KEK Proceedings 99-15
October 1999
H/R

Proceedings of the Eighth EGS4 Users' Meeting in Japan

August 1 - 3, 1999.

KEK, Tsukuba, Japan

Edited by

H. Hirayama, Y. Namito and S. Ban
KEK, High Energy Accelerator Research Organization

High Energy Accelerator Research Organization (KEK), 1999

KEK Reports are available from:

Information Resources Division
High Energy Accelerator Research Organization (KEK)
1-1 Oho, Tsukuba-shi
Ibaraki-ken, 305-0801
JAPAN

Phone: (81)-0298-64-5137
Fax: (81)-0298-64-4604
E-mail: adm-jouhoushiryou1@ccgemail.kek.jp
Internet: http://www.kek.jp

FOREWARD

The Eighth EGS4 Users' Meeting in Japan was held at High Energy Accelerator Research Organization (KEK) from August 1 to 3. The meeting has been hosted by the Radiation Science Center. Nearly 90 participants attended the meeting.

The meeting was divided into two parts. Lectures concerning the EGS4 System, Mortran, User code, HOWFAR, how to use PEGS4, how to write source routine and the EGS4 shower display system on PC were given at the first half. Practices to install the EGS4 system on the UNIX workstation or PC and to run PEGS4 or user code were also performed. In the later half, 15 talks related EGS4 were presented. The talks covered the wide fields, like the medical application and the calculation of various detector response *etc.* These talks were very useful to exchange the information between the researchers in the different fields.

Finally, we would like to express our great appreciation to all authors who have prepared manuscript quickly for the publication of this proceedings.

Hideo Hirayama
Yoshihito Namito
Syuichi Ban
Radiation Science Center
KEK, High Energy Accelerator Research Organization

CONTENTS

IMPROVEMENT OF THE CROSS-SECTION AND BRANCHING-RATIO EVALUATION IN EGS4 IN THE ENERGY INTERVAL WHICH HAS AN ABSORPTION-EDGE

Y. NAMITO and H. HIRAYAMA

High Energy Accelerator Research Organization (KEK)
Oho, Tsukuba-shi, Ibaraki-ken, 305-0801, Japan

Abstract

EGS4 treats the cross section and branching ratio in fitting to a linear function in small energy intervals. This technique is called a "piece-wise line-fit" (=PWLF). PWLF breaks down in the vicinity of the photon absorption edge and produces a large error. The intensities of K_β and several L-x rays are underestimated due to this PWLF error. To avoid this breakdown, we improved the PWLF. In the energy interval which has an absorption edge, the interpolation is sustained and extrapolation from either a higher or lower energy bin is employed to evaluate the photon cross section and the branching ratio. This method is called the "local extrapolation method" (LEM). By using LEM, a reasonable evaluation of the intensity of the characteristic x-ray is achieved.

1 What is PWLF?

Prior to an EGS4 calculation [1], material data are produced using the PEGS4 program. PEGS4 estimates the mean-free path (MFP) and branching ratio of interactions using the theory and experiment values, and fit them to linear functions of energy in each energy interval. PEGS4 outputs the coefficients of these linear functions, and EGS4 reads in them in HATCH and uses them for a Monte-Carlo calculation. For photons, the energy intervals are set to have an equal width on the logarithm scale. Here, the number of intervals is increased until the error of the theory or experiment and the linear function become within some set allowance. This is an outline of the Piece-Wise Linear Fit (=PWLF) used in the EGS4 code. For most of the cases, the error becomes smaller than the allowance before the number of intervals becomes the upper limit (200). In this case, the error of PWLF is less than the allowance set in the PEGS4.

2 Enhancement of the PWLF-error Near to the Absorption Edge

Only one apparent exception to this is the photon mfp and the branching ratio in the energy interval with the absorption edge. In the energy interval which has the absorption edge, the photon mean-free path (GMFP) changes by a factor of about 4 like a step-function. On the other hand, GMFP in PWLF changes like a linear function. Thus, GMFP in PWLF has a large error.

An example of GMFP near to the K-absorption-edge in the material data of copper is shown in Fig. 1. Here, PWLF has a great error in the energy interval having an absorption edge (hereafter called "edge-interval"; here, it is the 64th interval). The edge-energy is 8.9789 keV. The enhancement of the PWLF-error occurs only in the edge-bin, and does not affect to the other intervals. The material data was made with UP=1.0 MeV, AP=0.001 MeV, MXGE=200. MXGE is the upper-limit of the energy interval number. The width of the energy interval (Δ) is calculated by $(\mathrm{UP/AP})^{1/N}$, and now Δ is 3.6%. Here, N is the number of intervals, 198 (=MXGE-2).

3 The Effect to Characteristic X-Rays

This enhancement of the error is not obvious for itself. The enhancement of the error becomes obvious, because the energy of some of the characteristic x-rays is within this edge interval, and their transport is affected by this PWLF error in the edge-bin. For example, the energy difference of the K_α, $K_{\beta,1}$ or $K_{\beta,2}$ and K-edge is about 10%, about 1% and 0.02% for copper; transport of K_β is affected by the PWLF-error in most cases. The error of GMFP for K_{β_1} and K_{β_2} is 60% and 79%, respectively, as shown in Table 1.

As the number of K-X rays emitted outside the target is roughly proportional to GMFP, the error of the number of emitted photons is almost equal to the GMFP-error. A comparison of the measured and EGS4-calculated number of K-X-rays emitted outside the target is shown in Fig 2. Here, 40 keV photons incident on a copper target. The experimental setup is described in Ref.[2]. While the agreement is good for K_α rays, the EGS4 calculation underestimated the K_β rays by about 50% of the measurement due to the effect of a PWLF-error near to the edge.

4 Local Extrapolation Method

To solve this problem, we developed the following calculation method: (The concept of this method is shown in Fig 3.)

1. Judgment of an "IN" edge-interval or not
   Prior to a Monte Carlo calculation, the interval number of the edge bin is calculated and saved. When the energy interval number of a photon agrees with the edge bin number, the photon is judge to be entering the edge-bin.

2. Comparison of the photon energy and edge energy

   - Save all edge energies (K, L_1, L_2, L_3) of all elements in each region.
   - Compare the photon energy and the edge energy of the corresponding edge interval.

3. Extrapolation of GMFP

   - Extrapolate from a higher energy bin in the case that the photon energy is higher than the edge energy.
   - Extrapolate from a lower energy bin in the case that the photon energy is lower than the edge energy.

4. Treat the branching ratio between the photoelectric effect, Compton scattering, pair production, Rayleigh scattering in the same manner.

The macros for this method is shown in Fig. 4. To change into extrapolation from interpolation, one has to increase or decrease the energy-interval number by one. Because this is the only necessary operation, the modifications of a calculation are few. The increase in the calculation time is below

the detection limit. Because this method utilizes only extrapolation in the energy interval which has an absorption edge, this calculation method can be called the "Local Extrapolation Method" (LEM).

The GMFP of PWLF with LEM almost agrees with the exact values shown in Fig. 5. Also, the GMFP error of K_{β_1} and K_{β_2} decreased by a factor of 100, to 0.5% and 0.8%, respectively, as shown in Table 1.

5 The Limit of LEM

The LEM does not work in the case that more than 2 edges are contained in one energy interval or in the case that neighboring energy intervals energy intervals contain edges. The cure for them is to make the width of the energy intervals (Δ) narrower, so that these things do not occur. The guidelines for Δ to make LEM work are:

- No restriction for Δ is necessary in the case that the K edge is concerned in the region of a single element. Δ can be very wide.
- "$2\Delta < E_{L_2}/E_{L_3} - 1$" in the case that both the K- and L-edge are concerned in the region of a single element. Here, E_{L_2} and E_{L_3} are the L_2- and L_3-absorption edge energy, respectively. For example, $\Delta < 1.1\%$, 2.6%, 8% for Zn、Ag、Pb, respectively.
- Δ <0.25% is hopeful in the case that both the K- and L-edge are concerned in the region of plural elements. The probability of normal operation of LEM is 99.9%.

6 Other Methods

It is possible to avoid the effect of an enhancement of the PWLF error near to the absorption edge by making Δ so small that the characteristic x ray energy does not belong to the edge bin. For example, the effect of a PWLF error enhancement on the $K_{\beta,1}$ ray of copper can be avoided by making MXGE= 800. Because the intensity of the remaining $K_{\beta,2}$ ray of copper is quite weak, the agreement of the measurement and calculation becomes very good by this. However, MXGE=40000 is necessary in the case that one wants to calculate the intensity of the $K_{\beta,2}$ ray without any enhancement of the PWLF-error. Also, the energy of some L-X ray is quite close to the absorption-edge energy. For example, the energy difference of the Pb $L_{\gamma,6}$ or $L_{\beta,5}$ and absorption edge energy is only 0.2%. To handle them adequately, MXGE=4000 is necessary. It is desirable to avoid making photon data a few 10 or a few 100-times bigger to treat the absorption edge adequately from the view point of calculation efficiency.

References

1) W. R. Nelson, H. Hirayama and D.W.O. Rogers, SLAC-265 (Stanford University, Stanford, 1985).

2) Y. Namito, S. Ban. H. Hirayama, N. Nariyama, H. Nakashima, Y. Nakane, Y. Sakamoto, N. Sasamoto, Y. Asano, and S. Tanaka, "Compton Scattering of 20-40 keV Photons", Phys. Rev. A **51**, 3036-3043 (1995).

Table 1: GMFP of Cu for K_{β_1}(8.905 keV) and K_{β_2}(8.977 keV).

	GMFP (μm)			
	K_{β_1}	(Error)	K_{β_2}	(Error)
Exact*	29.84		30.53	
PWLF	11.80	(-60%)	6.295	(-79%)
PWLF-LEM	29.69	(-0.5%)	30.30	(-0.8%)

* Obtained using CALL option of PEGS4.

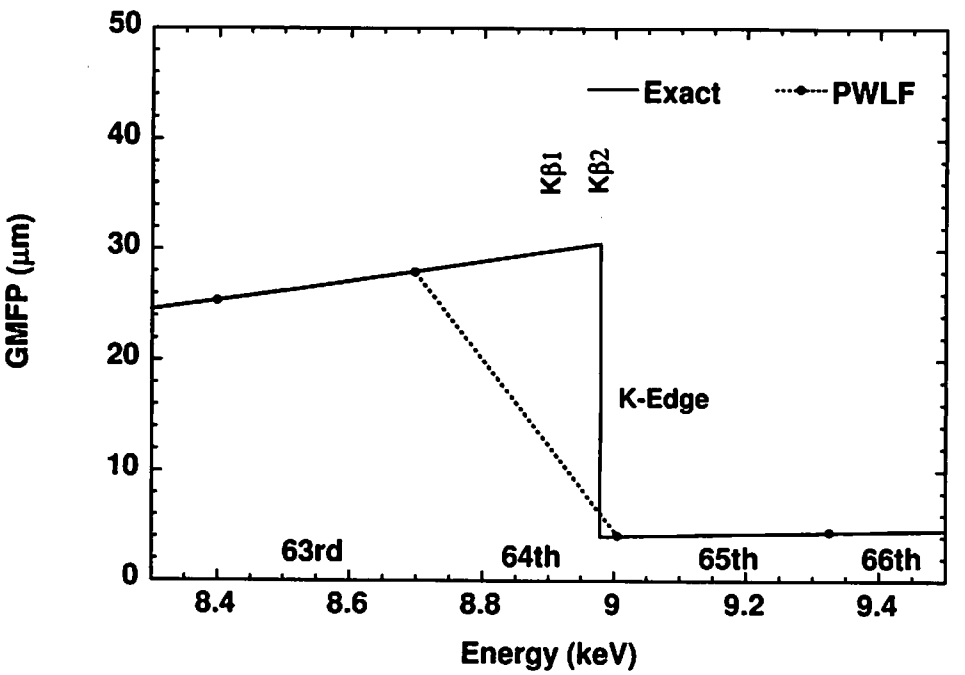

Figure 1: Evaluated values of the mean-free path of copper by PWLF. The error of PWLF is evident in the 64th interval where the K edge is contained.

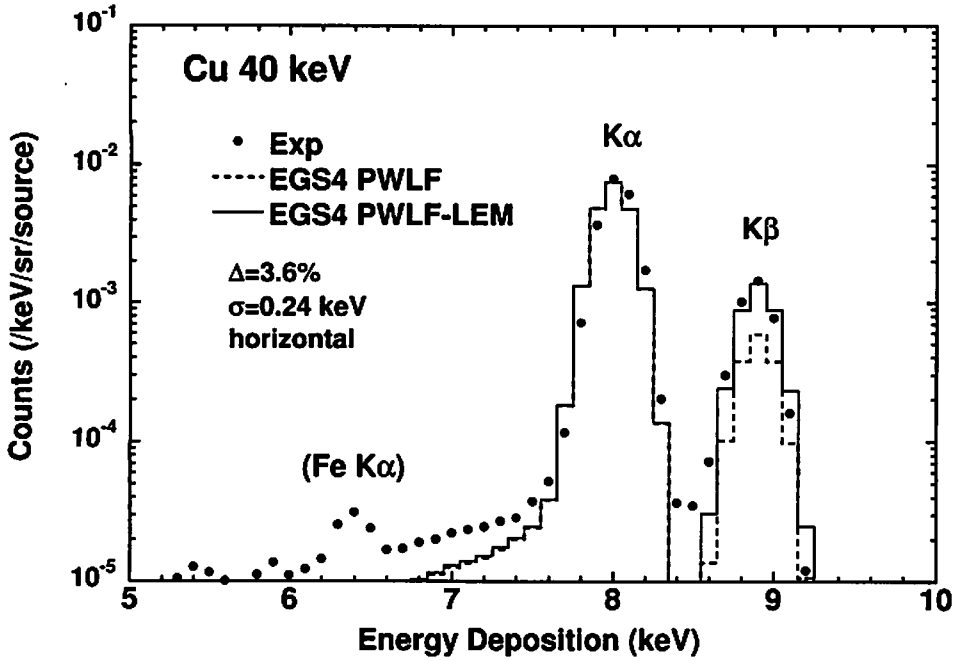

Figure 2: Comparison of measured and calculated intensity of the K-X ray. The intensity of the K_β ray is underestimated by a factor of 2 due to the error of PWLF in the EGS4 calculation using PWLF. This underestimate is recovered in the EGS4 calculation using PWLF-LEM. An underestimate of K_β can also be avoided by making Δ (width of the energy interval in the material data) narrower as the enhancement of the PWLF error affects only the photon transport in the edge bin.

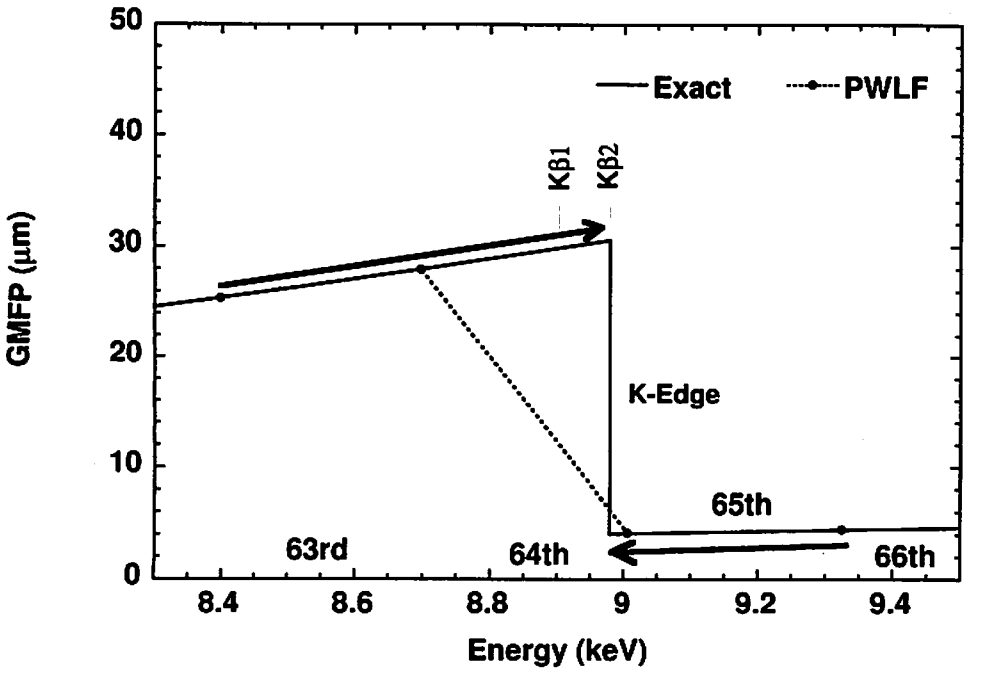

Figure 3: Concept of the local extrapolation method.

```
REPLACE {$EVALUATE GMFPRO USING GMFP(GLE);} WITH
{;IEXTP=0;
 IF(EIG.LT.0.15) [DO IIJ=1,NEDGB(MEDIUM) [
   IF(LEDGB(IIJ,MEDIUM).EQ.LGLE) [ "Judge if photon energy is in edge-bin"
     IF(EDGB(IIJ,MEDIUM).LE.EIG) [IEXTP=1;] "Extrapolate from higher-bin"
     ELSE [IEXTP=-1;]]]]                    "Extrapolate from lower-bin "
GMFPRO=GMFP1(LGLE+IEXTP,MEDIUM)*GLE+GMFP0(LGLE+IEXTP,MEDIUM);}

REPLACE {$EVALUATE GMFPRO USING GMFP(GLE);} WITH
{GMFPRO=GMFP1(LGLE,MEDIUM)*GLE+GMFP0(LGLE,MEDIUM);}

REPLACE {$EVALUATE COHFAC USING COHE(GLE);} WITH
{;COHFAC=COHE1(LGLE+IEXTP,MEDIUM)*GLE+COHE0(LGLE+IEXTP,MEDIUM);}

REPLACE {$EVALUATE GBR1 USING GBR1(GLE);} WITH
{;GBR1=GBR11(LGLE+IEXTP,MEDIUM)*GLE+GBR10(LGLE+IEXTP,MEDIUM);}

REPLACE {$EVALUATE GBR2 USING GBR2(GLE);} WITH
{;GBR2=GBR21(LGLE+IEXTP,MEDIUM)*GLE+GBR20(LGLE+IEXTP,MEDIUM);}
```

Figure 4: Macro for the local extrapolation method

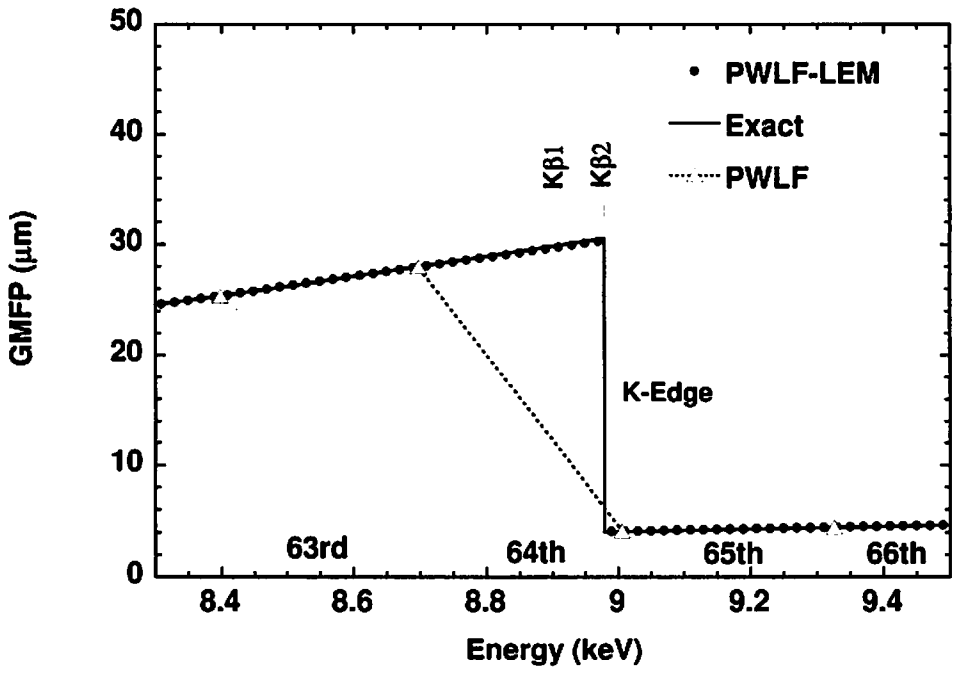

Figure 5: GMFP values evaluated by PWLF and LEM

THE INFORMATION EDICATION USING EGS4 MONTE CARLO CODE OF TOKYO METROPOLITAN UNIVERSITY OF HEALTH SCIENCES

M. FUKUSHI, Y. NAMITO[1] , H. SAITOH, K. FUKUDA

Department of Radiorogic Science Tokyo Metropolitan University of Health Sciences
2-10 Higashi-Ogu, 7Chome, Arakawa-ku, Tokyo 116-8551 Japan
[1]*High Energy Accelerator Research Organization*
1-1 Oho, Tsukuba-shi, Ibaraki 305-0801 Japan

Abstract

Tokyo Metropolitan University of Health Sciences has done The Information Education using EGS4 Monte Carlo code since the 1998 fiscal year.

Two items under practical training item were done.

1. The interaction between photon of 0.1 ~ 10 MeV (Mega Electron Volt :MeV) and Aluminum(Al),Iron(Fe) and Lead(Pb).
2. The simulation of gamma ray energy measurement of the radiation detector.

As the result, the student was possible the understanding of the radiation physics for the easiness at Practical training of EGS4 Monte Carlo code[1].

1 Introduction

With the explosive popularization of the personal computer, it ended in the age of the programming education. The computer literacy education becomes a part of the information processing education at present. In addition, necessity and importance of computer literacy education in the multimedia era heighten of popularization of the recent Internet and development of the multi-media technology. Therefore, the information processing education environment was rapidly equipped with Tokyo Metropolitan University of Health Sciences.

Then, practical training of EGS4 Monte Carlo code was started in the student of Department of Radiorogic Science Tokyo Metropolitan University of Health Sciences[2]. The practical training used personal computer (Windows-NT) of information processing practical training room for each one person one. And, the video projector carried out the description.

2 The Outline of the Information Education using EGS4 Monte Carlo Code

2.1 The installation of the program

The download of A (egs4pc.exe), B (user_code.exe), C (pictwin2.exe), D (metro.exe) and E (metro2.exe) is done from the teacher home page. The file is expanded in each.

2.2 The Description of Each Interaction

The following were made to be an object: Particle and interaction Photoelectric effect, Rayleigh Scattering, Compton Scattering, Pair production, Bremsstrahlung Emission, Annihilation, Moller Scattering, Bhabha Scattering and Multiple Coulomb scattering from the nucleus of The material. And, they were explained using the figure. Then, the student wrote the figure in the note, and it was made to be a material of Practical training of EGS4 Monte Carlo code.

2.3 The Item on Practical Training of EGS4 Monte Carlo Code

Following thing be programmed to run EGS4 Monte Carlo code: the type of the radiation source, The input energy, the geometrical condition and Type and position of the detector. However, these programming were omitted practical training, since the time is not sufficient. The student interactively inputs the type of the radiation source, the input energy and the number in the history. Next, the locus of the particle was output in the graphic. This practical training was carried out at groups about 8 persons.

The practical training of EGS4 Monte Carlo code did following two items.

1. The interaction of the photon energy from 0.1 to 10 MeV and Aluminum (Al), Iron (Fe) and Lead (Pb).

2. The simulation of the gamma ray energy of radiation detector.

2.3.1 The interaction of the photon energy from 0.1 to 10 MeV and Aluminum (Al), Iron (Fe) and Lead (Pb)

1. Proportion (P) of the photons that penetrates directly the photon was monotonously emitted. And, proportion (S) of the photon which scatters by interacting with the flat plate, is required.

   The material of the planar target used Lead (Pb) Aluminum (Al) Iron (Fe). The incident photons energy 0.1,1.0 and 10.0 MeV and thickness of the flat plate were made to be 1,2,5 and 10 cm. And, The number in the history was made to be 50. Next, Shower.exe of EGS4PICT is executed. The student Leads each interaction and (P), (S) from the locus of the photon.

2. In making P to be a function of the thickness at Kaleida Graph for Windows, it is plotted in the semilogarithm. The thickness of P=1/e [e=2.72] is obtained from the gradient of this regression line. This thickness is "Mean Free Path of the photon". The material and the energy dependence of Mean Free Path are examined.

3. The material is made to be Lead (Pb), and Mean Free Path for 70, 80, 90 and 100 keV of photon energy is required. And, the energy dependence is examined.

4. "Build-up factor = (P + S)/P" is obtained. Then, Thickness and energy, The material dependence of the Build-up factor are examined.

5. How does main interaction change at energy and the material ? Then, how each interaction is utilized in radiodiagnosis and radiotherapy treatment. Or, whether it becomes the noise is examined.

2.3.2 The simulation of the gamma ray energy of radiation detector

1. The photon of 1 MeV is emitted in a NaI of the flat plate. Students sketch all the trajectories of γ, e^- & e^+, which are displayed on computer screens. The type of the reaction is confirmed from the locus. And, whether it absorbed the photon in the detector all is confirmed. And, the absorbed energy is recorded.

   These operations are repeated to 20 times. Next three points are examined after the end.

   (a) The absorbed energy in absorbing the photon in the detector all.

   (b) The absorbed energy in absorbing the part of the photon in the detector.

   (c) The absorbed energy as the photon does the element way of the detector.

2. Under the condition of (1), by increasing the photon number in 5000, the distribution of the absorbed energy is calculated. Kaleida Graph for Windows is used for the display. And, all efficiency and peak efficiency are recorded. Then, next seven points are examined.

   (a) Is total energy absorption peak correspondent to which reaction of the locus ?

   (b) What kind of process it deals with there is other peak.

   (c) Is the connected part correspondent to which reaction of the locus ? And, why this part becomes the continuous distribution without becoming a peak.

   (d) The energy of the photon is made to be 0.3 and 3.0 MeV. Then, 1 MeV it is compared.

   (e) What does difference (ΔE) of energy of right end of the connected energy division minute and peak energy originate ?

   (f) How do all efficiency and peak efficiency change by the incident energy?

3 Result

The student noticed following fact by Practical training of EGS4 Monte Carlo code.

1. Two gamma ray are discharged in the front, when Positron annihilation it under flight. It was proven that it became a factor of the error in Positron Emission Tomography.

2. Since electronic Moller scattering occurs in the multiple dose, the most abounding reaction became a Moller scattering.

3. The limited figure length was realized by repeatedly plowing the extension.

And, it has been proven that the utilization of the graphic is effective in computer practical training that made the student to be an object. Then, this practical training also used the graphic abundantly. Therefore, it was possible that the student maintained the interest at the whole for practical training hour and that it positively tackles practical training (figure 1). The student does Practical training of EGS4 Monte Carlo code, and it is considered that the understanding of the radiation physics was possible for the easiness.

4 Conclusion

The outline of content and method of "The Information Education using EGS4 Monte Carlo code of Tokyo Metropolitan University of Health Sciences" for the student of Department of Radiorogic Science Tokyo Metropolitan University of Health Sciences was described. As the result, following problems were sensed.

Four items under the time using EGS4 Monte Carlo code are spent and are done[3,4]. Four items are Type of the radiation source, Energy, Geometrical condition and Position of the detector. Then, it would be able to carry out the simulation of high degree of freedom becomes possible. And, EGS4 Monte Carlo code is utilized for the graduation research. In addition, practical training of the computer is made to be a more effective thing. Therefore, we consider that to cooperate the observation with the lecture is important. However, we realized the purpose in the beginning by Practical training of EGS4 Monte Carlo code.

References

1) W. R. Nelson, H. Hirayama and D. W. O. Roger, "The EGS4 code system", *SLAC report-265* 1985.

2) Y. Namito, M. Fukushi, H. Hirayama, H. Saitoh and T. Fujisaki, "Nuclear medicine class using EGS4 Monte Carlo code", *J. Med. Phys.* **18** Supplement57: 211-214, 1998.

3) H. Hirayama and Y. Namito, "Lecture Note of EGS4 Course at KEK", *Internal 99-5*, 1999.

4) H. Hirayama and Y. Namito, "Lecture Note Installation of EGS4 (Revised in 1999) *KEK Internal* 99-4: 1999.

Fig. 1.

INTERPRETATION OF DEPTH-VARIATION OF MOLIÈRE ANGULAR DISTRIBUTION WITH IONIZATION

T. NAKATSUKA

Okayama Shoka University
Tsushima-Kyomachi, Okayama 700-8601, Japan

Abstract

Under the Molière multiple scattering process with ionization, the shape of angular distribution becomes young again or the expansion parameter B becomes small again just before charged particles dissipate their whole energies. We have investigated the mechanism of depth-variation of the distribution using Kamata-Nishimura formulation of the Molière theory and found that the variation of the shape can be interpreted by the shifts of frequency component between the central gaussian term and the asymptotic single scattering term or by the variation of discriminating angle between the moderate small angle scattering and the low-frequency large angle scattering. The translation formula between the Kamata-Nishimura formulation and the Molière-Bethe one giving full compatible results in the nonrelativistic condition is also proposed.

1 Introduction

We have proposed an improved Molière angular distribution to take account of ionization loss in the last meeting [1]. We expected almost all scattering properties would proceed more rapidly in the ionization process than in the fixed-energy process. But the new theory predicts the shape of angular distribution grows old slower in the ionization process and moreover it becomes young again before charged particles dissipate their whole energies. More precisely, the expansion parameter B increases more slowly and becomes small again before they reach to their ranges. The fact was not so easy to accept for us that we investigated the mechanism of depth-variation of Molière angular distribution using Kamata-Nishimura formulation [2, 3] of the Molière theory [4, 5, 6] under the massless approximation [1].

Kamata-Nishimura formulation is equivalent with Molière-Bethe one except for the expansion errors [7]. There exists a translation formula between them. We should remind the former formulation was described in the relativistic condition. In case we apply the former formulation in the nonrelativistic condition a small cares should be added to the original theory. We compared the both formulations in detail and got the Kamata-Nishimura formulation of Molière theory with ionization full compatible with Molière-Bethe results at the fixed-energy limit, revising the last result [1].

2 Molière Angular Distribution with Ionization under the Massless Approximation

We can get Molière angular distribution with ionization in the following process [1]. The diffusion equation is

$$\frac{\partial f}{\partial t} = \iint f(\vec{\theta} - \vec{\theta}') - f(\vec{\theta})\}\sigma(\vec{\theta}')d\vec{\theta}' + \varepsilon\frac{\partial f}{\partial E}, \tag{1}$$

where $\sigma(\vec{\theta})$ denotes the single scattering formula. We assume axial symmetrical condition in this text, then the formula can be expressed as

$$\sigma(\vec{\theta})d\vec{\theta}dt = \sigma(\theta)2\pi\theta d\theta dt = \frac{1}{\pi\Omega}\frac{K^2}{p^2v^2}\theta^{-4}2\pi\theta d\theta dt, \tag{2}$$

where the scattering angle is taken greater than the Molière screening angle:

$$\theta > \sqrt{e}\chi_a. \tag{3}$$

Applying Hankel transforms, we get

$$\frac{\partial \tilde{f}}{\partial t} = -2\pi\tilde{f}\int_0^\infty \theta d\theta[1 - J_0(\zeta\theta)]\sigma(\theta) + \varepsilon\frac{\partial \tilde{f}}{\partial E}. \tag{4}$$

According to the Kamata-Nishimura formulation in the relativistic condition, the diffusion equation becomes

$$\frac{\partial \tilde{f}}{\partial t} = -\frac{K^2\zeta^2}{4E^2}\tilde{f}\{1 - \frac{1}{\Omega}\ln\frac{K^2\zeta^2}{4E^2}\} + \varepsilon\frac{\partial \tilde{f}}{\partial E}, \tag{5}$$

so that we get the solution as

$$\tilde{f} = \frac{1}{2\pi}\exp\{-\frac{K^2\zeta^2 t}{4E_0E}[1 + \frac{1}{\Omega}(2 - \frac{E_0 + E}{E_0 - E}\ln\frac{E_0}{E}) - \frac{1}{\Omega}\ln\frac{K^2\zeta^2}{4E_0E}]\}. \tag{6}$$

By applying the translation formula proposed last we can reform the solution to the standard Molière form, so that we get the angular distribution in Molière series;

$$f(\vartheta) = f^{(0)}(\vartheta) + \frac{1}{B}f^{(1)}(\vartheta) + \frac{1}{B^2}f^{(2)}(\vartheta) + \cdots, \tag{7}$$

where

$$\vartheta \equiv \theta/\theta_{\mathrm{M}}. \tag{8}$$

The Molière distribution is characterized by two parameters, the expansion parameter B and the unit of Molière variable θ_{M}. In this case these are determined as

$$B - \ln B = \Omega - \ln\Omega + \ln(\nu t) \tag{9}$$

and

$$\theta_{\mathrm{M}} = \theta_{\mathrm{G}}\sqrt{B/\Omega}, \tag{10}$$

where

$$\nu = e^2(E/E_0)^{(E_0+E)/(E_0-E)} \tag{11}$$

and

$$\theta_{\rm G} = \frac{K\sqrt{t}}{\sqrt{E_0 E}}. \tag{12}$$

ν is a function of fractional thickness, $t/(E_0/\varepsilon)$, decreasing with thickness as indicated in Fig. 1. In case of fixed-energy process ν shoud be taken as 1, which is the limiting value of Eq. (11) at $E \to E_0$. $\theta_{\rm G}$ denotes the root mean square angle evaluated by the gaussian approximation [8, 9] with the scattering energy E_s replaced by the Kamata-Nishimura constant K [2, 3].

We indicate the depth-variations of the expansion parameter B for various incident energies in Fig. 2. In case of fixed-energy process ν is 1 so that B increases monotonusly with t as indicated by the dot line in the figure. In case of ionization process the parameters B increase with t but just before charged particles reach to their ranges they begin to decrease, as understood from Eq. (9) and shown in the figure.

Also we indicate the depth-variations of the unit of Molière variable $\theta_{\rm M}$ for various incident energies in Fig. 3. The units $\theta_{\rm M}$ can be regarded almost indicating the root mean square spreads of central gaussian feature of the Molière distribution. In case of fixed-energy process the units $\theta_{\rm M}$ increase monotonusly a little more rapid than $\sqrt{t}$ under the gaussian approximation. In case of ionization process the units $\theta_{\rm M}$ increase still more rapid and they diverge just before charged particles reach to their ranges.

The angular distributions with ionization are compared with those under the fixed-energy condition in Fig. 4. At thicknesses of small dissipated energy the both distributions agree well but with dissipation of energy the formers show more rapid broadening. The distributions show gaussian features in the central small angle region and asymptotic single scattering features at large angle region. In fixed-energy condition the weights of the asymptotic single scattering feature decrease monotonusly with traversed thickness but in ionization process the weights return to become a little large again before chraged particles dissipate their whole energies.

3 Depth-Variation of Molière Angular Distribution: Interpretation in the Frequency Space

In the fixed-energy process, the weight of asymptotic single scattering term decreases monotonusly with increase of traversed thickness comparing with central gaussian term. But in the ionization process, it decreases more slowly and rather it begins to increase again at final stage of traverse. We want to investigate the mechanism of depth-variation of Molière angular distribution first in the frequency space.

If we regard the dependence of energy on traversed thickness as

$$E = E_0 - \varepsilon t, \tag{13}$$

the last term of Eq. (5) vanishes and we get

$$\frac{\partial \tilde{f}}{\partial t} = -\frac{K^2\zeta^2}{4E^2}\tilde{f}\{1 - \frac{1}{\Omega}\ln\frac{K^2\zeta^2}{4E^2}\}. \tag{14}$$

We can integrate the equation as

$$\tilde{f} = \frac{1}{2\pi}\exp\{-\langle\frac{K^2\zeta^2}{4E^2}\rangle_{\rm av} t + \frac{1}{\Omega}\langle\frac{K^2\zeta^2}{4E^2}\ln\frac{K^2\zeta^2}{4E^2}\rangle_{\rm av} t\}, \tag{15}$$

where we have introduced the averages taking along the traversed thickness;

$$\langle x\rangle_{\rm av} \equiv t^{-1}\int_0^t x dt. \tag{16}$$

In case of fixed-energy process, terms in the average bracket are constants. So we get

$$\tilde{f} = \frac{1}{2\pi}\exp\{-\frac{K^2\zeta^2 t}{4E^2}(1-\frac{1}{\Omega}\ln\frac{K^2\zeta^2}{4E^2})\}. \tag{17}$$

If we modify the right-hand side so as the terms to have the same composite variable inside and outside of the logarythm, we can express the first higher term by a universal function:

$$\begin{aligned} 2\pi\tilde{f} &= \exp\{-\frac{K^2\zeta^2 t}{4E^2}(1+\frac{1}{\Omega}\ln t-\frac{1}{\Omega}\ln\frac{K^2\zeta^2 t}{4E^2})\} \\ &\simeq \exp\{-(1+\frac{1}{\Omega}\ln t)\frac{\theta_{\rm G}^2\zeta^2}{4}\}-\frac{1}{\Omega}\exp\{-\frac{\theta_{\rm G}^2\zeta^2}{4}\}\frac{\theta_{\rm G}^2\zeta^2}{4}\ln\frac{\theta_{\rm G}^2\zeta^2}{4}+\cdots, \end{aligned} \tag{18}$$

where $\theta_{\rm G}$ denotes the root mean square angle evaluated in the gaussian approximation. So that we get

$$f2\pi\theta d\theta \simeq f^{(0)}(\frac{\theta/\theta_{\rm G}}{\sqrt{1+\Omega^{-1}\ln t}})\frac{\theta d\theta/\theta_{\rm G}^2}{(1+\Omega^{-1}\ln t)}+\frac{1}{\Omega}f^{(1)}(\frac{\theta}{\theta_{\rm G}})\frac{\theta d\theta}{\theta_{\rm G}^2}+\cdots. \tag{19}$$

We see the shift of $\Omega^{-1}\ln t$ term in the frequency space accelerates the broadening of central gaussian distribution more than $\sqrt{t}$ under the gaussian approximation, making the width wider at $t>1$ and narrower at $t<1$.

In case with ionization, terms in the average brackets vary with thickness of traverse and we get

$$\langle\frac{K^2\zeta^2}{4E^2}\rangle_{\rm av} = \frac{K^2\zeta^2}{4E_0E}, \tag{20}$$

$$\langle\frac{K^2\zeta^2}{4E^2}\ln\frac{K^2\zeta^2}{4E^2}\rangle_{\rm av} = \frac{K^2\zeta^2}{4E_0E}\ln\frac{K^2\zeta^2}{4E_0E\nu}. \tag{21}$$

We see the term ν defined in Eq. (11) appears in the average. So that we get

$$\begin{aligned} \tilde{f} &= \frac{1}{2\pi}\exp\{-\frac{K^2\zeta^2 t}{4E_0E}(1-\frac{1}{\Omega}\ln\frac{K^2\zeta^2}{4E_0E\nu})\} \\ &= \frac{1}{2\pi}\exp\{-\frac{K^2\zeta^2 t}{4E_0E}(1+\frac{1}{\Omega}\ln\nu t-\frac{1}{\Omega}\ln\frac{K^2\zeta^2 t}{4E_0E})\}. \end{aligned} \tag{22}$$

This time the term of $\Omega^{-1}\ln\nu t$ shifts so as the first higher term to be the universal function, so that

$$2\pi\tilde{f} \simeq \exp\{-(1+\frac{1}{\Omega}\ln\nu t)\frac{\theta_{\rm G}^2\zeta^2}{4}\}-\frac{1}{\Omega}\exp\{-\frac{\theta_{\rm G}^2\zeta^2}{4}\}\frac{\theta_{\rm G}^2\zeta^2}{4}\ln\frac{\theta_{\rm G}^2\zeta^2}{4}+\cdots \tag{23}$$

and

$$f2\pi\theta d\theta \simeq f^{(0)}(\frac{\theta/\theta_{\rm G}}{\sqrt{1+\Omega^{-1}\ln\nu t}})\frac{\theta d\theta/\theta_{\rm G}^2}{(1+\Omega^{-1}\ln\nu t)}+\frac{1}{\Omega}f^{(1)}(\frac{\theta}{\theta_{\rm G}})\frac{\theta d\theta}{\theta_{\rm G}^2}+\cdots. \tag{24}$$

It should be noticed that there exists a decreasing factor ν in the unit of central gaussian distribution this time, which makes the increase of the unit slow down compared with the unit of asymptotic single scattering term.

4 Depth-Variation of Molière Angular Distribution: Interpretation in the Angular Space

We want to make the same investigation of the mechanism of depth-variation of Molière angular distribution as in the pevious section, in the angular space.

We separate the single scattering formula to two parts, moderate small angle scattering $\sigma_{\rm M}$ and low-frequency large angle scattering $\sigma_{\rm L}$:

$$\sigma(\theta) = \sigma_{\rm M}(\theta) + \sigma_{\rm L}(\theta), \tag{25}$$

where the two scatterings are separated by the discriminating angle

$$\theta_{\rm D} = e^{\Omega/2}\sqrt{e}\chi_{\rm a} = (K/E)e^{1-C}. \tag{26}$$

Using the Bethe formula Eq. (14) of [6]

$$I_1(x) \equiv 4\int_x^\infty t^{-3}[1 - J_0(t)]dt \simeq 1 + \ln 2 - C - \ln x + O(x^2) \tag{27}$$

and evaluating the similar integration in the finite angular range as

$$\int_{\theta_{\rm min}}^{\theta_{\rm max}}[1 - J_0(\theta\zeta)]\sigma(\theta)2\pi\theta d\theta \simeq \frac{1}{\Omega}\frac{K^2\zeta^2}{4E^2}\ln(\theta_{\rm max}/\theta_{\rm min})^2, \tag{28}$$

we can evaluate the diffusion factor appearing in Eq. (4) for the both scatterings, respectively:

$$\int_0^\infty [1 - J_0(\theta\zeta)]\sigma_{\rm M}(\theta)2\pi\theta d\theta \simeq \frac{K^2\zeta^2}{4E^2}, \tag{29}$$

$$\int_0^\infty [1 - J_0(\theta\zeta)]\sigma_{\rm L}(\theta)2\pi\theta d\theta \simeq -\frac{1}{\Omega}\frac{K^2\zeta^2}{4E^2}\ln\frac{K^2\zeta^2}{4E^2}. \tag{30}$$

We can express the solution of Eq. (14) in the Kamata-Nishimura series [7]

$$\tilde{f} = \tilde{f}_0 + \Omega^{-1}\tilde{f}_1 + \Omega^{-2}\tilde{f}_2 + \cdots, \tag{31}$$

by using the terms derived from the recurrence formula

$$\frac{\partial\tilde{f}_k}{\partial t} + \frac{K^2\zeta^2}{4E^2}\tilde{f}_k = \frac{K^2\zeta^2}{4E^2}\tilde{f}_{k-1}\ln\frac{K^2\zeta^2}{4E^2}. \tag{32}$$

The first two terms among them are derived as

$$\tilde{f}_0 = \frac{1}{2\pi}\exp\{-\int_0^t \frac{K^2\zeta^2}{4E^2}dt\} = \frac{1}{2\pi}\exp\{-\langle\frac{K^2\zeta^2}{4E^2}\rangle_{\rm av}t\}, \tag{33}$$

$$\begin{aligned}\tilde{f}_1 &= \frac{1}{2\pi}\exp\{-\int_0^t \frac{K^2\zeta^2}{4E^2}dt\}\int_0^t \frac{K^2\zeta^2}{4E^2}\ln\frac{K^2\zeta^2}{4E^2}dt \\ &= \frac{1}{2\pi}\exp\{-\langle\frac{K^2\zeta^2}{4E^2}\rangle_{\rm av}t\}\langle\frac{K^2\zeta^2}{4E^2}\ln\frac{K^2\zeta^2}{4E^2}\rangle_{\rm av}t.\end{aligned} \tag{34}$$

In case of fixed-energy process, the first two terms are explicitly expressed as

$$\tilde{f}_0 = \frac{1}{2\pi}\exp\{-\frac{K^2\zeta^2 t}{4E^2}\} = \frac{1}{2\pi}\exp\{-\frac{\theta_{\rm G}^2\zeta^2}{4}\}, \tag{35}$$

$$\tilde{f}_1 = \frac{1}{2\pi}\exp\{-\frac{\theta_{\rm G}^2\zeta^2}{4}\}\frac{K^2\zeta^2 t}{4E^2}\ln\frac{K^2\zeta^2}{4E^2}. \tag{36}$$

We examine the configuration of the second term, or the first higher term, in detail. In the frequency space we get

$$\begin{aligned}\tilde{f}_1 &= -\frac{1}{2\pi}\exp\{-\frac{\theta_G^2\zeta^2}{4}\}\Omega t\int_{\theta_D}^{\infty}[1-J_0(\zeta\theta)]\sigma(\theta)2\pi\theta d\theta \\ &= -\frac{1}{2\pi}\exp\{-\frac{\theta_G^2\zeta^2}{4}\}2t\int_{(K/E)e^{1-C}}^{\infty}[1-J_0(\zeta\theta)]\frac{K^2}{E^2}\theta^{-3}d\theta \\ &= -\frac{1}{\pi}\exp\{-\frac{\theta_G^2\zeta^2}{4}\}\int_{e^{1-C}/\sqrt{t}}^{\infty}[1-J_0(\theta_G\zeta x)]x^{-3}dx, \qquad (37)\end{aligned}$$

so that in the angular space we get

$$\begin{aligned}\Omega^{-1}f_1 d\vec{\theta} &= -td\vec{\theta}\iint[f_0(\vec{\theta})-f_0(\vec{\theta}-\vec{\theta}')]\sigma_L d\vec{\theta}' \\ &= \frac{2}{\pi\Omega}d\vec{\phi}e^{-\phi^2}\int_{e^{1-C}/\sqrt{t}}^{\infty}\phi'^{-3}(\frac{1+\cosh 2\phi\phi'}{2}e^{-\phi'^2}-1)d\phi', \qquad (38)\end{aligned}$$

respectively. The both expressions have explicit t in the lower boundaries of integration. If we separate the integrtion to two parts by the boundary at $\sqrt{t}$ times greater angle of θ_D, then the asymptotic single scattering term can be expressed by a universal function of the composite variable

$$\phi = \theta/\theta_G. \qquad (39)$$

In fact we have

$$\begin{aligned}\tilde{f}_1 &= -\frac{1}{2\pi}\exp\{-\frac{\theta_G^2\zeta^2}{4}\}\Omega t\{\int_{\theta_D}^{\sqrt{t}\theta_D}+\int_{\sqrt{t}\theta_D}^{\infty}\} \\ &= -\frac{1}{2\pi}\exp\{-\frac{\theta_G^2\zeta^2}{4}\}\Omega t\{\frac{1}{\Omega}\frac{K^2\zeta^2}{4E^2}\ln t-\frac{1}{\Omega}\frac{K^2\zeta^2}{4E^2}\ln\frac{K^2\zeta^2 t}{4E^2}\} \\ &= \frac{1}{2\pi}\exp\{-\frac{\theta_G^2\zeta^2}{4}\}\{-\frac{\theta_G^2\zeta^2}{4}\ln t+\frac{\theta_G^2\zeta^2}{4}\ln\frac{\theta_G^2\zeta^2}{4}\} \qquad (40)\end{aligned}$$

and

$$\Omega^{-1}f_1 d\vec{\theta} = \frac{1}{\pi\Omega}(\phi^2-1)e^{-\phi^2}\ln t\, d\vec{\phi}+\frac{1}{\Omega}f^{(1)}(\phi)d\vec{\phi}. \qquad (41)$$

So that the first higher term of Kamata-Nishimura series is separated to the above two parts. The latter is the universal function to indicate the asymptotic single scattering term and the former indicates the acceleration term by which the width of central gaussian distribution varies a little more rapid than $\sqrt{t}$ under the gaussian approximation as mentioned in the section VII.B of Scott [10] and the section 4 of Kamata-Nishimura [2].

In case of ionization process, we get the following expressions for the first two terms of Kamata-Nishimura expansion:

$$\tilde{f}_0 = -\frac{1}{2\pi}\exp\{-\frac{\theta_G^2\zeta^2}{4}\}, \qquad (42)$$

$$\tilde{f}_1 = -\frac{1}{2\pi}\exp\{-\frac{\theta_G^2\zeta^2}{4}\}\Omega\int_0^t dt'\int_{\theta_D}^{\infty}[1-J_0(\zeta\theta)]\sigma(\theta)2\pi\theta d\theta. \qquad (43)$$

We should remind the screening angle $\sqrt{e}\chi_a$ and the discriminating angle θ_D, both, increase along traversed thickness this time due to decreasing E. We replace the increasing θ_D by a constant

discriminating angle $\overline{\theta_D}$ which corresponds to θ_D at the geometrical mean energy $\sqrt{E_0 E}$, then we get

$$\begin{aligned}
\tilde{f}_1 &= -\frac{1}{2\pi}\exp\{-\frac{\theta_G^2\zeta^2}{4}\}\Omega\int_0^t dt'\{\int_{\theta_D}^{\overline{\theta_D}}+\int_{\overline{\theta_D}}^{\infty}\} \\
&= -\frac{1}{2\pi}\exp\{-\frac{\theta_G^2\zeta^2}{4}\}\Omega\int_0^t dt'\ \frac{1}{\Omega}\frac{K^2\zeta^2}{4E'^2}\ln(\overline{\theta_D}/\theta_D)^2+\frac{2}{\Omega}\frac{K^2\zeta^2}{4E'^2}\int_{\zeta\overline{\theta_D}}^{\infty}x^{-3}[1-J_0(x)]dx\} \\
&= -\frac{1}{2\pi}\exp\{-\frac{\theta_G^2\zeta^2}{4}\}\Omega\int_0^t dt'\ \frac{1}{\Omega}\frac{K^2\zeta^2}{4E'^2}\ln\frac{E'^2}{E_0E}-\frac{1}{\Omega}\frac{K^2\zeta^2}{4E'^2}\ln\frac{K^2\zeta^2}{4E_0E}\}. \qquad (44)
\end{aligned}$$

So that the first higher term becomes

$$\begin{aligned}
\tilde{f}_1 &= \frac{1}{2\pi}\exp\{-\frac{\theta_G^2\zeta^2}{4}\}\Omega\{-\frac{t}{\Omega}\frac{K^2\zeta^2}{4E_0E}\ln\nu+\frac{t}{\Omega}\frac{K^2\zeta^2}{4E_0E}\ln\frac{K^2\zeta^2}{4E_0E}\} \\
&= \frac{1}{2\pi}\exp\{-\frac{\theta_G^2\zeta^2}{4}\}\{-\frac{\theta_G^2\zeta^2}{4}\ln\nu t+\frac{\theta_G^2\zeta^2}{4}\ln\frac{\theta_G^2\zeta^2}{4}\}. \qquad (45)
\end{aligned}$$

¿From the result we see the first higher term of Kamata-Nishimura series gives the universal function of asymptotic single scattering term and the acceleration term of central gaussian distribution proportional to $\ln\nu t$ in the ionization process.

5 Asymptotic Distribution at Large Angle

We want to investigate the asymptotic feature of Molière angular distribution at large angle in the ionization process under the massless approximation. Integrating the single scattering formula (2) from the incident point to the observation level, we get

$$\begin{aligned}
2\pi\theta d\theta\int_0^t\sigma(\theta)dt' &= \frac{2\theta d\theta}{\Omega}\theta^{-4}\int_0^t\frac{K^2}{E'^2}dt' \\
&= \frac{1}{\Omega}(\frac{\theta}{\theta_G})^{-4}d(\frac{\theta}{\theta_G})^2 \\
&= \frac{1}{B}(\frac{\theta}{\theta_M})^{-4}d(\frac{\theta}{\theta_M})^2, \qquad (46)
\end{aligned}$$

where we used the relation (10). This result shows that the asymptotic feature of Molière angular distribution at large angle is also explained by the accumulation of single scatterings in the ionization process as done in the fixed-energy process.

6 Molière Angular Distribution with Ionization in Nonrelativistic Condition

Kamata and Nishimura submitted their Molière theory in the relativistic condition. We want here to certify a little cares in constructing Kamata-Nishimura formulation of the theory in the nonrelativistic condition, with ionization.

The diffusion equation is already described in Eq. (1):

$$\frac{\partial f}{\partial t}=\iint f(\vec{\theta}-\vec{\theta'})-f(\vec{\theta})\}\sigma(\vec{\theta'})d\vec{\theta'}+\varepsilon\frac{\partial f}{\partial E},$$

where the single scattering formula $\sigma(\vec{\theta})$ is described in Eq. (2). If we assume the energy E uniquely depends on the traversed thickness t without fluctuation, then the last term of the

diffusion equation dissapears. Applying Hankel transforms we get

$$\frac{\partial \tilde{f}}{\partial t} = -\frac{\zeta^2}{w^2}\tilde{f}\{1 - \frac{1}{\Omega}\ln\frac{\zeta^2}{w^2/\beta'^2}\}. \tag{47}$$

We defined

$$w = 2pv/K = \frac{2E}{K}\{1 - (\frac{mc^2}{E})^2\}, \tag{48}$$

$$\beta'^2 = \frac{1.13 + 3.76\alpha^2}{1.13 + 3.76\alpha_0^2}\beta^2, \tag{49}$$

where

$$\alpha = zZ/(137\beta) \qquad \text{and} \qquad \alpha_0 = Z/137. \tag{50}$$

Introducing the gaussian mean square angle as

$$\theta_G^2 = \int_0^t \frac{4}{w^2}dt, \tag{51}$$

and assuming the solution as

$$\tilde{f} = \frac{1}{2\pi}\exp\{-\frac{\theta_G^2\zeta^2}{4}(1 - \frac{1}{\Omega}\ln\frac{\theta_G^2\zeta^2}{4\nu t/\beta'^2})\}, \tag{52}$$

then we get the differntial equation for the unknown function ν,

$$\frac{\partial}{\partial t}\ln(\nu t/\beta'^2) + \frac{4}{w^2\theta_G^2}\ln(\nu t/\beta'^2) = \frac{4}{w^2\theta_G^2}(1 - \ln\frac{4\beta'^2}{w^2\theta_G^2}). \tag{53}$$

We can solve the equation as

$$\begin{aligned}\ln(\nu t/\beta'^2) &= \exp\{-\int_{t_0}^t \frac{4dt}{w^2\theta_G^2}\}\int_0^t [\frac{4}{w^2\theta_G^2}(1 - \ln\frac{4\beta'^2}{w^2\theta_G^2})\exp\{\int_{t_0}^t \frac{4dt}{w^2\theta_G^2}\}]dt \\ &= 1 - \frac{1}{\theta_G^2}\int_0^t \frac{4}{w^2}\ln\frac{4\beta'^2}{w^2\theta_G^2}dt,\end{aligned} \tag{54}$$

so that we get

$$\ln(\nu/\beta'^2) = \ln\frac{\theta_G^2}{4t} + \frac{4}{\theta_G^2}\int_0^t \frac{\ln(w^2/\beta'^2)}{w^2}dt. \tag{55}$$

ν in case of $\beta' \approx \beta$, which is realized e.g. when a singly charged particle traverses through a light media of $Z \ll 137$, is indicated in Fig. 1, revised from the last meeting.

Using the translation formula proposed in the last meeting [1], we find the angular distribution is expreesed by the traditional Molière series, where the expansion parameter B and the unit of Molière variable are determined by

$$B - \ln B = \Omega - \ln\Omega + \ln\frac{\nu t}{\beta'^2}, \tag{56}$$

$$\theta_M = \theta_G\sqrt{\frac{B}{\Omega}}. \tag{57}$$

The results even show full compatible relations with Molière-Bethe one at the fixed-energy limit.

It should be noticed that especially in case of the ionization loss of a constant rate of Eq. (13), the gaussian mean square angle defined in Eq. (51) is explicitly expressed as

$$\theta_G^2 = \frac{K^2}{2\varepsilon}\{\frac{1}{pv} - \frac{1}{p_0v_0} + \frac{1}{2mc^2}\ln\frac{(E_0 - mc^2)/(E - mc^2)}{(E_0 + mc^2)/(E + mc^2)}\}. \tag{58}$$

7 Recipe for Getting Molière Angular Distribution with Ionization (Revised)

We summarize here the sequence of getting the Molière angular distribution $f(E_0, t, \theta)\theta d\theta$ of charged particles starting with incident energy of E_0 and having traversed thickness of x in g/cm^2 or $t = x/X_0$ in radiation unit [8], assuming ionization loss with a constant rate. We use the scattering constants K and Ω defined by Kamata and Nishimura [2, 3].

At first we should get the scale factor ν,

$$\frac{\nu}{\beta'^2} = \frac{\theta_G^2}{4t} \exp \frac{4}{\theta_G^2} \int_0^t \frac{\ln(w^2/\beta'^2)}{w^2} dt\},$$

using

$$w = 2pv/K \quad E = E_0 - \varepsilon t,$$

and

$$\theta_G^2 = \frac{K^2}{2\varepsilon}\{\frac{1}{pv} - \frac{1}{p_0 v_0} + \frac{1}{2mc^2} \ln \frac{(E_0 - mc^2)/(E - mc^2)}{(E_0 + mc^2)/(E + mc^2)}\},$$

where β'^2 is defined by

$$\beta'^2 = \frac{1.13 + 3.76\alpha^2}{1.13 + 3.76\alpha_0^2}\beta^2, \qquad \alpha = zZ/(137\beta), \qquad \text{and} \qquad \alpha_0 = Z/137.$$

Then we can get our distribution by the usual Molière function:

$$f(E_0, t, \theta)\theta d\theta = [f^{(0)}(\vartheta) + B^{-1} f^{(1)}(\vartheta) + B^{-2} f^{(2)}(\vartheta) + \cdots]\vartheta d\vartheta,$$

where the Molière expansion parameter B is got by

$$B - \ln B = \Omega - \ln \Omega + \ln \frac{\nu t}{\beta'^2},$$

and the Molière angle is defined by

$$\vartheta = \theta/\theta_M \quad \text{and} \quad \theta_M = \theta_G \sqrt{B/\Omega}.$$

8 Conclusions and Discussions

The mechanism of depth-variation of Molière angular distribution was investigated using Kamata-Nishimura formulation of Molière theory. Molière process was well understood by separating the single scattering formula σ into two parts, moderate small angle scattering σ_M and the low-frequency large angle scattering σ_L, by the discriminating angle θ_D.

In case of fixed-energy process, Kamata-Nishimura takes the discriminating angle θ_D a constantant factor $e^{\Omega/2}$ times as large as the screening angle $\sqrt{e}\chi_a$. Then the moderate small angle scattering gives the traditional Fermi distribution derived by the gaussian approximation [8]. But the central gaussian distribution is corrected by the first higher term of the solution so that the width of the distribution increases much more rapid than $\sqrt{t}$ along the traversed thickness.

Molière-Bethe takes the discriminating angle θ_D an increasing factor $e^{B/2}$ times as large as the screening angle $\sqrt{e}\chi_a$. Then the moderate small angle scattering gives the gaussian distribution with the width increasing with θ_M which is more rapid than $\sqrt{t}$. But in this case the central gaussian distribution is not corrected by the first higher term of the solution.

In case of ionization process, the screening angle $\sqrt{e}\chi_a$, as well as the discriminating angle θ_D in Kamata-Nishimura formulation, increases with traversed thickness due to the decrease of energy. If we take the discriminating angle θ_D constant by the value at the geometrical mean enegy $\sqrt{E_0 E}$, the scale factor ν, which is characteristic to the ionization process, appears as a compensation.

These investigations will help us understand the properties of Molière process with ionization much more.

Acknowledgments

The author wishes to express his thanks to Prof. J. Nishimura for continuous discussions about the contents.

References

1) T. Nakatsuka, *"Proceedings of the Seventh EGS4 User's Meeting in Japan,"* KEK Proceedings 98-7, 13(1998).

2) K. Kamata and J. Nishimura, Prog. Theor. Phys. Suppl. **6**, 93(1958).

3) J. Nishimura, in *Handbuch der Physik, Band 46*, edited by S. Flügge (Springer, Berlin, 1967), Teil **2**, p. 1.

4) G. Molière, Z. Naturforsch. **2a**, 133(1947).

5) G. Molière, Z. Naturforsch. **3a**, 78(1948).

6) H.A. Bethe, Phys. Rev. **89**, 1256(1953).

7) T. Nakatsuka, *"Proceedings of the 26th International Cosmic Ray Conference,"* Salt Lake City, Utah, 1999, Vol. 1, p.522.

8) B. Rossi and K. Greisen, Rev. Mod. Phys. **27**, 240(1941).

9) T. Nakatsuka, Phys. Rev. **D58**, 056002(1998).

10) W.T. Scott, Rev. Mod. Phys. **35**, 231(1963).

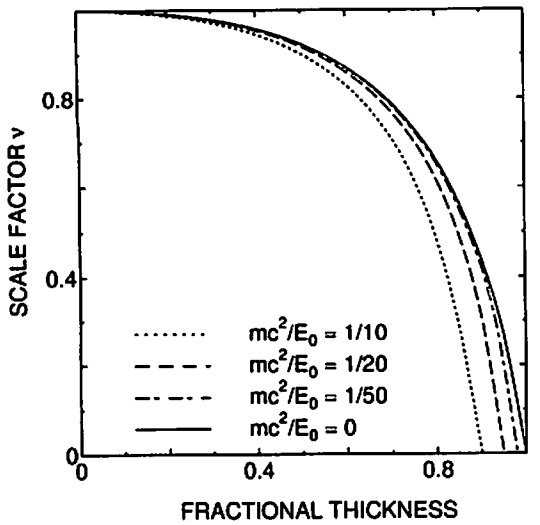

Figure 1: Variation of the scale factor ν against t, at $\beta' \approx \beta$. Abscissa means $t/(E_0/\varepsilon)$. The curves correspond to incident energies $E_0/(mc^2)$ of 10, 20, 50, and ∞.

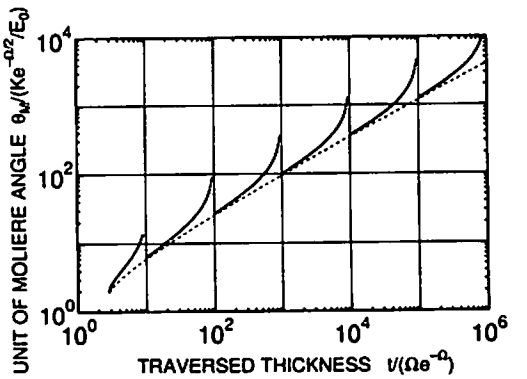

Figure 3: Depth-variation of the unit of Molière angle θ_M for various incident energies, E_0/ε of 10, 10^2, 10^3, 10^4, 10^5, and 10^6 in unit of $\Omega e^{-\Omega}$. Dot line indicates traditional θ_M without ionization.

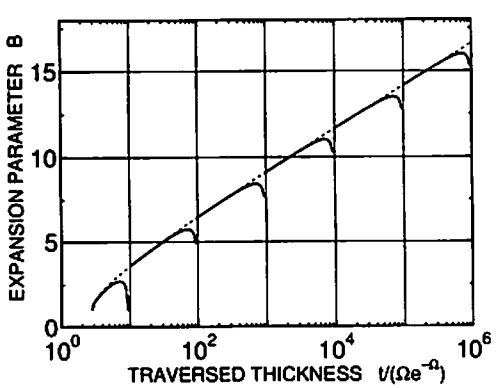

Figure 2: Depth-variation of expansion parameter B for various incident energies, E_0/ε of 10, 10^2, 10^3, 10^4, 10^5, and 10^6 in unit of $\Omega e^{-\Omega}$. Dot line indicates traditional B without ionization.

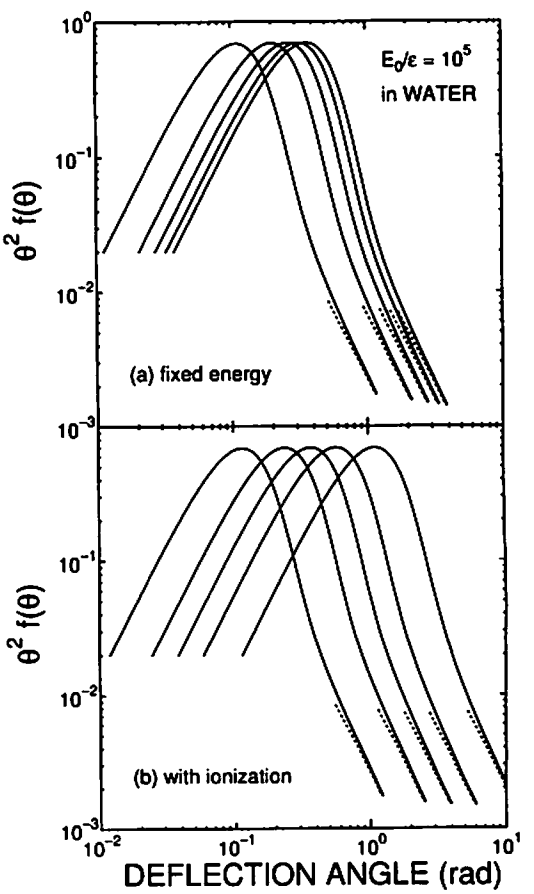

Figure 4: Angular distributions multiplied by θ^2. Solid lines correspond to those at $t/(E_0/\varepsilon)$ of 0.1, 0.3, 0.5, 0.7, and 0.9 from left to right. Dot lines indicate accumulations of single scatterings.

CONSTRUCTION OF OPTIMUM COMPENSATION SHIELDS IN A DUCT STREAMING SYSTEM

K. UEKI and M. KAWAI[1]

Nuclear Technology Division Ship Research Institute
6-38-1 Shinkawa, Mitaka, Tokyo 181-0004, Japan
[1]*Neutron Science Research Facility*
High Energy Accelerator Research Organization
1-1 Oho, Tsukuba, Ibaraki 305-0801, Japan

Abstract

In this study, a two-bend (three-legged) cylindrical duct of 10 cm-diameter is placed in a concrete shield of 2 m-thick, and an point isotropic neutron source of 14 MeV is located at 50 cm in front of the duct inlet. The ten FCs (flagging cells) are located around the duct and the contribution from each FC to the dose-equivalent rate at the duct outlet is obtained by the MCNP 4B code with the cell flagging card. The FCs are regarded as concrete in the first calculation, then they are partly replaced with the compensation shields of the NS-4-FR successively.

As the results, by replacing the five FCs located from the outlet of the second leg to the outlet of the third leg with the shields, the dose-equivalent rate at the outlet is reduced below the dose of no duct. The other FCs can not reduce the dose to the level of no duct. Therefore, the optimum compensation shielding is constructed with the five FCs around the duct. Moreover, it is expected that the equilibrating contribution from each FC to the dose-equivalent rate at the duct outlet is the essential function to make the optimum compensation shielding system with neutron streaming.

1 Introduction

In the Monte Carlo calculation, the history of a particle is tracked in a shielding system in accordance with the probability low, so that it enables us to recognize each course that the particles passed through. In the continuous energy Monte Carlo code MCNP 4B, the passage of a particle is recognized with the cell flagging card[1]. Only the particles passed through the flagging cell or surface are flagged and the other particles are not flagged. Accordingly, the flagged particles and the non-flagged particles are distinguished in the detector. In the previous study, the neutron streaming experiment with three straight ducts in the thick iron slab[2] was analyzed by the cell flagging card[3]. The ratios of the neutron response passed through the flagging cell located at the duct inlet to the total neutron response (flagged and non-flagged neutron response) were obtained as a function of the detector locations in the duct. In addition, the streaming system with a two-bend duct in the thick concrete slab was calculated. The contribution of neutron fluxes passed through the flagging cells set in several locations around the duct to the detector located at the outlet of the duct was analyzed. Thus, the optimum location for setting a compensation shield can be comprehended in the duct shielding system. In the multi group Monte Carlo code MORSE-CG 4, there is no such

a cell flagging card of the MCNP 4B code. Accordingly, users have to supply some subroutines in the MORSE-CG code by themselves to do the flagging cell calculation like the MCNP 4B code.

In this study, a shielding system with a two-bend cylindrical duct in a thick concrete shield is established and a point isotropic source of 14 MeV-neutrons is located in front of the duct inlet. The FCs are located around the duct. The system proposes two shielding problems. One is a conventional radiation-streaming problem. The other is how to construct the optimum compensation shields, which reduce the dose-equivalent rate at the duct outlet as low as the dose of no duct by employing the compensation shields of the NS-4-FR around the duct. Pursuing the minimum volume, the proper location and the configuration of the shield around the duct will solve it. The later is the main problem in the present study.

2 Shielding System and Compensation Shields

(i) Shielding System: A two-bend (three-legged) cylindrical duct is set in a 2m thick concrete shield. As shown in Fig. 1, the duct bends by an angle of 45 deg. at 50 cm from the duct inlet and also bends by an angle of 45 deg. at 150 cm. The duct is 10 cm-diameter and it is made of stainless steel 0.5 cm-thick. In order to obtain the neutron dose-equivalent rates, Detector Cell 1 and Detector Cell 2 are located at the duct inlet and the duct outlet, respectively.

(ii) Source Conditions: A point isotropic source of 14 MeV neutrons is located at 50 cm in front of the duct inlet.

(iii) Compensation Shields: The basic configuration of the compensation shields is annular cylinder of inner radius 5.5 cm, outer radius 25.5 cm, and 10 cm-high. The duct bends by an angle of 45deg., so that configuration of the shields are a little bit modified at the bent parts of the duct as shown in Fig. 1, but the volume of 1.948×10^4 cm^3 is the same as the basic one. Ten compensation shields in all are set at the inlet and the outlet of the duct, and around the bent parts of it. The shields are made of the NS-4-FR, which is a kind of epoxy resins and contains approximately 1 w/o of boron to reduce secondary gamma rays.

According to the shielding experiment with a ^{252}Cf neutron source of average energy of 2.35 MeV, the shielding ability of the NS-4-FR is better than that of water and much better than that of concrete. The tenth-layer of the neutron dose-equivalent rate for the NS-4-FR, water and ordinary concrete is 14.5 cm-thick, 16.5 cm-thick and 28.0 cm-thick for the ^{252}Cf neutron source5, respectively. Because of the NS-4-FR containing approximately 21 w/o of aluminum[5], which has relatively large inelastic cross sections to high-energy neutrons, good shielding ability of the NS-4-FR is more expected than that of water for higher energy of 14 MeV neutrons.

3 Monte Carlo Techniques and Procedures

In order to investigate the contribution from each compensation shield to the detector located at the duct outlet, CF (cell flagging) card in the continuous energy Monte Carlo code MCNP 4B1 is employed in the calculations. As an example of applying the CF card, the three-straight-rectangular-ducts streaming experiment with 14 MeV neutrons at the OCTAVIAN of Osaka University2 was analyzed by the MCNP 4B code. The CF card was used to investigate the contribution from a flagging cell located at the inlet of an outer duct of the three-straight-rectangular-ducts to the detector located at the outlet of it. As the results, the contribution from the flagging cell to the detector was cleard[3].

In this study, the CF card with ten flagging cells (FC1, FC2, $\cdots$ FC10) are located as indicated in Fig. 1. In the first calculation, all the flagging cells are not regarded as the compensation

shields but as the same concrete around the duct. In this way, not only the dose-equivalent rates at the duct inlet and the outlet but also the contributions from the flagging cells to the detector at the duct outlet are calculated. In the next calculation, some cells are selected and the selected cells are replaced with the compensation shields of the NS-4-FR. After that, in the same way, calculations are repeated, changing the selected cells. Consequently, the dose-equivalent rate and the dose contributed from the flagging cells, of which some cells are concrete and the others are the NS-4-FR, are obtained separately in the detector located at the duct outlet. As the estimator, the track length estimator is employed in the present calculations.

In case of no duct, the dose-equivalent rate at the corresponding location to the duct outlet is obtained by replacing the void and the stainless steel of the duct with the concrete around it. Then, at the duct outlet, the dose without the duct is compared to it with the duct and the compensation shields. By comparing, the following two items are cleared : (i) Which compensation shield is more effective to reduce the dose-equivalent rate at the outlet. (ii) How many compensation shields are required to reduce it under the dose of no duct. As the results, the construction of the optimum compensation shields will be possible. The Detector I is located at the duct inlet and the Detector II is at the duct outlet, so that the ratio of the dose-equivalent rate at the inlet to the outlet is obtained. The ratio is an index of the shielding effect for the compensation shields.

4 Results and Discussions

At first, in case of no duct, the neutron dose-equivalent rates are obtained at the corresponding locations to the duct inlet and the outlet in the concrete bulk shield in Fig. 1. (1),(2) in the following table is at the corresponding location to the duct inlet and the duct outlet, respectively. The final goal is to reduce the dose-equivalent rate below the value of (2) by employing the compensation shields.

(1)	Neutron Dose-Equivalent Rate at the Duct Inlet (Detector Cell 1): 7.57×10^{-8}(μSv/h/source neutron/s)
(2)	Neutron Dose-Equivalent Rate at the Duct Outlet (Detector Cell 2): 3.19×10^{-14}(μSv/h/source neutron/s)
	(1)/(2) = $1/2.37 \times 10^{6}$

4.1 Discussion of Fig. 2

In this calculation, FC1, FC2, $\cdots$ FC10 in Fig. 1 are not regarded as the compensation shields but as concrete. The neutron dose-equivalent rate at the duct outlet and the contribution of neutrons passed through each FC to the dose are shown in Fig. 2 and the numerical values are in the following table.

Neutron Dose-Equivalent Rate at the Duct Outlet (Detector Cell 2): 1.04×10^{-13} (μSv/h/source neutron/s)			
Contribution of Neutrons Passed through each FC to the above dose-equivalent rate			
From FC1	27 (%)	From FC6	53 (%)
From FC2	19 (%)	From FC7	63 (%)
From FC3	21 (%)	From FC8	59 (%)
From FC4	25 (%)	From FC9	55 (%)
From FC5	30 (%)	From FC10	47 (%)

As the results, the contributions from FC1 $\sim$ FC5 located around the first leg are relatively small, but the contributions from FC6 $\sim$ FC10 located around the outlet of the second leg and the third leg are large. Accordingly, it is estimated that the compensation shields of FC6 $\sim$ FC10 are more effective for reducing the neutron dose-equivalent rate at the duct outlet than those of FC1 $\sim$ FC5. In the above table, the neutron dose-equivalent rate at the duct outlet is 1.04×10^{-13} (μSv/h/source neutron/s). It is larger than the dose of 3.19×10^{-14} (μSv/h/source neutron/s) without the duct by a factor of 3.26.

4.2 Discussion of Fig. 3

Considering the discussion of Fig. 2, the compensation shields are set to FC1, FC2, and FC3, and the rest cells are concrete. These FCs are near the duct inlet. Contributions of neutrons passed through these FCs are shown in Fig. 3 and the numerical data is in the following table.

Neutron Dose-Equivalent Rate at the Duct Outlet (Detector Cell 2): 9.94×10^{-14} (μSv/h/source neutron/s)			
Contribution of Neutrons Passed through each FC to the above dose-equivalent rate			
From FC1	20 (%)	From FC6	60 (%)
From FC2	11 (%)	From FC7	68 (%)
From FC3	16 (%)	From FC8	56 (%)
From FC4	26 (%)	From FC9	53 (%)
From FC5	31 (%)	From FC10	45 (%)

The amount of the contributions from FC1, FC2, and FC3 are reduced a little. However, as expected from the discussion of Fig. 2, the magnitude of the contribution from these FCs is so small that the essential reduction of the neutron dose-equivalent rate is not observed at the duct outlet.

4.3 Discussion of Fig. 4

Next, FC6, FC7 and FC8, which make the most of a contribution to the dose-equivalent rate at the duct outlet, are replaced with the compensation shields, and the rest cells are concrete. The contributions of neutrons passed through these FCs are shown in Fig. 4 and the numerical data is indicated in the following table.

Neutron Dose-Equivalent Rate at the Duct Outlet (Detector Cell 2): 3.99×10^{-14} (μSv/h/source neutron/s)			
Contribution of Neutrons Passed through each FC to the above dose-equivalent rate			
From FC1	29 (%)	From FC6	33 (%)
From FC2	20 (%)	From FC7	37 (%)
From FC3	29 (%)	From FC8	33 (%)
From FC4	24 (%)	From FC9	43 (%)
From FC5	26 (%)	From FC10	58 (%)

The neutron dose-equivalent rate at the duct outlet decreases to 3.99×10^{-14} (μSv/h/source neutron/s) and the dose is a factor of approximately 1.25 of it without the duct. The considerable

dose reduction is due to effective function of FC6, FC7, and FC8 filled with the NS-4-FR. This reduction phenomenon is also understood by the fact that the contributions from FC6, FC7, and FC8 to the dose-equivalent rate at the duct outlet are about 1/2 of those in Fig. 3. Furthermore, it is clear that the contribution from FC10, which is located outside the duct outlet, occupies 58 % of the dose at the duct outlet, so FC10 is an important cell to reduce the dose.

4.4 Discussion of Fig. 5

Owing to the discussion of Fig. 4, the contribution from FC10 is large at the duct outlet. Accordingly, FC8, FC9, and FC10 are replaced with the compensation shields, and the rest cells are concrete. The results are shown in Fig. 5 and the numerical number is in the following table.

Neutron Dose-Equivalent Rate at the Duct Outlet (Detector Cell 2): 4.89×10^{-14} (μSv/h/source neutron/s)			
Contribution of Neutrons Passed through each FC to the above dose-equivalent rate			
From FC1	24 (%)	From FC6	61 (%)
From FC2	19 (%)	From FC7	68 (%)
From FC3	20 (%)	From FC8	36 (%)
From FC4	23 (%)	From FC9	31 (%)
From FC5	25 (%)	From FC10	30 (%)

As expected, the contribution from FC10 decreases to approximately 1/2 of the value in Fig. 4. On the other hand, the contributions from FC6 and FC7 increases by a factor of two, and the dose equivalent rate at the duct outlet also increases by 23 the dose at the duct outlet is a factor of 1.53 of the dose without the duct. Therefore, FC6, FC7, and FC8, which are located at the second bent part, perform the essential function to reduce the dose-equivalent rate at the duct outlet below the dose of no duct.

4.5 Discussion of Fig. 6

Indeed, the compensation shields of FC6, FC7, and FC8 perform the essential function to reduce the dose-equivalent rate. However, from the above discussion, it is very difficult to reduce the dose below one of no duct by employing the three shields of FC6, FC7, and FC8. Accordingly, FC6, FC7, FC8, and FC9 are replaced with the compensation shields and the rest cells are concrete. The results are shown in Fig. 6 and the numerical data is in the following table.

Neutron Dose-Equivalent Rate at the Duct Outlet (Detector Cell 2): 3.43×10^{-14} (μSv/h/source neutron/s)			
Contribution of Neutrons Passed through each FC to the above dose-equivalent rate			
From FC1	28 (%)	From FC6	30 (%)
From FC2	23 (%)	From FC7	35 (%)
From FC3	25 (%)	From FC8	32 (%)
From FC4	24 (%)	From FC9	33 (%)
From FC5	24 (%)	From FC10	60 (%)

Consequently, the contributions from FC1 to FC9 are almost the same as 25~35 %, except for 60 % of FC 10. The neutron dose-equivalent rate at the duct outlet decreases to 3.43×10^{-14}

(μSv/h/source neutron/s) and this dose is a factor of 1.075 of it without the duct. Therefore, it might be possible to reduce the dose-equivalent rate below of no duct by replacing one more FC with the compensation shield.

4.6 Discussion of Fig. 7

Finally, FC10 is added to the compensation shields of the NS-4-FR in Fig. 6. The contribution from FC10 is clarified in Fig. 7 and the numerical values are in the following table.

Neutron Dose-Equivalent Rate at the Duct Outlet (Detector Cell 2): 2.78×10^{-14} (μSv/h/source neutron/s)			
Contribution of Neutrons Passed through each FC to the above dose-equivalent rate			
From FC1	25 (%)	From FC6	37 (%)
From FC2	29 (%)	From FC7	41 (%)
From FC3	22 (%)	From FC8	44 (%)
From FC4	22 (%)	From FC9	49 (%)
From FC5	22 (%)	From FC10	37 (%)

The neutron dose-equivalent rate at the duct outlet decreases to 2.78×10^{-14} (μSv/h/source neutron/s) and the dose is a factor of 0.87 of it without the duct. At last, due to replacing FC6 $\sim$ FC10 with the compensation shields of the NS-4-FR, the dose at the duct outlet is reduced below of no duct. Therefore, it is concluded that the optimum compensation shielding system is established for the neutron-streaming problem in Fig. 1. The contributions from FC1 $\sim$ FC10 to the dose-equivalent rate at the duct outlet are almost the same as 35$\pm$10 %. Accordingly, it is expected that equilibrating the contribution from each FC to the dose-equivalent rate at the duct outlet is the essential function to make the optimum compensation shielding system with the neutron streaming.

5 Concluding Remarks

In this study, a two-bend (three legged) duct of 10 cm-diameter is made in a concrete shield of 2 m-thick, and an point isotropic neutron source of 14 MeV is located at 50 cm in front of the duct inlet. The ten FCs are located around the duct. The FCs are regarded as concrete in the first calculation, and the contribution from each FC to the dose-equivalent rate at the duct outlet is cleared. Consequently, the contributions from the FCs located around the outlet of the second leg and the inlet of the third leg is larger than that of the others. In order to establish the optimum compensation shielding system, according to size of the contribution to the dose-equivalent rate at the duct outlet, the FCs of concrete are replaced with the compensation shields of the NS-4-FR successively.

As the results, by replacing the five FCs located from the outlet of the second leg to the outlet of the third leg with the shields, the dose-equivalent rate at the outlet is reduced below the dose of no duct. By replacing the three FCs the rest cells are concrete, and the minimum dose-equivalent rate at the duct outlet is a factor of 1.25 of the dose without the duct. In case of the four FCs the minimum dose is a factor of 1.08, and at last in case of the five FCs the minimum dose is a factor of 0.87, that is, less than 1.0. The locations of the five FCs are from the outlet of the second leg to the outlet of the third leg. Therefore, the optimum compensation shielding is constructed with the five FCs around the duct. Moreover, it is expected that equilibrating the contribution from each FC to the dose-equivalent rate at the duct outlet is the essential function to make the optimum compensation shielding system with neutron streaming.

References

1) "MCNPTM-A General Monte Carlo N-Particle Transport Code Version 4B," J. F. BRIESMEISTER, Ed., *LA-12625-M*, Los Alamos National Laboratory (1997).

2) Y. Oka, et al., "Bench Mark Experiment of Fusion Neutron Streaming through Iron Shields," *OKUTAVIAN Rep. A-88-01*, (1988).

3) K. Ueki and M. Kawai, *Journal of the Atomic Energy Society of Japan*, **Vol. 40**, No. 11, 881(1998), in Japanese.

4) E. A. Straker, P. N. Stevens, D. C. Irving, and V. R. Cain "The MORSE code - A Multi Group Neutron and Gamma-Ray Transport Code," *ORNL-3622* (1965).

5) K. Ueki, et al., "Systematic Evaluation of Neutron Shielding Effects for Materials," *Nucl. Sci. Eng.*, **Vol. 124, No. 3**, 455 (1996).

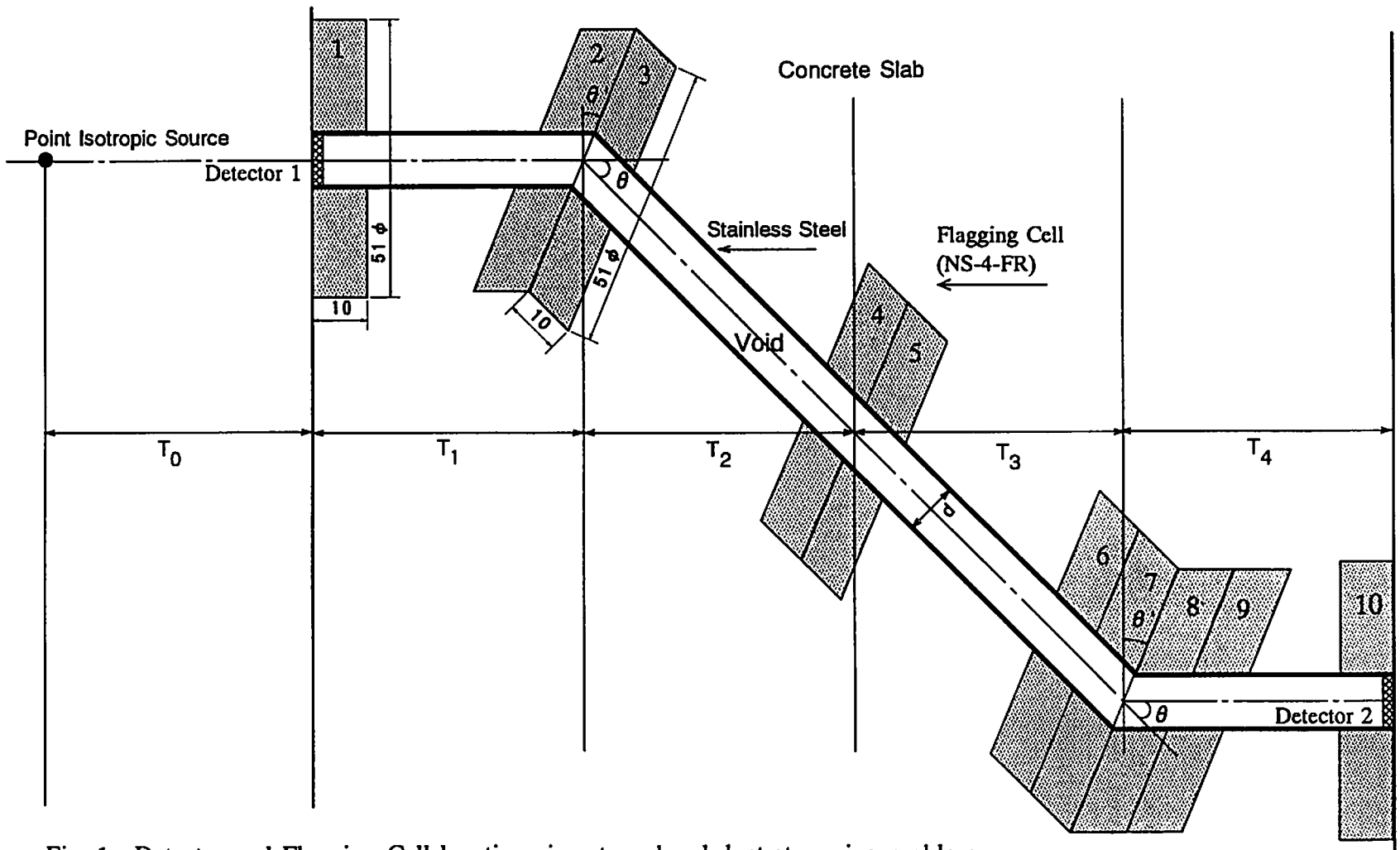

Fig. 1 Detector and Flagging Cell locations in a two -bend duct streaming problem. Source : 14 MeV neutrons, $\theta = 45°$, $\theta' = \theta/2$, d = 10㎝, and $T_0 = T_1 = T_2 = T_3 = T_4 = 50$㎝.

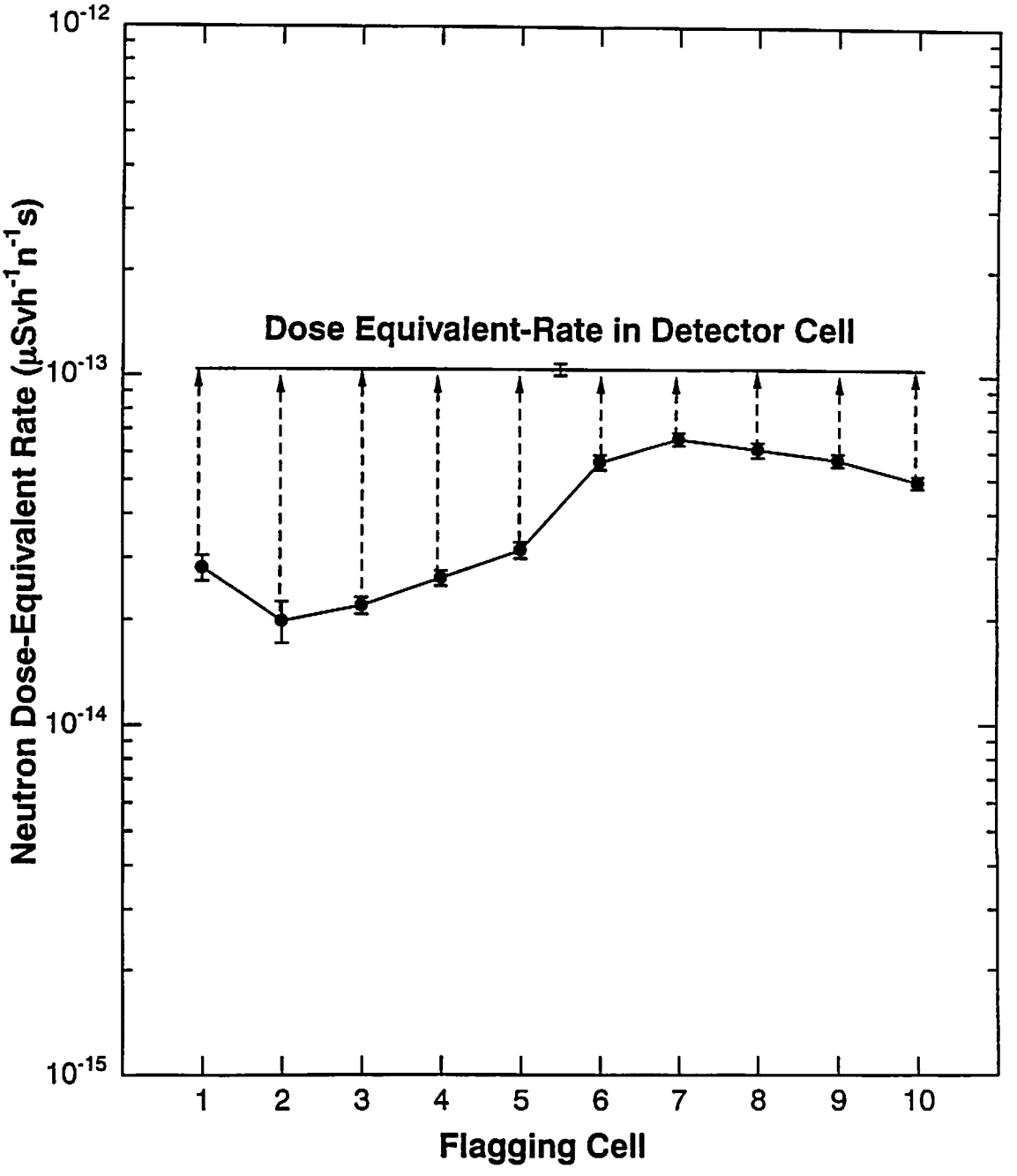

Fig.2 Contribution of neutrons from each flagging cell to the detector cell at the duct end in Fig. 1. All the flagging cells are concrete.

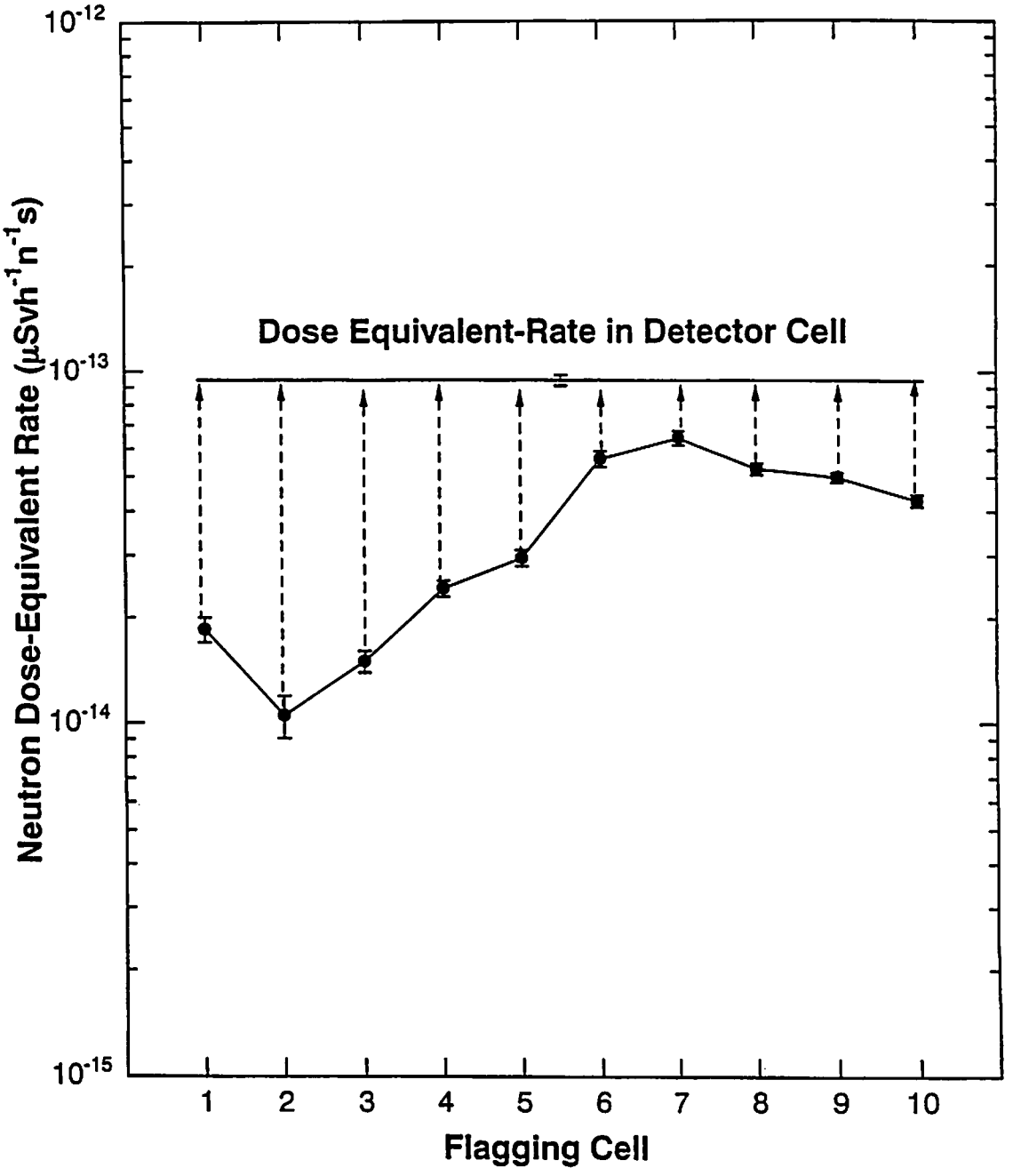

Fig.3 Contribution of neutrons from each flagging cell to the detector cell at the duct end in Fig. 1.
Flagging cells 1,2,3 are NS-4-FR, ohters are concrete.

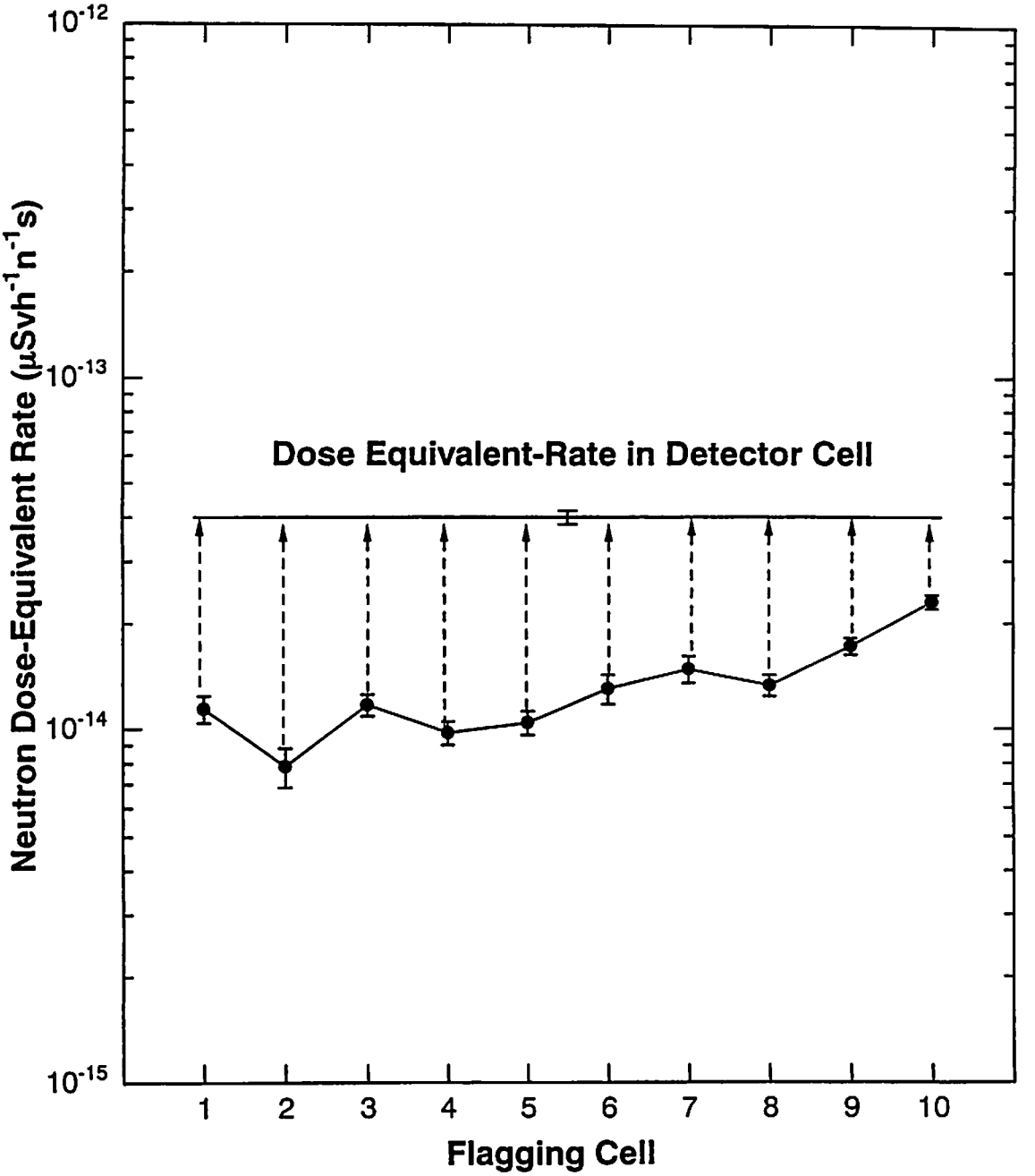

Fig.4 Contribution of neutrons from each flagging cell to the detector cell at the duct end in Fig. 1. Flagging cells 6,7,8 are NS-4-FR, ohters are concrete.

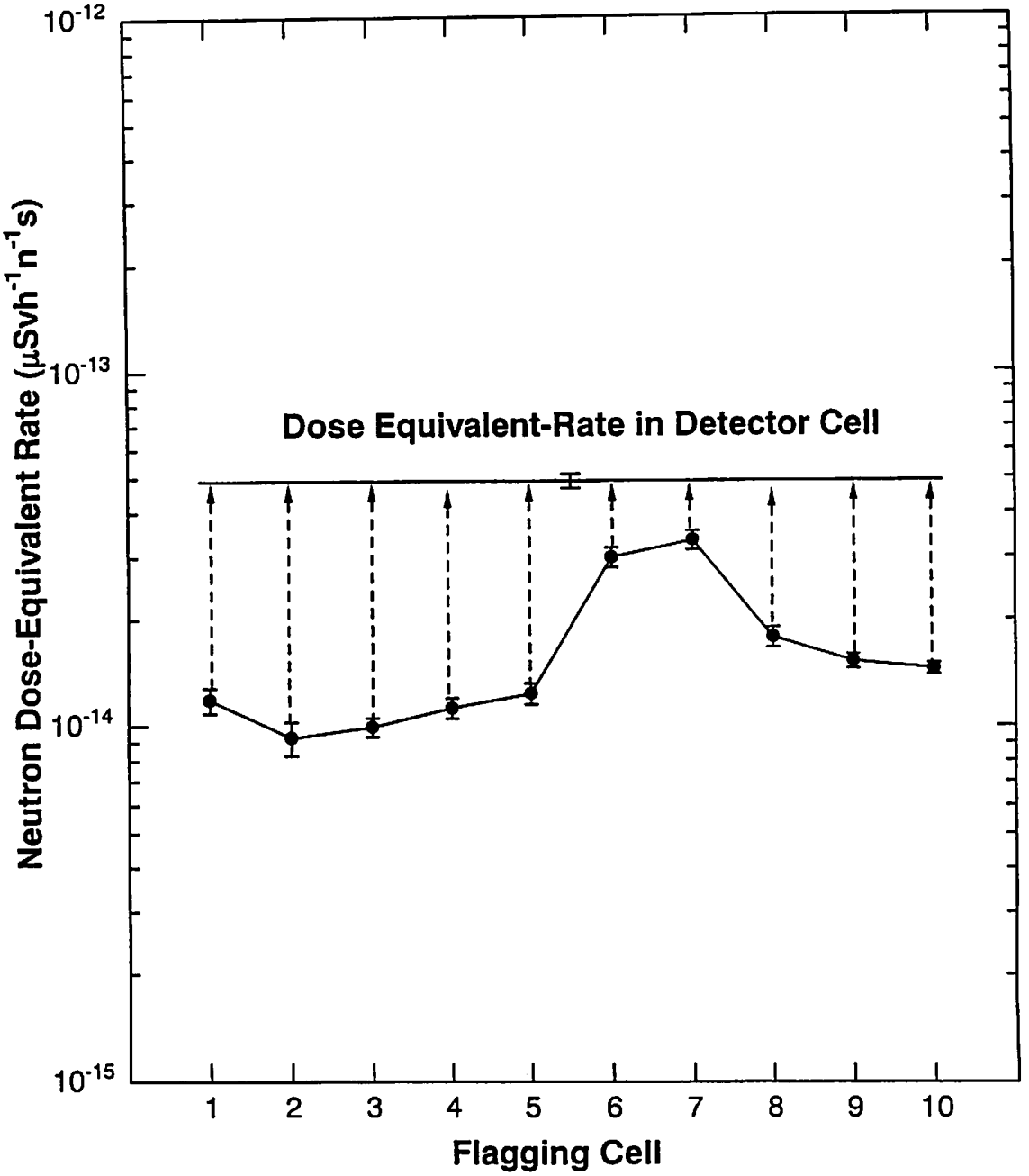

Fig.5 Contribution of neutrons from each flagging cell to the detector cell at the duct end in Fig. 1. Flagging cells 8,9,10 are NS-4-FR, ohters are concrete.

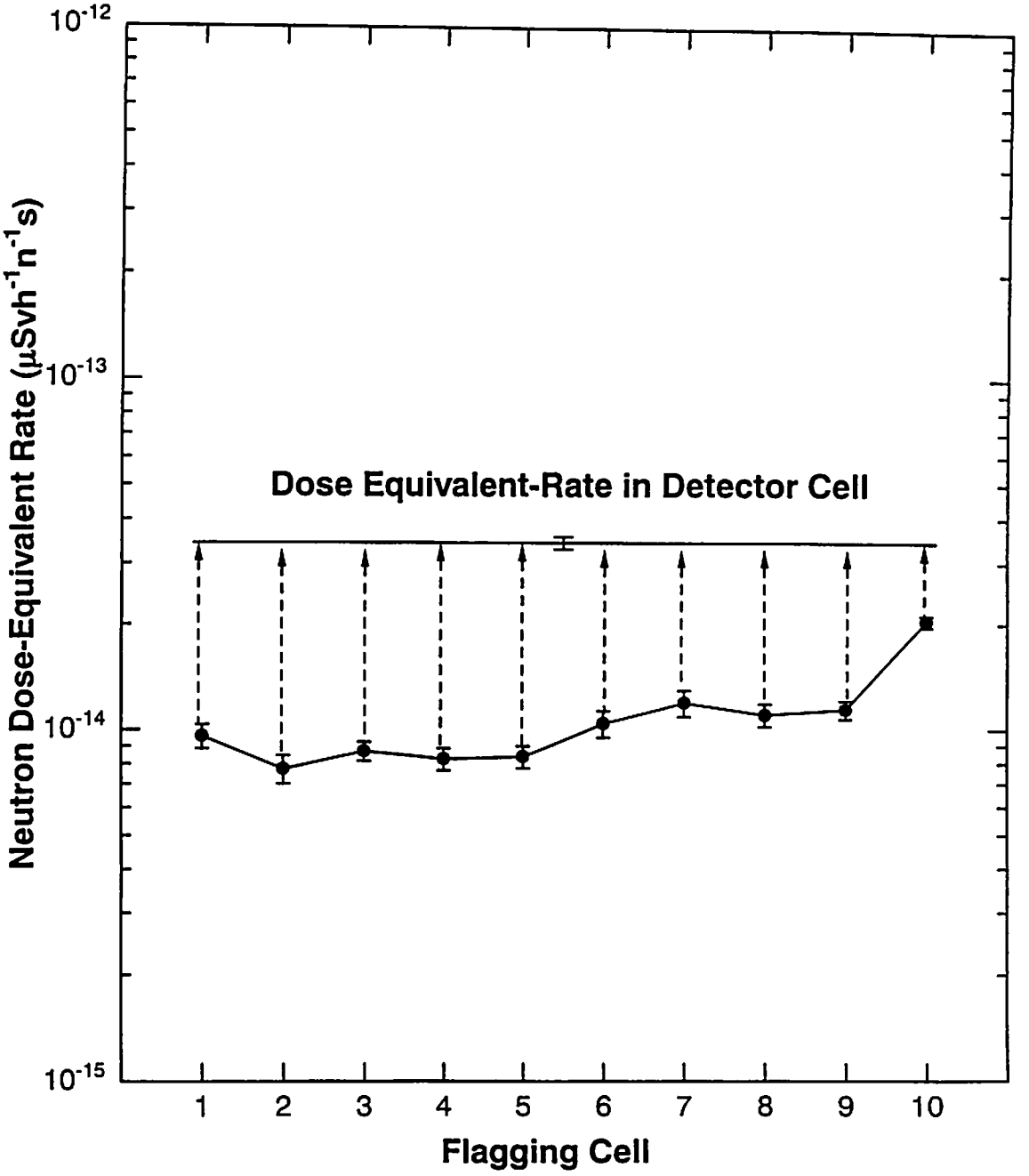

Fig.6 Contribution of neutrons from each flagging cell to the detector cell at the duct end in Fig. 1. Flagging cells 6,7,8,9 ara NS-4-FR, others are concrete.

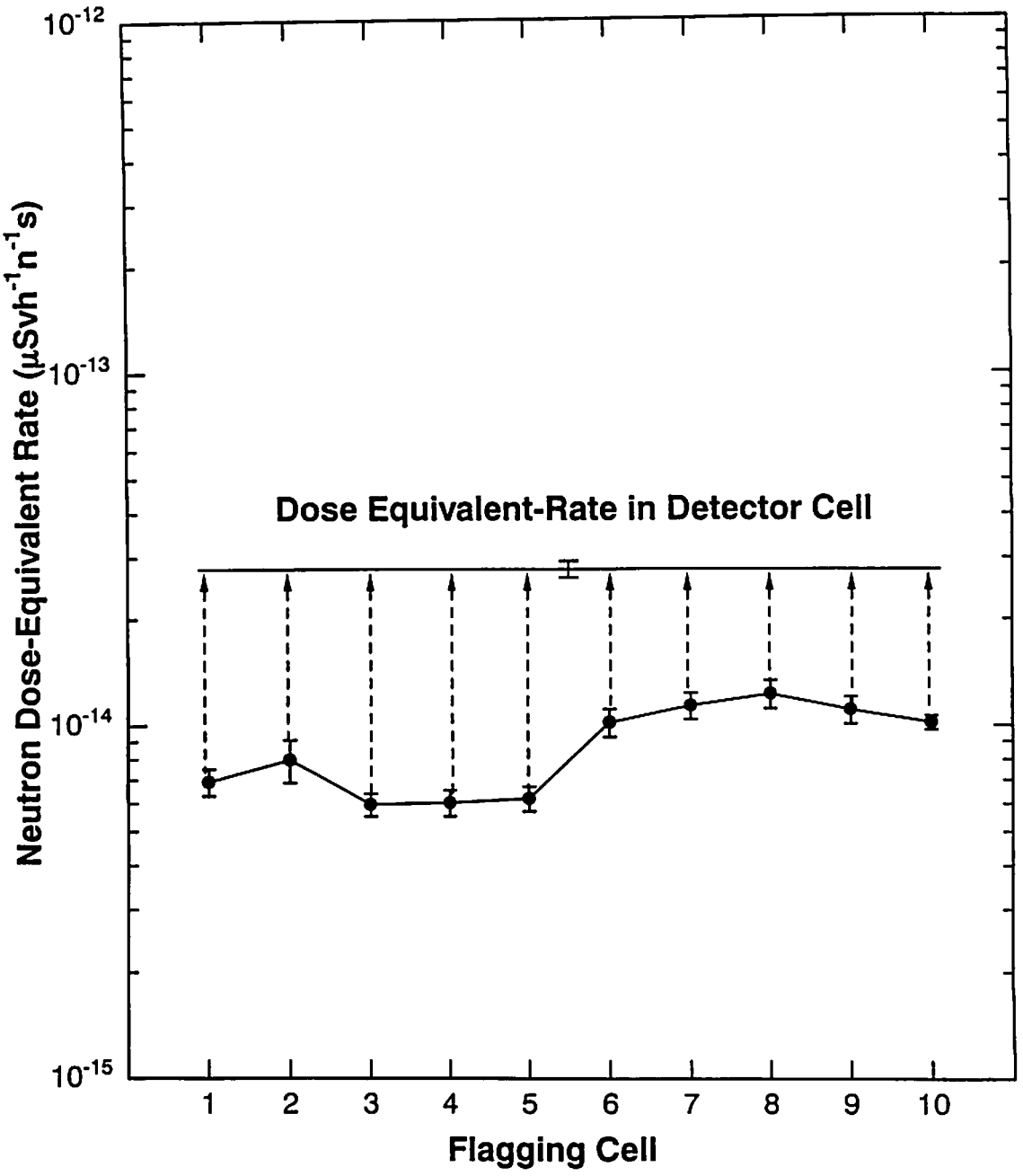

Fig.7 Contribution of neutrons from each flagging cell to the detector cell at the duct end in Fig. 1. Flagging cells 6,7,8,9,10 ara NS-4-FR, others are concrete.

DEVELOPMENT OF β-RAY TOTAL ABSORPTION DETECTOR FOR DETERMINATION OF ATOMIC MASSES

H. UNO, M. SHIBATA, K. KAWADE, Y. KOJIMA[1], A. TANIGUCHI[2], Y. KAWASE[2]

Department of Energy Engineering and Science, Nagoya University
Furo-cho, Chikusa-ku, Nagoya 464-8603, Japan
[1]*Applied Nuclear Physics, Faculty of Engineering, Hiroshima University*
Higashi-Hiroshima 739-8527, Japan
[2]*Research Reactor Institute, Kyoto University*
Kumatori, Sennan, Osaka 590-0494, Japan

Abstract

We are developing three new-type β-ray detectors for determination of atomic masses. The response functions for monoenergetic electrons were simulated by EGS4 and their detection efficiencies were evaluated. The expected β-ray spectra were also simulated and the effectiveness of them was discussed.

1 Introduction

Atomic masses are fundamental physical constants and contribute to development of mass formula. They are also necessary for astrophysics and nuclear engineering. A β-decay energy (Q_β) measurement is one of precise and reliable measurements for determination of atomic masses. We have been measured Q_β using a small planar type Ge detector [1-2]. For high energy Q_β determination of weak radioactivity, we are developing new-type β-ray detectors which can detect scattering electrons and/or bremsstrahlung photons with high efficiency [3], those are a sum-type Ge detector, a well-type Ge detector and a sum-type BGO scintillation detector. The response for monoenergetic electrons and β-ray spectra have been simulated. The effectiveness of new-type detectors has been evaluated by simulation.

2 Simulation for Monoenergetic Electrons and β-Rays

Figure 1 shows escape ratios of scattering electrons and bremsstrahlung photons from a Ge crystal (36mmϕ× 13mmt, LEPS (ORTEC)) for incident monoenergetic electrons as shown in an inset. The "Peak" represents full energy absorption in the Ge crystal. The "back-scatt.", "side-scatt." and "forward" represent the escapes of each direction for scattering electrons or bremsstrahlung photons. These results show that the efficiencies increase when scattering electrons and bremsstrahlung photons can be detected.

A Ge crystal which has a good energy resolution and has a volume large enough to detect bremsstrahlung photons is favorable detector, but it is still difficult to obtained commercially. The sum-type Ge detector (Fig.2(a)) and the well-type Ge detector (Fig.2(b)), which have large solid angle, is considered to be effective in order to detect back-scattering electrons. On the other hand, in spite of its bad energy resolution, a BGO scintillator has large probability of γ-ray absorption. Therefore the sum-type BGO scintillation detector (Fig.2(c)) is considered to be effective for high Q_β measurements, because it can detect not only back-scattering electrons but also bremsstrahlung photons.

2.1 Sum-type Ge detector and Well-type Ge detector

Figure 2(a) and 2(b) show the sum-type Ge detector which is composed of two identical Ge detectors (LEPS(ORTEC) 36mmϕ×13mmt) and the well-type Ge detector (ORTEC), respectively, together with geometrical condition. In the sum-type Ge detector, back-scattering electrons from one Ge crystal can be detected by another one. It measures energy sum of two detectors. Figure 3 shows the detection efficiencies of the sum-type Ge detector, the well-type Ge detector and a single Ge detector for monoenergetic electrons. The response for monoenergetic electrons is simplified as shown in an inset of Fig.3. They are a full energy absorption (A), a bremsstrahlung escape (B) and a scattering escape (C). Here, A/(A+B+C) regards as the detection efficiency. For the sum-type Ge detector, the calculations have done with two geometrical condition. One is, it is impossible in real experiment, adhered two Ge crystals. Another is a realistic geometry (the dotted line), that is two Ge detectors are put 17mm distance.

The efficiency of the well-type Ge detector is larger than that of the single Ge detector by 60% and it is almost same as that of the adhered sum-type Ge detector. This means the well-type Ge detector is more effective than the sum-type Ge detector. The expected β-ray spectrum (Q_β=3.5MeV) with the well-type Ge detector has been simulated (Fig.4). In this energy, the simulated spectrum does not correspond to the theoretical one. This is caused by escapes of some scattering electrons and bremsstrahlung photons. This detector is favorable for Q_β determination with high efficiency but an unfolding procedure with the response functions for monoenergetic electrons is necessary.

The commercially available well-type Ge detector has large energy loss due to Al-housing. The 624keV conversion electrons of ^{137}Cs were measured with the well-type Ge detector. The energy loss was about 200keV. If the housing material can be made by much thinner material, Q_β can be determined much precisely.

2.2 Sum-type BGO scintillation detector

As shown in Fig.1, the percentage of bremsstrahlung photons increases above around 4MeV. A BGO scintillator has large probability of γ-ray absorption. So they can detect bremsstrahlung photons. Fig.2(c) shows a schematic view of the sum-type BGO scintillation detector and electrons behavior in it. The detector is composed of two BGO scintillators (120mmϕ×100mmt). They arranged 180(in close geometry. In this detector, back-scattering electrons can be also detected. It measures energy sum of two BGO crystals. The efficiency of the sum-type BGO scintillation detector is larger than 85% for monoenergetic electrons in an energy range between 1 and 8MeV (Fig.3). This detector is fairy effective for high Q_β measurements. Figure 5 shows an expected β-ray spectrum obtained with this detector (Q_β=3.5MeV). The lower part represents the deviation between the simulated and theoretical β-ray spectrum. They are good agreement each other. This detector is considered to be useful for higher energy Q_β determination more than 5~6MeV like new isotopes in precision of about 0.3MeV.

3 Conclusion

The detection efficiencies of the sum-type detector, the well-type Ge detector and the sum-type BGO scintillation detector were evaluated by simulation of response for monoenergetic electrons. The simulated β-ray spectrum with the sum-type BGO scintillation detector is good agreement with the theoretical β-ray. As the results, it is considered that, the well-type Ge detector is effective for precise measurements, and for high Q_β measurements of weak radioactivity, the sum-type BGO scintillation detector is favorable.

References

1) T. Ikuta, A. Taniguchi, H. Yamamoto, K. Kawade and Y. Kawase, *J. Phys. Soc. Jpn.* **64** (1995) 3244.

2) A. Osa, T. Ikuta, K. Kawade, H. Yamamoto and S. Ichikawa, *J. Phys. Soc. Jpn.* **65** (1996) 928-934.

3) M. Shibata, Y. Kojima, H. Uno, T. Uchino, H. Yamamoto, K. Kawade, A. Taniguchi and Y. Kawase, Proceedings of the Seventh EGS4 Users' Meeting in Japan, *KEK proceedings 98-7* pp.55 (1998).

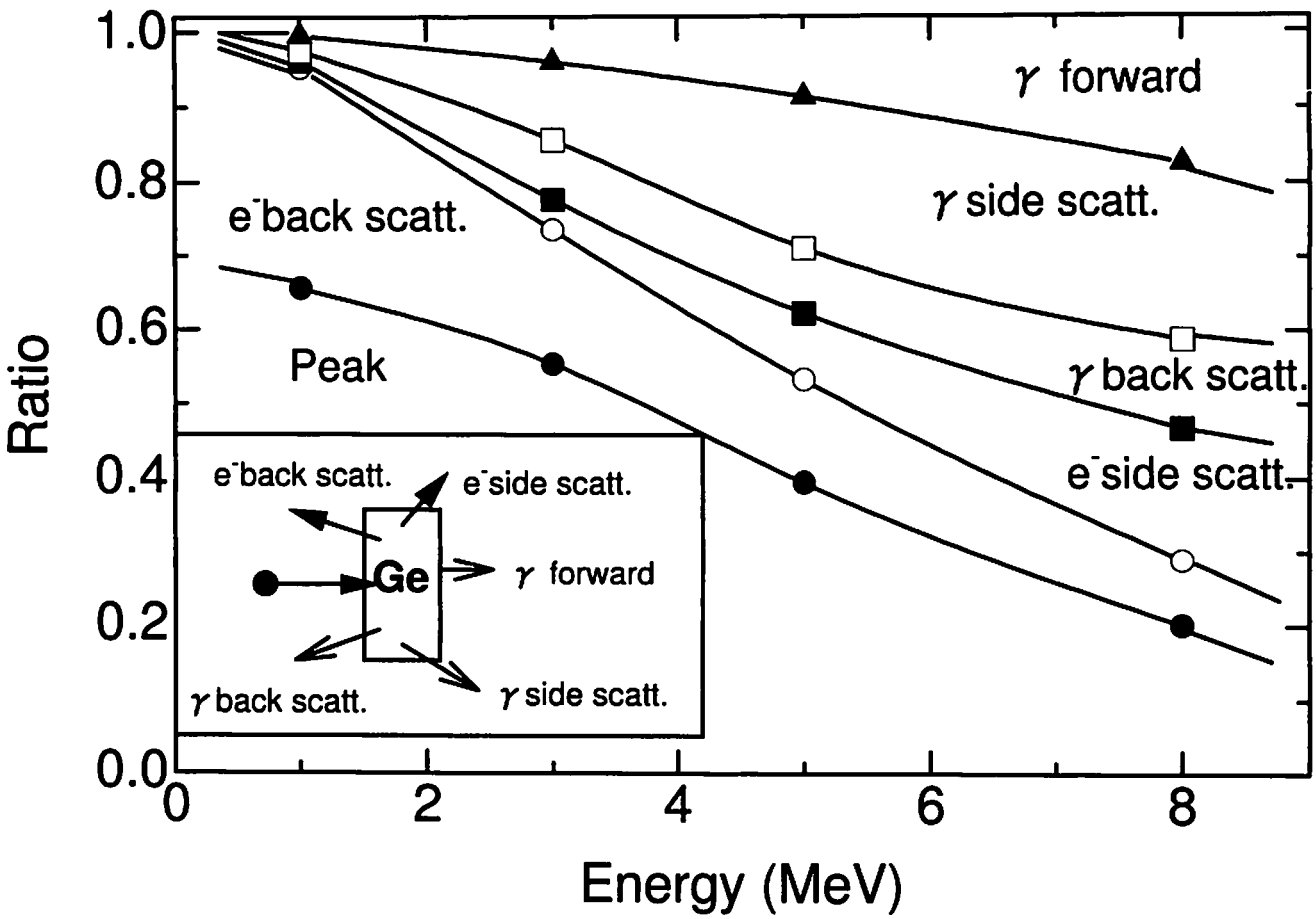

Fig. 1 The energy escape ratios from a 36mm $^{\phi}$ × 13mm^{t} Ge crystal when electrons go into the crystal as shown in an inset. The "Peak" represents the full energy absorption. The other parts represent the escapes of each direction as shown in an inset.

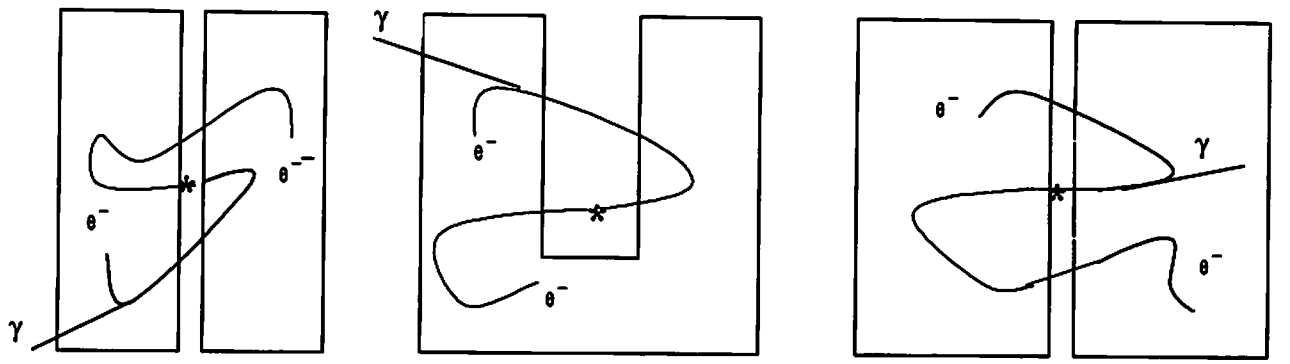

Ge size 36mm$^{\phi}$ × 13mm^{t} Ge size 55.7mm$^{\phi}$ × 60.2mm^{t} BGO size 12cm$^{\phi}$ × 10cm^{t}

well depth 40mm

well diameter 14.5mm

(a) (b) (c)

Fig. 2 Schematic views of new-type β-ray detectors.
(a) a sum-type Ge detector (b) a well-type Ge detector
(c) a sum-type BGO scintillation detector

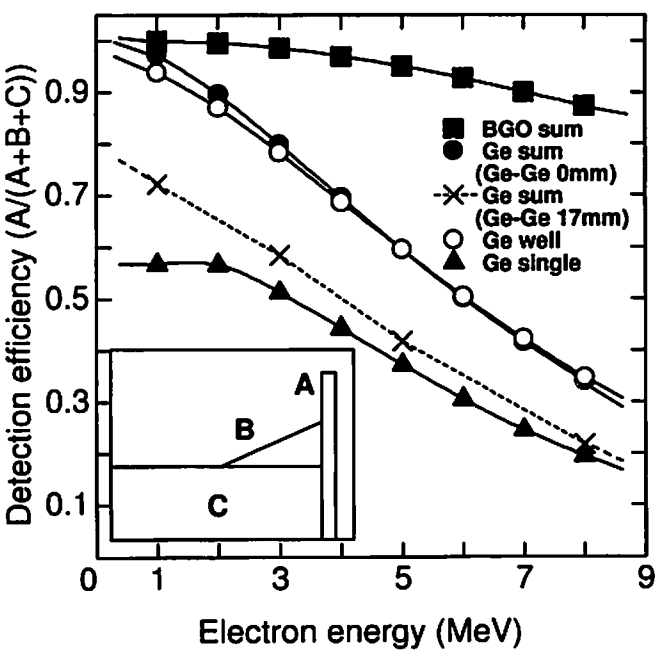

Fig. 3 The energy dependence of the simulated response functions of a sum-type Ge detector(Ge-Ge 0mm, 17mm), a well-type Ge detector, a sum-type BGO scintillator detector anda single Ge detector.

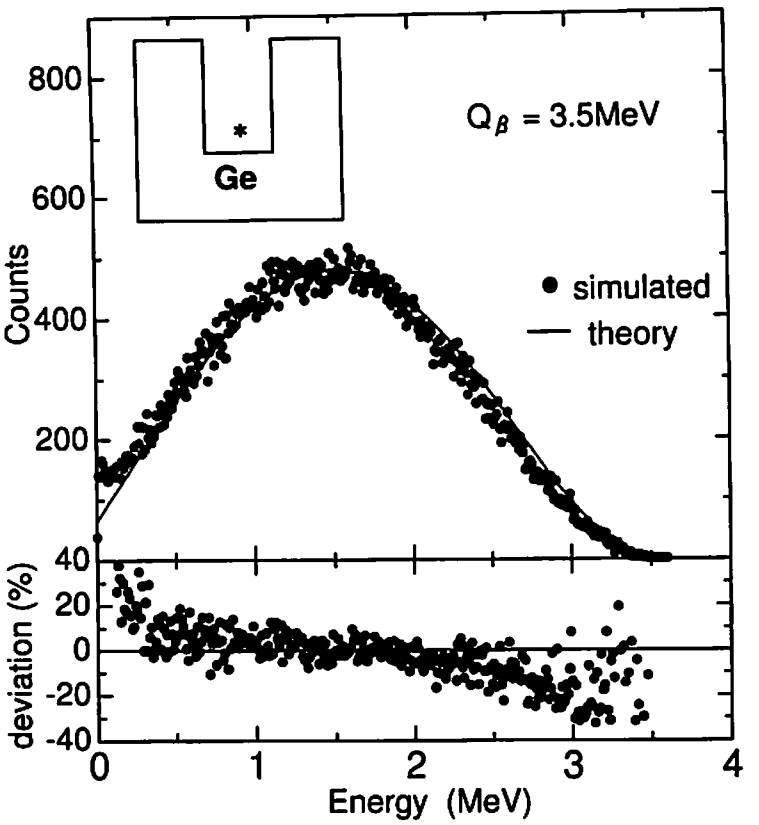

Fig. 4 A simulated β -ray spectrum with a well-type Ge detector. The lower part shows the deviation between the simulated and theoretical β -ray spectrum.

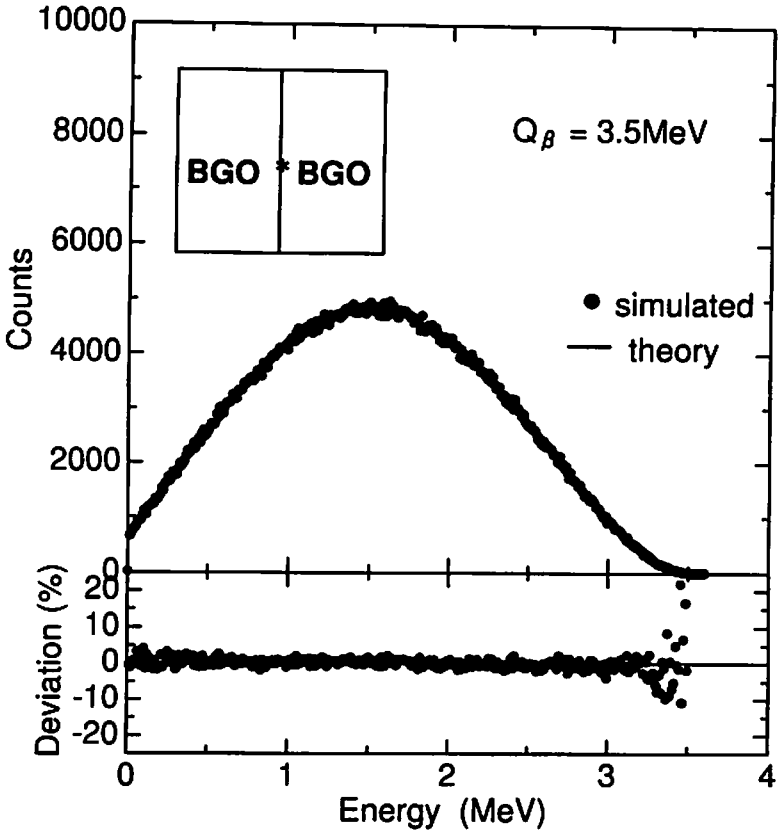

Fig. 5 A simulated β-ray spectrum with a sum-type BGO scintillation detector. The lower part shows the deviation between the simulated and theoretical β-ray spectrum.

RESPONSE OF NaI(Tl) SCINTILLATION DETECTORS FOR GAMMA RAYS

H. Tawara, S. Sasaki, K. Saito[1], E. Shibamura[2] and M. Miyajima[3]

High Energy Accelerator Research Organization
1-1 Oho, Tsukuba, Ibaraki 305-0801, Japan
[1] *The Graduate University for Advanced Studies*
1-1 Oho, Tsukuba, Ibaraki 305-0801, Japan
[2] *Saitama Prefectural University, Junior College*
820 Sannomiya, Koshigaya, Saitama 343-8250, Japan
[3] *Department of Applied Physics, Fukui University*
3-9-1 Bunkyo, Fukui 910-8507, Japan

Abstract

An EGS4 Monte-Carlo calculation for gamma-ray transport in a NaI(Tl) scintillator was performed in order to output the initial spatial distribution of the scintillation yields. The relative scintillation yields for secondary electrons were estimated by taking into account the experimental electron-response curve of the NaI(Tl) scintillator. The energy-response curve and the intrinsic energy resolution corresponding to the full-energy deposition of gamma rays are described and discussed. Using the output from the EGS4 usercode, we will next simulate the scintillation-photon transport in a NaI(Tl) scintillator in order to evaluate the collection efficiency of scintillation photons to the photomultiplier photocathode. The absolute scintillation yield will be determined by comparing the calculated results with experiments.

1 Introduction

A scintillation process has been one of the most useful methods for the detection and spectroscopy of radiations. The mean energy required to produce one scintillation photon, the W_s value [1] is the important physical quantity for understanding the energy pathways of the radiation to luminescence or to estimate the light output of various scintillators properly:

$$W_s = \frac{T}{N_s}, \tag{1}$$

where T is the initial kinetic energy of the radiation and N_s is the mean number of scintillation photons produced in a scintillator by the full-energy deposition of the radiation.

We developed a method to determine the absolute values for N_s of various scintillators. The W_s values of some liquid and solid scintillators have been estimated by using various photomultipliers (PMT) conformable to their scintillation lights[1, 2, 3, 4]. The method consists of two parts:

[1]The W value is defined as the mean energy required to produce one ion pair in matter by ionizing radiations when the initial kinetic energy of the radiation is completely dissipated in the matter. It is well known that the W value has been the basic concept related to an ionization process in radiation dosimetry, radiation spectroscopy and radiation chemistry of gases until now. The W_s value was introduced to expand the definition of the W value to a scintillation process[1].

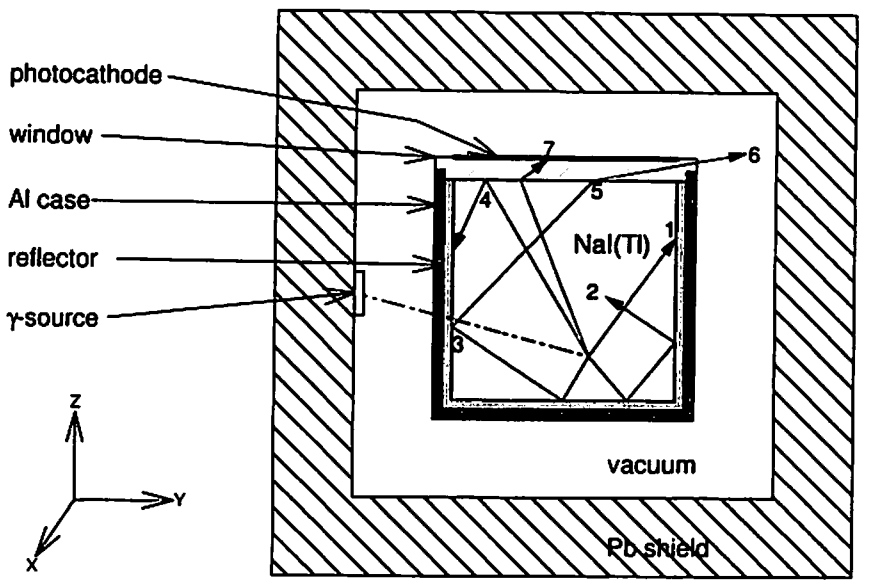

Figure 1: Cross-sectional view of the geometry of the NaI(Tl) scintillation detector used for Monte-Carlo simulations. The broken line represents the path of an incident gamma ray. The solid lines describe the typical flightpaths of scintillation photons emitted at the scintillation point. The following seven processes are treated in the SPC3 code: (1) absorption at the reflector, (2) absorption (attenuation) in the crystal, (3) reflection at the reflector, (4) reflection at the boundary between the window and the crystal, (5) refraction at the boundary between the window and the crystal, (6) escape from the detector, and (7) collection to the photocathode. The Pb shield is added for the present EGS4 calculation, but is not used in the SPC3 calculation.

1. the measurement of $N_{\rm pe}$, the absolute number of photoelectrons from the photocathode of a PMT connected to a scintillator.

2. the Monte-Carlo calculation of scintillation-photon transport in the scintillator for estimating $F_{\rm c}$, the collection efficiency of the scintillation photons produced in the scintillator to the photocathode.

We have developed a computer code for simulating scintillation-photon transport. The current version is named SPC3 (Simulation of photon collection in cylindrical vessel, ver.3) and can treat seven processes in the scintillation detector, which are shown in Fig. 1. The conversion efficiency of a scintillation photon to a photoelectron is known as the quantum efficiency of the photocathode ($F_{\rm qe}$). Thus, $N_{\rm s}$ in eq.(1) can be estimated by

$$N_{\rm s} = \frac{N_{\rm pe}}{F_{\rm c} F_{\rm qe}}. \tag{2}$$

Upon gamma-ray measurements, the full-energy peaks on the gamma-ray spectra commonly represent the energy response and energy resolution of a scintillation detector. Therefore, it is practical and useful to estimate an effective value corresponding to the full-energy deposition of gamma rays as the $W_{\rm s}$ value of the scintillation material of the detector for gamma rays. In this case, it is essentially important to consider that scintillation occurs directly by the energy dissipation of fast secondary electrons, such as Compton recoil electrons, photoelectrons, electron-positron pairs and Auger electrons. As the result of the full-energy deposition of *one* gamma ray, *several* scintillation points are created by these electrons scattered in the scintillator. If one

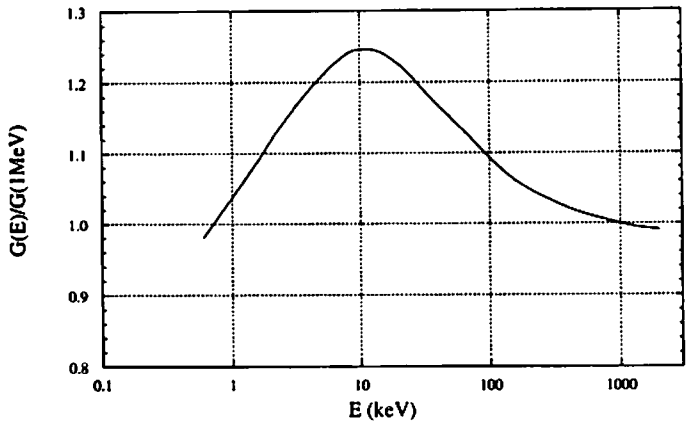

Figure 2: Electron response of NaI(Tl) normalized at 1 MeV.

estimates the total scintillation yield corresponding to the full-energy deposition of the gamma ray, the partial yields at these scintillation points must be estimated with careful consideration of the "electron response" of the scintillator. The electron response is frequently defined as the scintillation yield per unit electron energy. So far, experiments concerning a variety of scintillators have indicated that light outputs for electrons are not proportional to their initial kinetic energy. This nonproportioality also causes a broadening of the full-energy peaks on the gamma-ray spectra, which is sometimes referred to as an "intrinsic energy resolution" for gamma rays[5, 6].

The results of SPC3 calculations indicated that F_c strongly depends on the position of a scintillation point relative to that of a photocathode because of the absorption and escape of scintillation photons, as described in Fig. 1. When determining the W_s value experimentally, we must know the initial spatial distribution of the scintillation yields to calculate an accurate value for F_c by the SPC3 code. The EGS4 code[2] allowed us to simulate gamma-ray interactions in a scintillation detector and to obtain the spatial distribution of the scintillation yield inside its scintillation material corresponding to the full-energy deposition of gamma rays. In this work, we concentrated our efforts to study a NaI(Tl) scintillator as the most typical one. The following sections describe the electron response of the NaI(Tl) scintillator and the details of the present EGS4 calculation. This report also describes and discusses the intrinsic response of the NaI(Tl) scintillator for gamma rays obtained as results of the EGS4 calculation: the energy-response curve and the intrinsic energy resolution for gamma rays, which appear as a natural consequence of the gamma-ray interactions and the nonproportionality of the electron response.

2 Electron response

The electron response of a scintillator is, henceforth, expressed by $G_e(E)$:

$$G_e(E) = N_s(E)/E, \tag{3}$$

where E is the initial kinetic energy of an electron. Figure 2 shows the normalized electron-response curve used for the present calculation, which was experimentally obtained most recently by the Compton coincidence technique[7]. The previous experiments have been indicated that the $G_e(E)$ of NaI(Tl) scintillator has a maximum at around 10 keV, which is 20% to 30% larger than

[2]The EGS4 is a computer code for the Monte-Carlo simulation of the coupled transport of electrons and gamma-ray or X-ray photons with energies above several keV.

that at 1 MeV [7, 8]. The nonproportioality of the light output has been reported for various charged particles as well. This has been explained in terms of the linear energy transfer (LET) of the charged particle[9, 10]. In cases in which the scintillation yields for gamma rays are compared to those for charged particles, the effective LET for the gamma rays should be estimated from the LET distribution of the concerned secondary electrons.

3 EGS4 calculation

New functions were added to the default EGS4 code [11] to simulate the photon[3] transport and generation of secondary electrons in the low-energy region. This modified EGS4 code [12] can treat the following items: (1) the photoelectrons and X-rays in K-shell and L-shell photoelectric absorption [13], (2) K-Auger and L-Auger electrons, (3) Doppler-broadening of Compton-scattered photons [14], and (4) the linear polarization of photons in scattering and the anisotropic scattering of the linearly polarized photons in their azimuthal distribution [15]. The default random-number generator was also replaced by one that is based on a Lagged-Fibonacci method and has a period of 2^{144} [16].

A NaI(Tl) scintillation detector was described by cylinder-slab geometry in the EGS4 usercode, as shown in Fig.1. The geometry consists of a Pb shield used to reduce the background gamma rays, an Al case, a MgO reflector, a NaI crystal containing 0.1% Tl by weight and a SiO_2 window. Either an isotropic point source or a pencil beam was selected as a gamma-ray source according to the experimental setup. The cutoff energy on photon transport for each region was set to 1 keV. Electron transport wasn't simulated to save computation time. For example, the entire kinetic energy of a Compton recoil electron was deposited immediately at its Compton-scattering point. The EGS4 usercode scored the positions and energy of the Compton recoil electrons, photoelectrons, electron-positron pairs and Auger electrons for every incident gamma ray.

When the SPC3 code calculates the effective value for F_c, the initial spatial distribution of the scintillation yield is required as input information. A partial scintillation yield, $n_s(x,y,z)$, was therefore calculated by the EGS4 usercode:

$$n_s(x,y,z) = G_e(E)E(x,y,z), \tag{4}$$

where the scintillation point (x,y,z) was set to the generation point of the secondary electron which acts as a scintillation source.

On the other hand, the intrinsic characteristics of scintillators corresponding to the full-energy deposition of gamma rays can be understood in the following expression of N_s:

$$N_s(T) = \int_0^T P(E,T)G_e(E)EdE, \tag{5}$$

where T is the energy of an incident gamma ray and $P(E,T)$ is the frequency of a secondary electron having energy E produced in the scintillator by the full-energy deposition of the gamma ray. On the basis of the expression of eq.(5), the gamma-ray response can be defined as

$$G_g(T) = N_s(T)/T = \int_0^T [P(E,T)E/T]\, G_e(E)dE. \tag{6}$$

Both $P(E,T)E/T$ and $G_e(E)$ are important factors which characterize the gamma-ray response of the NaI(Tl) scintillator, as discussed in the section 4.

[3]The term "photon" involves gamma-ray and X-ray photons which are able to generate fast secondary electrons as scintillation sources. A photon, which is generated in the luminescence process and is detected by a photomultiplier, is always called a "scintillation photon" in this paper, whose transport is treated only in the SPC3 calculation.

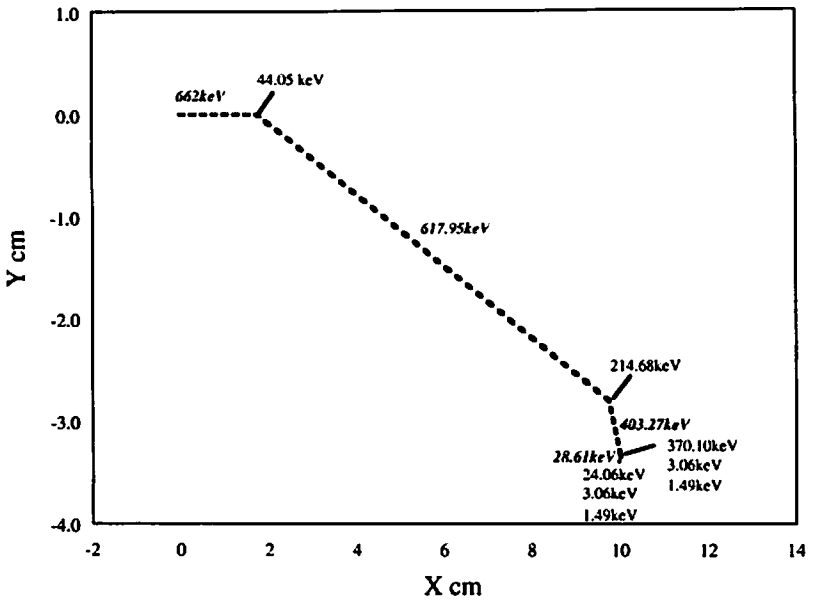

Figure 3: EGS4 simulation for one 662-keV gamma-ray incident to a NaI(Tl) crystal. The solid and broken lines show the trajectories of electrons and photons, respectively. They are projected onto the X-Y plane of the geometry shown in Fig. 1. The upright and italic figures show the energy of electrons and photons, respectively. The path lengths of photons are real, but those of electrons are scaled up arbitrarily.

Detailed calculations were first performed for 662-keV gamma rays emitted from ^{137}Cs to understand the characteristics of the gamma-ray response and its NaI(Tl)-crystal size dependence. A number of calculations were then performed concerning an infinite-volume crystal to obtain the energy dependence of the gamma-ray response and the intrinsic energy resolution.

4 Results and Discussions

Figure 3 shows the typical spatial distribution of the secondary electrons simulated with the EGS4 code, where one 662-keV gamma ray completely loses its energy inside a NaI(Tl) crystal. The 44.05-keV and 214.68-keV recoil electrons are produced through Compton-scattering. The Compton-scattered photon of 403.27 keV is absorbed in the K-shell of an iodine atom and produces a 370.10-keV photoelectron, a 3.06-keV Auger electron and a 28.61-keV $K_{\alpha 1}$-X ray. The $K_{\alpha 1}$-X ray is also absorbed in the K-shell of another iodine atom and produces another 3.06-keV Auger electron. The generation of each Auger electron creates two holes in the M-shell of the iodine atom. Instead of following further cascade processes in the iodine atom, the present EGS4 code outputs an excess energy of 1.49 keV (twice the M-shell binding energy) as energy deposition at the photoelectric absorption point.

$P(E,T)E/T$ in eq.(6) indicates the relative importance of a secondary electron with energy E to the full-energy peak of the gamma-ray spectrum. Figures 4-(a) and 4-(b) show $P(E,T)E/T$ as a function of E, of the infinite-volume crystal and of the 1-inch one, respectively. 662-keV gamma rays almost interact with iodine atoms in the crystal: 85% cause Compton scattering and the rest undergo photoelectric absorption. The kinetic energy of recoil electrons and scattered photons in the Compton scattering distribute from zero to 467.5 keV and from 194.5 keV to 662 keV, respectively. The photoelectric absorption of 662-keV gamma rays occurs 83.5% on the K-shell. After the emission of a photoelectron, a hole in the K-shell produces 88% X-rays and 12% Auger

electrons. In the case of infinite volume, the Compton recoil electrons[4] are given much weight in the scintillation yield, as shown in Fig. 4-(a). In a smaller size crystal, the relative importance moves from Compton recoil electrons to photoelectrons which are mainly K-shell photoelectrons produced directly by 662-keV incident gamma rays, as shown in Fig. 4-(b). The $G_e(E)$ values for these K-shell photoelectrons are smaller than those for the Compton-recoil electrons. The scintillation yield corresponding to the full-energy deposition, therefore, decreases with decreasing the crystal size. The ratio $G_g(662\text{keV})/G_e(1\text{MeV})$ was 1.046 and 1.038 in the infinite-volume crystal and in

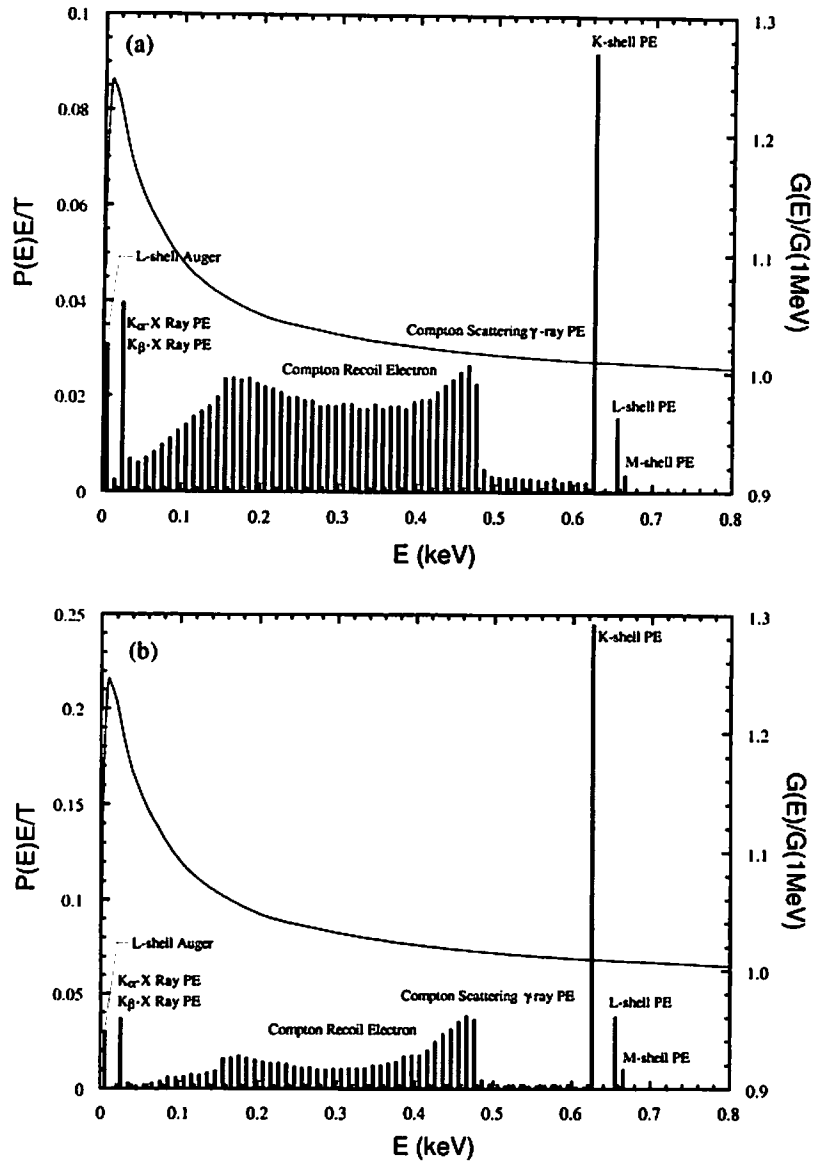

Figure 4: Relative importance of secondary electrons to the scintillation yield of NaI(Tl) scintillator corresponding to the full-energy deposition of 662-keV gamma rays: (a) an infinite-volume and (b) 1 inch diameter × 1 inch height. The bars show $P(E,T)E/T$. The solid lines show $G_e(E)/G_e(1\text{MeV})$, which is the same curve as that in Fig. 2. The "PE"s stand for photoelectrons.

[4]Actually there also exists the contribution of photoelectrons which are produced by the photoelectric absorption of Compton-scattered photons, whose distribution overlaps on that of the Compton recoil electrons in figures 4-(a) and 4-(b).

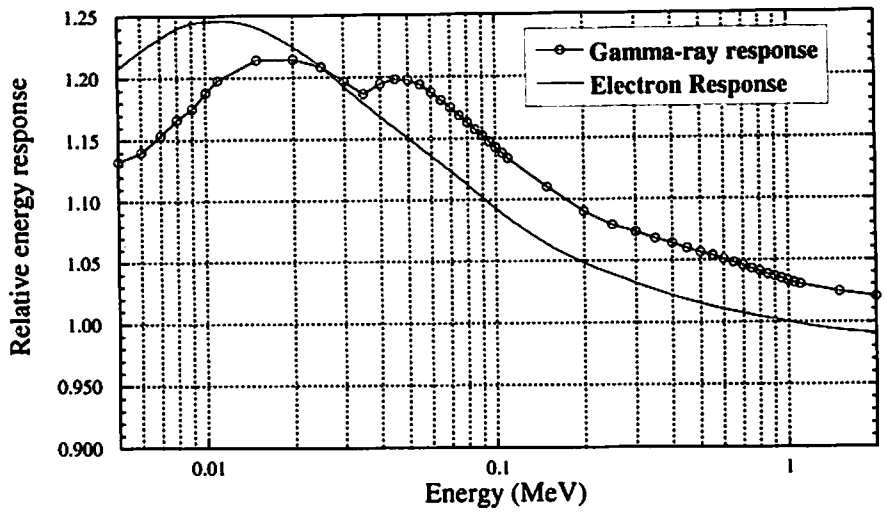

Figure 5: Relative gamma-ray response curve obtained in the present work. Circles indicate the calculated data points.

the 1-inch one, respectively.

The ratio $G_g(T)/G_e(1\text{MeV})$ of the infinite volume crystal was calculated in order to obtain the relative gamma-ray response as a function of the gamma-ray energy. Figure 5 shows a comparison between the electron-response curve and the gamma-ray response curve, where both curves are relative to the value for $G_e(1\text{MeV})$. The gamma-ray response is 4% to 5% larger than the electron response in the 50 keV to 1MeV energy range, and a depression appear in the vicinity of the K-edge of iodine (33.7 keV).

The gamma-ray spectra were calculated in order to estimate the intrinsic energy resolution of gamma rays. Figures 6-(a) and 6-(b) are the spectra calculated by the present EGS4 code. When calculated disregarding the nonproportioality of electron response, the full-energy peak becomes monochromatic, as shown in Fig. 6-(a). Figure 6-(b) shows the spectrum calculated with the electron response of the NaI(Tl) scintillator in Fig 2. It clearly indicates that the nonproportioality of the electron response broadens the full-energy peak. The fine structure of the peak is related to the number of secondary electrons involved in the full-energy deposition of one gamma ray. The broadening of the full-energy peak for 662-keV gamma rays was calculated to be about 1.9% in a standard deviation in a 2-inch crystal: this intrinsic resolution is equivalent to 4.5% in FWHM.

Figure 7 shows the intrinsic energy resolution in FWHM as a function of the gamma-ray energy, which was calculated for an infinite volume. In the 50 keV to 1 MeV energy range, the intrinsic energy resolution was calculated to be about 4% to 5.5%. In the vicinity of the K-edge of iodine, the calculated resolution took a minimum value of about 1% in FWHM.

5 Summary and Future Plane

In order to estimate the absolute W_s value corresponding to the full-energy deposition of gamma rays, the EGS4 code was improved and its usercode was produced. This usercode can output the initial spatial distribution of the scintillation yield by taking into account the position and energy of secondary electrons, and the electron-response curve.

The response of the NaI(Tl) scintillator was investigated using the present EGS4 usercode. In the energy range of several hundred keV, the scintillation yields for the full-energy deposition of

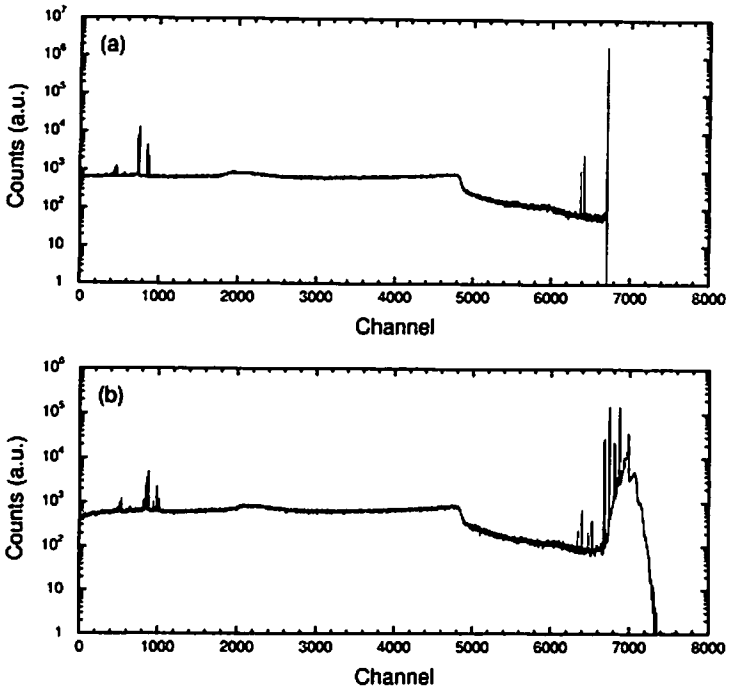

Figure 6: Spectra calculated for the 662-keV gamma-ray incidence: (a) energy-deposition spectrum and (b) scintillation yield spectrum calculated by taking into account the energy distribution of the secondary electrons and the electron response. The NaI(Tl)-crystal size is 2 inch diameter × 2 inch height.

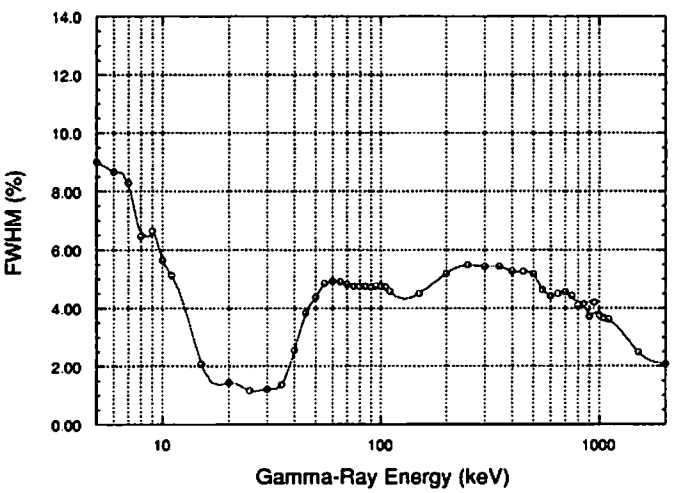

Figure 7: Intrinsic energy resolution calculated for an infinite volume. The white circles indicate the calculated points. The solid line is added just as a guide for seeing.

gamma rays were found to be about 5% higher than those for electrons having the same energy. The nonproportioality of the electron-response curve caused an intrinsic energy resolution for gamma rays: it was about 5% in FWHM in the gamma-ray energy region of several hundred keV.

In the next step, we will simulate the scintillation-photon transport in a NaI(Tl) detector to evaluate the collection efficiency of scintillation photons to a photocathode precisely by coupling the EGS4 calculation to the SPC3 calculation. The absolute W_s value corresponding to the full-energy deposition of gamma rays will be determined by comparing the calculated results with experiments.

References

1) M. Miyajima, S. Sasaki, H. Tawara, and E. Shibamura, *IEEE Trans. Nucl. Sci.* **39**, 536 (1992).

2) M. Miyajima, S. Sasaki and E. Shibamura, *Nucl. Instrum. Meth.* **224**, 331 (1984).

3) M. Miyajima, S. Sasaki and H. Tawara, *IEEE Trans. Nucl. Sci.* **40**, 417 (1993).

4) E. Shibamura, S. Sasaki, H. Tawara and M. Miyajima, *KEK Proceedings* **99-8**, 175 (1999).

5) B. D. Rooney and J. D. Valentine, *IEEE Trans. Nucl. Sci.* **44**, 509 (1998).

6) J. D. Valentine, B. D. Rooney and J. Li, *IEEE Trans. Nucl. Sci.* **45**, 512 (1998).

7) B. D. Rooney and J. D. Valentine, *IEEE Trans. Nucl. Sci.* **43**, 1271 (1996).

8) A. J. R. Prescott and G. H. Narayan, *Nucl. Instrum. Meth.* **75**, 51 (1969).

9) R. B. Murray and A. Meyer, *Phys. Rev.* **122**, 815 (1961).

10) T. Doke, E. Shibamura and S. Kubota, *J. Phys. Soc. Jpn.* **68**, 2433 (1999).

11) W. R. Nelson, H. Hirayama and D. W. O. Rogers, *SLAC-265* (Stanford University, Stanford 1985).

12) Y. Namito, S. Ban and H. Hirayama, *Radiat. Phys. and Chem.* **53**, 283 (1998).

13) H. Hirayama, Y. Namito and S. Ban, *KEK Internal* **96-10** (1996).

14) Y. Namito, S. Ban and H. Hirayama, *Nucl. Instrum. Meth.* **A349**, 489 (1994).

15) Y. Namito, S. Ban and H. Hirayama, *Nucl. Instrum. Meth.* **A332**, 277 (1993).

16) G. Marsaglia, A. Zaman and W. W. Tsang, *FSU-SCRI-87-50* (1987).

RESPONSE FUNCTION AND ITS APPLICATION TO A SEMICONDUCTOR RADIATION DETECTOR WITH SMALL MOBILITY AND LIFETIME

M. HIRASAWA and M. YAMAMOTO

Division of Radiation Research National Institute of Radiological Sciences
9-1 Anagawa-4, Inage-ku, Chiba 263-8555 Japan

Abstract

A radiation detector using a semiconductor like CdTe can measure radiation rays at room temperature because its band gap is comparably big. However the energy and time resolutions become coarse because mobility and lifetime of electrons and holes drop at room temperature. These important values also fluctuate depending on the completeness of the crystal. A method is proposed to acquire information about the values from the detector response function.

1 Experiment

Fig.1 shows the measured response function curve of a planar type CdTe detector with 1 mm thickness and 80 V applied voltage for the gamma rays from ^{22}Na. The photoelectric absorption peaks for 511 keV and 1.275 MeV gamma rays are seen around the center and right terminal, respectively. Fig.2 shows an enlarged function curve around the 511 keV peak. It is seen that the 511 keV peak has a larger tail on the lower energy side. Fig.3 shows a further enlarged function curve of the area enclosed by the rectangle in Fig.2. It is seen that there is a small difference in elevation at channel number 1076. It is possible to say that the 511 keV peak has its a right edge at channel number 1449 and its left edge at channel number 1076. The ratio of these channel numbers is approximately 1.3.

2 Simulation

The radiation detector system shown in Fig.4 is assumed, where the gray part is a planar type semiconductor detector with thickness of d and x means depth of the photoelectric reaction point. The pulse height of a detection signal VRh is written in the form

,

where λ_e and λ_h express the mean free paths of electrons and holes in the semiconductor detector, respectively. The part enclosed by square brackets is called Hecht's coefficient1).

The simulated response function curve of the planar type CdTe detector for gamma rays from ^{22}Na (same conditions as in Fig.1) is shown in Fg.5. The Monte Carlo simulation code EGS4, using Hecht's coefficient as the weight function for the deposited energy in the code, is used. The values of λ_e and λ_h are calculated using the published values[2] of the mobility $\times$ lifetime for the CdTe crystal used in the experiment. Fig.6 shows the enlarged function curve around the 511 keV

photoelectric absorption peak. It is also seen that the 511keV peak has a tail on the lower energy side and it has its right edge at 500 keV and its left edge at 361 keV. The ratio of these energies is approximately 1.4.

3 Discussion and Conclusion

The low energy side tail in photoelectric absorption peaks is caused by the photoelectric reaction depth dependence of the pulse height of the detection signal VRh described in the above formula. Using the formula, the right edge to left edge ratio in photoelectric absorption peaks is written as

.

Therefore, measurement of the edge ratio leads to acquisition of information on λ_e and λ_h which describe mobility and lifetime of electrons and holes, respectively. It is proved by the close agreement with the edge ratio in the simulation to the one in the experiment that accurate measurement of the edge ratio is possible. If statistical fluctuation of the numbers of electrons and holes is considered in the simulation, the edge ratio will become closer to the experimental one.

Table 1 shows operating values and the edge ratios of the planar type radiation detectors using various semiconductors. In order to acquire information on mobility and lifetime, it is necessary that the values of mobility and lifetime be comparatively small.

References

1) K. Hecht, "Zum Mechanismus des lichtelektrischen Primarstromes in isolierenden Kristallen", *Z. Phys.*, **Vol.77**, pp.235-245, 1932.

2) R. Ohno, M. Funaki and T. Ozaki, "Development of the High Quality CdTe Single Crystals for Radiation Detectors", *Ionizing Radiation*, **Vol.22**, pp.9-18, 1996.

Table 1: Edge ratio of planar type semiconductor radiation detector

Material	Operating Temp. (K)	Band gap (eV)	Mob ility Electron (cm^2/ V sec)	Hole	Life time Electron (μ sec)	Hole	Edge ratio Depth : 0.1cm E : 0.8kV/cm
Si	77	1.16	21000	11000	>1000	1000	1.0
Ge	77	0.74	36000	42000	>1000	2000	1.0
CdTe	300	1.47	1100	100	3	2	1.3
CZT	300	2	1100	80	1	0.3	5.0
HgI_2	300	2.13	100	4	1	10	1.9
GaAs	300	1.4	8600	400	0.01	0.01	16.5
Diamond	300	5.4	2000	1600	0.01	0.01	1.2

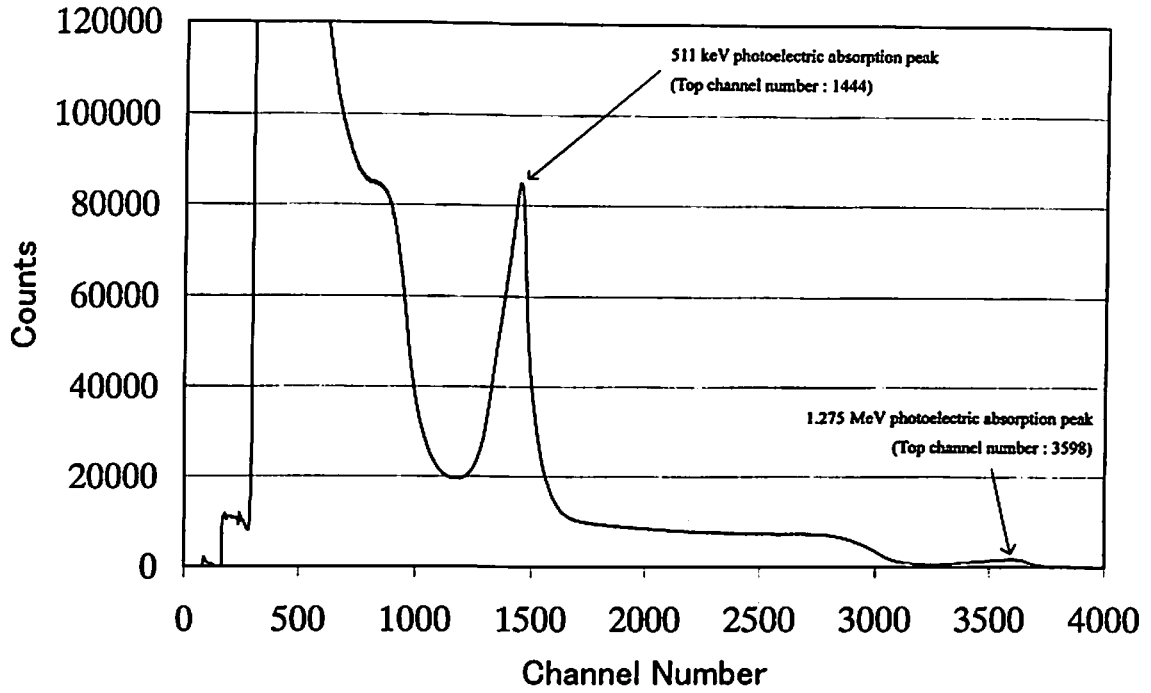

Fig.1: Measured response function of planar type CdTe detector for ^{22}Na

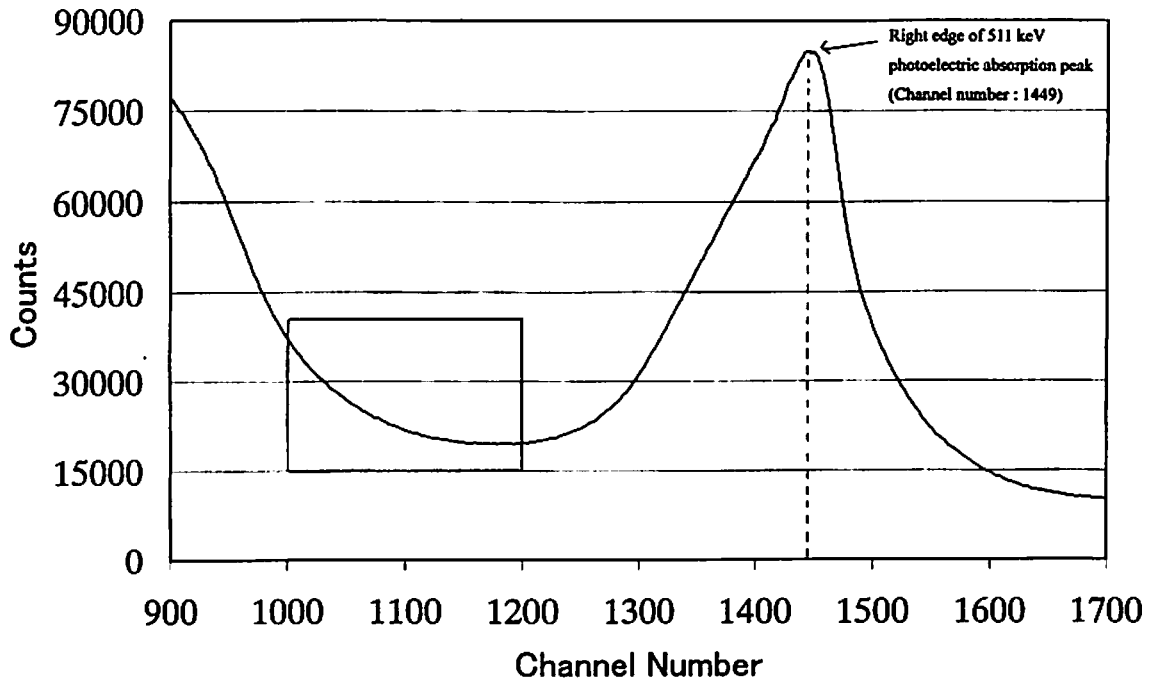

Fig.2: Enlarged function curve around 511 keV peak of Fig.1

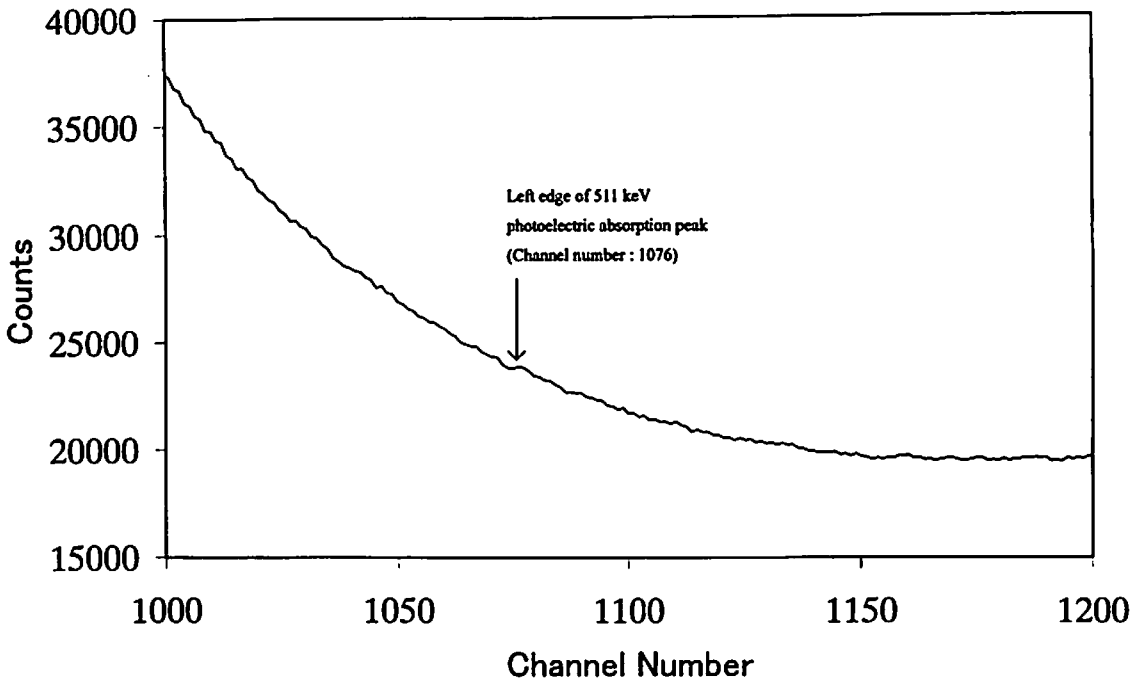

Fig.3: Further enlarged function curve of enclosed area in Fig.2

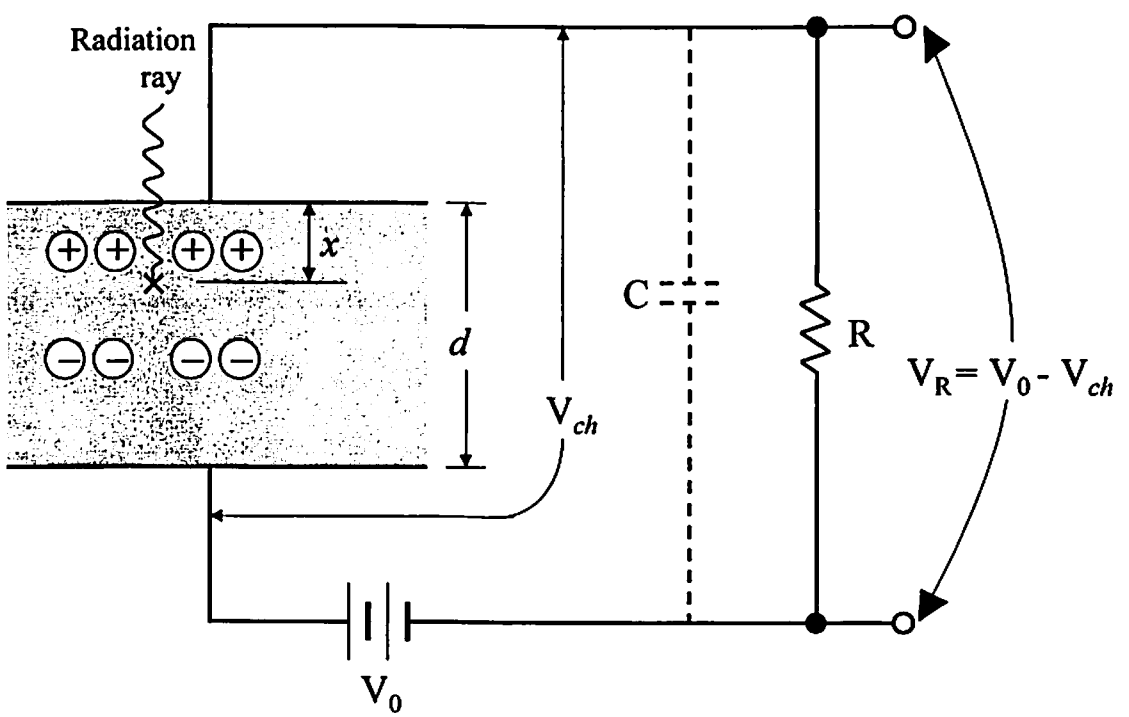

Fig.4: Planar type semiconductor radiation detector system

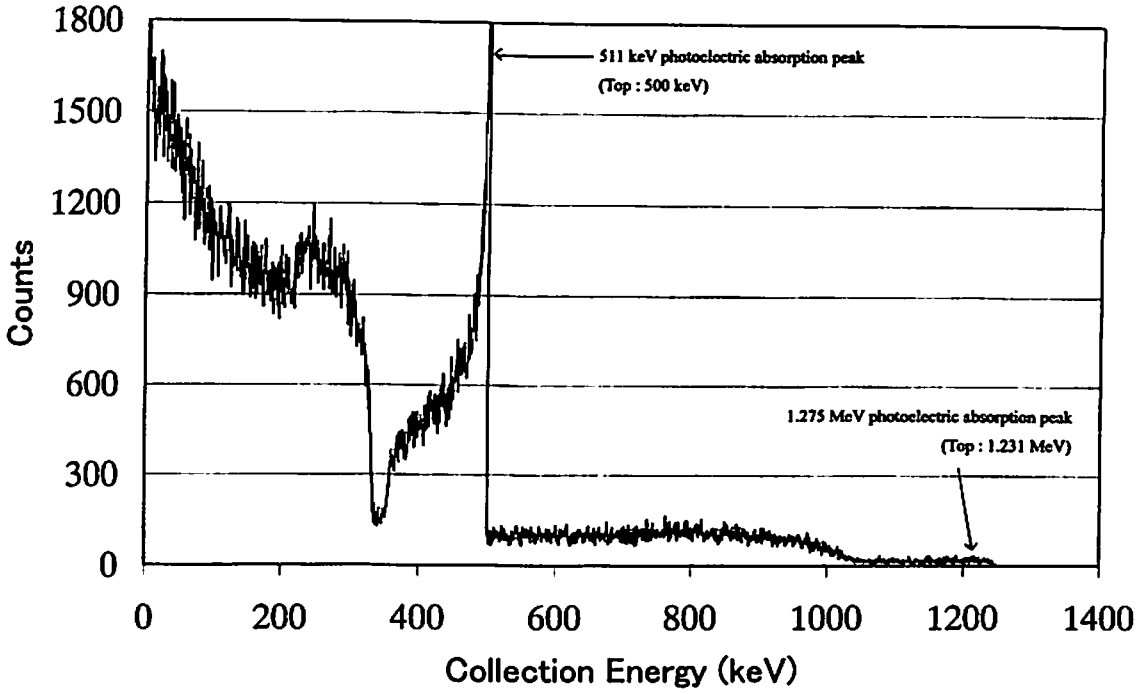

Fig.5: Simulated response function of planar type CdTe detector for ^{22}Na

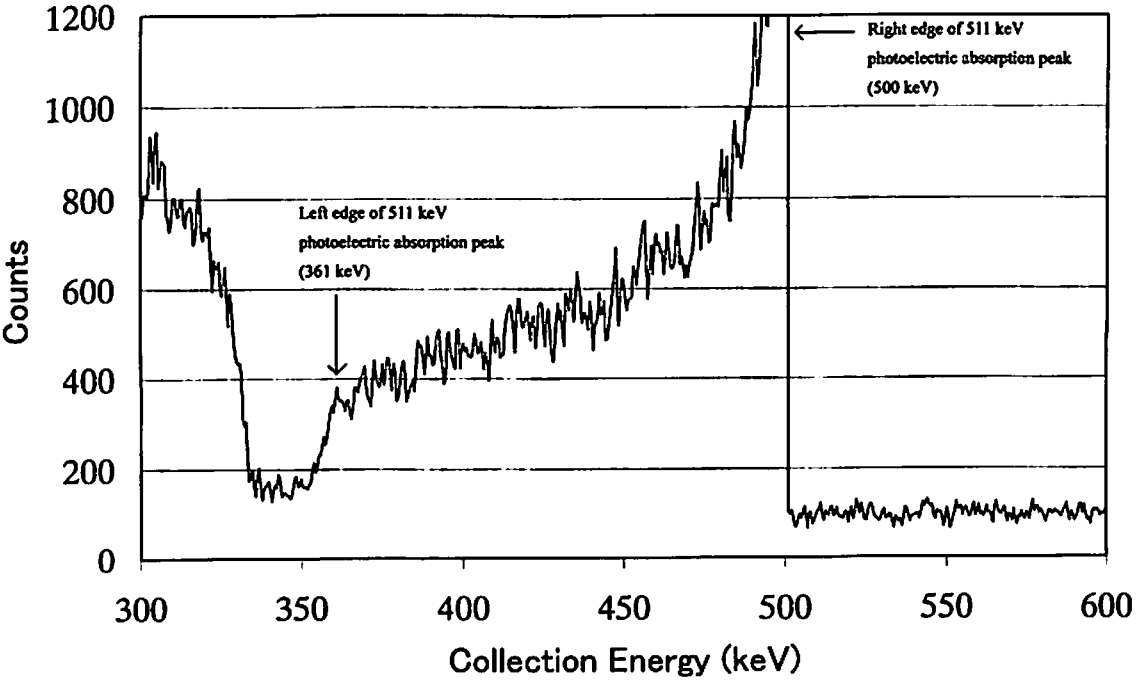

Fig.6: Enlarged function curve around 511 keV peak of Fig.5

GAMMA SENSITIVITY OF THIN GAP CHAMBER

S. TSUNO, B. YE and T. KOBAYASHI

International Center for Elementary Particle Physics
University of Tokyo
Tokyo, 113, JAPAN

Abstract

The Large Hadron Collider(LHC) at the European Laboratory for Particle Physics (CERN) is expected to operate at lower luminosity ($10^{33}cm^{-2}s^{-1}$) for the first three years and at the full luminosity of $10^{34}cm^{-2}s^{-1}$ by year 2008 and on. Thin Gap Chamber(TGC) must operate under this high luminosity. Therefore there will be enormous background whose effect have to be estimated. The main particles in the background radiation are neutrons and photons. In this report, the sensitivity of TGC for gammas with energy from 20 keV to 1.8 MeV have been measured using radioactive sources. The measured sensitivity was compared with results from calculations of the Monte Carlo simulation code called EGS4(Electron Gamma Shower). The average sensitivity of the TGC for gammas is about 1%.

1 Introduction

There are three major sources of radiation at the LHC: particle production at the interaction point, local beam losses, and beam-gas interactions. The total beam loss around the ring should not exceed 10^7 protons s^{-1}, which is relatively small when compared with the p-p collision rate of $10^9 s^{-1}$ per collision point. Beam-gas interactions are estimated to be $10^2 m^{-1} s^{-1}$ in the interaction area. Therefore the dominant radiation source will be from particles produced in proton-proton collisions at the interaction point. The enormous rate of these collisions will cause radiation damage, particle miss-ID, fake tracking, fake trigger and so forth.

The background particles are neutrons, photons, neutral pions (π^0) and other charged particles(p, $\mu^{\pm}, \pi^{\pm}$) which are generated from the interaction of hadrons produced in pp collisions with the shielding at large $|\eta|$ values, the very forward detectors of ATLAS and the machine elements, such as beam pipes, collimators, pumps and so forth. The main particles generated as the result of these interactions are neutrons that will diffuse into the hall, and producing secondary particles when interacting with matter. In particular, thermal neutrons are absorbed by nuclei with the emission of photons. The kinetic energy of these photons is in the range of 10 - 10^4 keV(Ref.[1]). On the other hand, fast neutrons produce hadrons when interacting with the material of the apparatus. A non negligible fraction of these particles are charged particles such as pions, protons and muons. These background particles will result high detector counting rates in the detector.

Total backgrounds in the first muon station, and the maps of neutron and gamma fluence in the ATLAS experimental hall is shown in Ref.[2]. The estimation of the fake level-1 muon trigger rate is presented in Ref.[3].

The Muon System is particularly exposed to this background since the spectrometer is based on an open system, and it may result a radiation damage and fake triggers for TGCs. Therefore,

it is important to study these background particles and to estimate the effect of the chamber aging as well as the fake trigger.

In this report, we have studied the sensitivity of Thin Gap Chamber (TGC) on gammas with energy from 20 keV to 1.8 MeV. The measured sensitivity is compared with the results of calculations of the Monte Carlo simulation using EGS4(Electron Gamma Shower) code (Ref.[4]).

2 Detection Process of Gamma for TGC

The structure of a TGC is the same with that of a MWPC, except that the anode-to-anode, i.e. wire-to-wire, distance is larger than the cathode-to-anode distance. The structure consists of 50 μm radius wires spaced every 1.8 mm. The anode plane is sandwiched between two graphite cathode planes, at a distance of 1.4 mm. The cathode plane consists of a 1.6 mm G-10 plate on which the graphite is deposited. The outside of a G-10 is clothed a copper foil of 18 μm to provide the ground. Fig.1 shows the structure of the TGC.

The almost any gammas in the TGC can transmit without any interactions. But it will interact with some small probability corresponding to each energy. While the main process is the photo-electron effect in the low energy, it is the compton scattering in the high energy nearly 1 MeV. The secondary electron generated by these interactions can reach the sensitive region(gas region) to pass through the TGC wall as repeating the collisions with the wall materials. The TGC have almost 100% efficiency for this secondary electron which reached the sensitive region. But if it dosen't have much energy, it cannot reach the sensitive region. In this case, it will not be detected. Then, when we study the detection process of gammas for TGC, we must understand the interaction process of gammas corresponding to each energy and the behavior of the low energy electron in the TGC wall. And we cannot also ignore the direct interaction of gammas with the gas molecule in the very low energy. The interaction proess of gammas for TGC is imitatively presented in Fig.1.

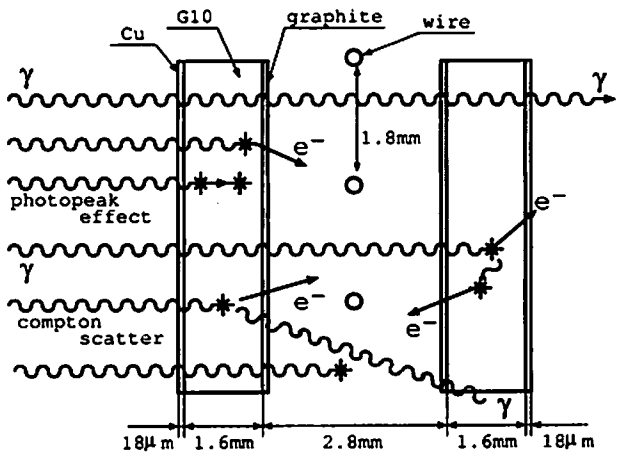

Figure 1: TGC structure and various interaction processes of gammas

3 Experimental Setup

The TGC sensitivity for gammas of different energies was measured by irradiating the detector with collimated gamma rays from a radioactive source. The measurement must be performed with the self-trigger mode since gammas cannot give a signal coincided with other trigger detectors such as TGC and Scintirator. The experimental setup is shown in Fig.2. The trigger signals are given by the OR'ed signals from five wires within the range of irradiation. The arrival time and the counting

were measured using a CAMAC TDC with the gate width set to 186 nsec which is wide enough to cover the drift time (25nsec) of the electrons but not too wide to avoid the double counting. The measurement time was measured using a CAMAC SCALER and total charge was measured using a CAMAC ADC.

A lead block with a small hole placed in front of the radioactive sources made the irradiated area to be about 1.5 cm^2. The signals from TGC were amplified and fed into the discriminator. The digital signals were divided into two signals. One of the signals were fed into the FAN IN/FAN OUT module which output OR signals to combine the input signals, and this output signal was distributed to other CAMAC modules as the trigger signal. The other one of the signals were delayed and put into each channel of the TDC module.

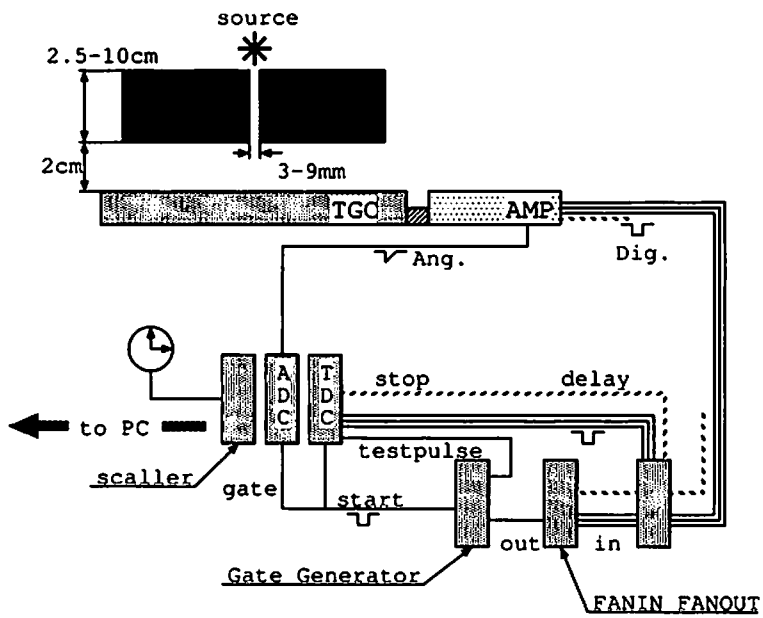

Figure 2: The experimental setup for irradiation of gammas

The source intensity was measured using a NaI(Tl) detector. A calibration was performed by camparing the experimental data with the simulation data using the EGS4. The structure of the collimator for each source with various energies was also determined using the simulation. Various energies and the structure of the collimater for each source are listed in Table1. Since the ^{109}Cd source had very low radio-activity, we did not use a collimator. The ^{88}Y source had rather high gamma energy, we could not properly collimate the gammas. According to the simulation, we needed a collimator of 20 cm in thickness enough to collimate the gammas emitted from ^{88}Y source. We used the collimators which thickness were 2.5, 5.0, 7.5 cm respectively to increase gamma flux on TGC, and we estimated the flux on TGC using the simulation.

The gamma sensitivity of the TGC was calculated as follows,

$$\epsilon_{TGC} = \frac{S_{TGC} - B_{TGC}}{N_{NaI}}$$

where S_{TGC} and B_{TGC} is the count rate of the TGC with and without a radioactive source, N_{NaI} is the total count rate of the gamma radiation with various energies collimated by the lead, measured by NaI(Tl) detector.

In order to confirm the result, we did a measurement of γ - γ coincidence method using a ^{22}Na source looking at pair annihilation and the 1275 keV gamma. Details are in Section 5.

	^{241}Am	^{22}Na	^{137}Cs	^{60}Co	^{133}Ba	(^{109}Cd)	(^{88}Y)
Energy(keV) (branch)	21.0(0.05) 59.5(0.36) 17.6(0.20) 13.9(0.13)	511(0.9) 1275(1.0)	662(0.85) 32.2(0.04) 31.8(0.02) 36.4(0.01)	1173(1.0) 1333(1.0)	81.0(0.34) 356.0(0.62) 302.9(0.18) 383.8(0.09)	22.2(0.55) 22.0(0.29) 24.9(0.14) 25.6(0.03)	898(0.93) 1836(0.99)
Radius(mm)	2.5	2.5	2.5	2.5	2.5	direct	2.5
Length(cm)	2.5	5.0	7.5	12.5	2.5	direct	2.5, 5.0, 7.5
Assignment Energy(keV)	20(0.61) 60(0.39)	511(0.48) 1275(0.52)	662	1253	81(0.28) 356(0.72)	22.2	898(0.48) 1836(0.52)

Table 1: The various energies of the sources and the structure of the collimater for each source

4 Simulation of Sensitivity

For better understanding of the role of different processes causing photon detection in the TGC, the EGS4 simulation was performed assuming a simple structure of the TGC which doesn't contain carborns and wires, presented in Fig.3.

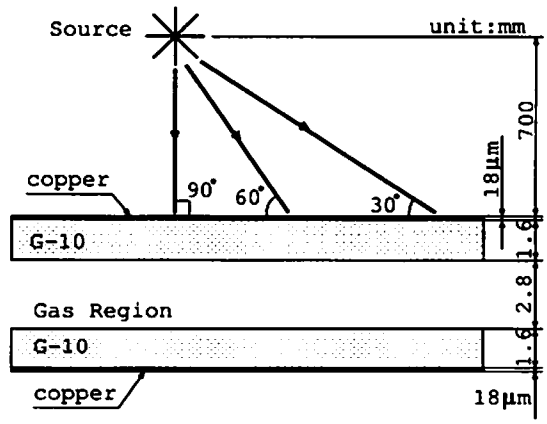

Figure 3: The structure of the TGC used in the simulation

The calculation method of the sensitivity is to count the electrons reached the sensitive region. The sensivity is defined as the ratio, the counts(N_s) of the secondary electron which reached the sensitive region per the counts(N_t) of the gamma which entered in the TGC, in brief N_s/N_t. The cut-off energy is 100eV in which the simulator stops to purchase gammas or electrons. We assume any electrons which reached the sensitive region with more than the cut-off energy are detectable as the signal. The irradiaton angles from the point source are 30, 60, 90 degree on the surface of the TGC. The simulation is performed in the range from 10 keV to 30 MeV of a gamma energy. The interaction probability and the mean free path of an electron and a photon on G-10 is presented in Fig.4, and the angle dependence of the sensitivity for incident gammas is presented in Fig.5.

The interaction probability on G-10 is mainly ruled by Compton scatter, except that Photopeak effect is dominance in low energy under 100 keV (see Fig.4). The mean free path of an electron on G-10 increases untill about 1 MeV and roughly settles the constant value after that. On the other hand, the sensitivity of TGC for gammas depends not only on the energy of gammas but on the incident angle relative to the interaction length on G-10, i.e. as the thickness of G-10 is large, the sensitivity also increases(Fig.5). The sensitivity increases twice, provided that the length of the interaction region become twice. The sensitivity has the peak near 3 MeV. In low energy, almost secondary electrons cannot pass through TGC wall because of the small mean free path

of electron although many electrons are generated in G-10 by Photopeak effect. In low energy, the sensitivity depends on the energy and the position when the secondary electron is generated. In high energy, the sensitivity does not depend on the energy and the position of the secondary electron but depends on the number of secondary electrons, i.e. the interaction probability on G-10, because of the almost constant value of the mean free path of an electron. Then in high energy more than 3 MeV, the sensitivity will be predicted to decrease proportionaly to $exp^{-\mu x}$. We have not found the direct interaction of gammas with the gas molecule.

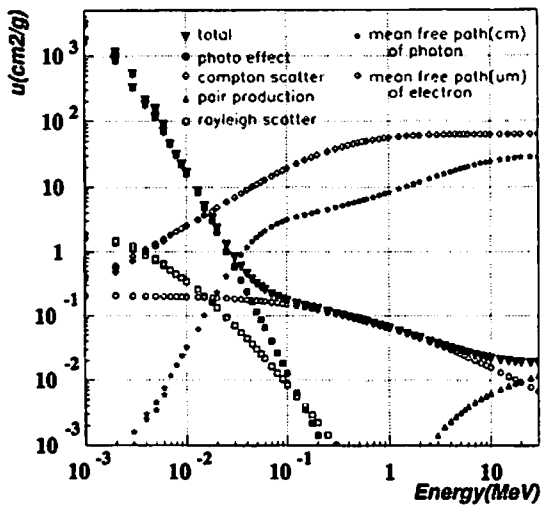

Figure 4: The interaction probability on G-10

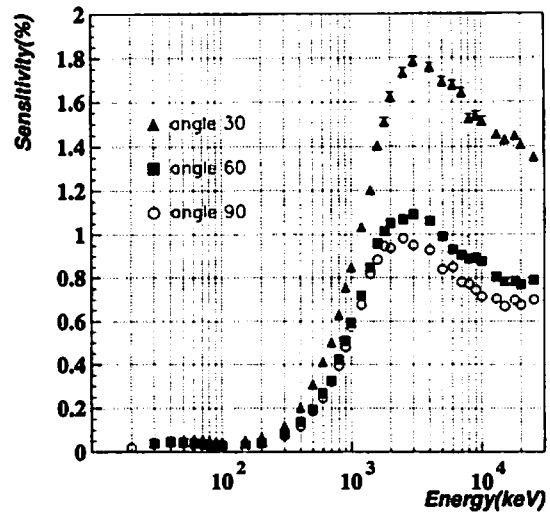

Figure 5: the angle dependence of the sensitivity for incident gammas

5 Results

The measurement was performed by using the 7 radioactive sources. Principal characteristics of these sources are presented in Table1. For this measurement any sources do not have pure monoenergetic photons. These sources have some different energy photons, and in addition some electrons depending on the sources. Since ^{137}Cs and ^{60}Co have the 514 keV and 314 keV electrons respectively, they are screened by 1mm aluminium filters placed between the TGC and the radioactive source. ^{109}Cd, ^{137}Cs, and ^{60}Co are regarded as almost monoenergetic photons since they have the gamma having the large branching ratio or have the mostly closed energies. The sensitivity for each energy of ^{241}Am, ^{133}Ba, ^{22}Na and ^{88}Y are estimated by using the simulation data since they have almost two gammas having the large branching ratio. The energy which we defined for thier sources are presented in Table1. But we used the ^{109}Cd and ^{88}Y sources as the reference data, since the ^{109}Cd source have not used the collimator, and since the sensitivity for the ^{88}Y source have been calculated by using many simulation data.

. On the other hand, we measured by the γ - γ coincidence method to confirm the result using the ^{22}Na source with the pair annihilation and the 1275 keV gamma. The setup scheme is presented in Fig6. In one decay the ^{22}Na source emits two 511 keV gammas from the pair annihilation and one gamma with the energy 1275keV. Two 511 keV gammas are scattered by back to back. One side hits the NaI(Tl) detector, another side hits the TGC. On the other hand, the 1275 keV gamma hit the CsI detector placed in side of the collimater and the TGC. Then the coincident signal from

NaI(Tl) and CsI is used as the trigger signal. Furthermore the NaI(Tl) and CsI detector measure the energy, and pick up the 511 kev gamma for the NaI(Tl) detector and 1275 kev gamma for CsI detector. The energy distribution of NaI(Tl) and CsI detector with or without the coincidence signal, that is the trigger signal, are presented in Fig7 and Fig8 respectively. The oblique line region in these figure represents the distribution with the trigger signal. Furthermore the criteria of energy cuts is imposed on the both detector. In this case, the fake signal is the cosmic ray only. As a result of the measurement, the contribution of the fake signals were less than 0.6 % for the reality signals. The systematic errors is defined as the difference between the measurement value of 'self trigger mode' and 'γ - γ coincidence method'.

The result of measurement for the various energies is presented in Fig9 with the result of simulation.

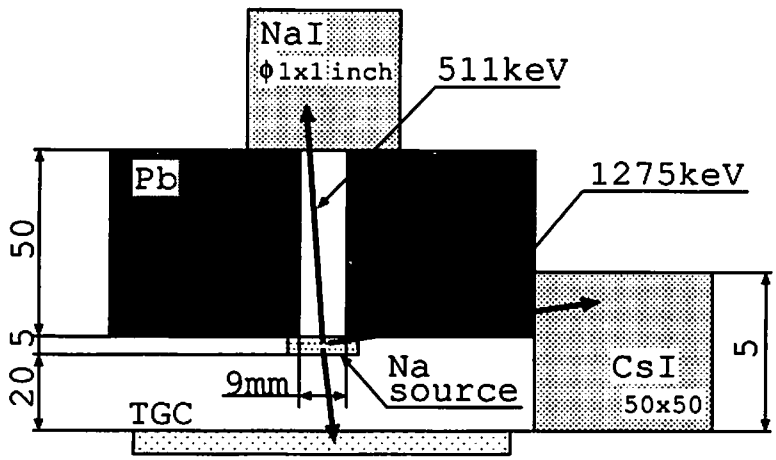

Figure 6: The setup of the coincidence method for ^{22}Na

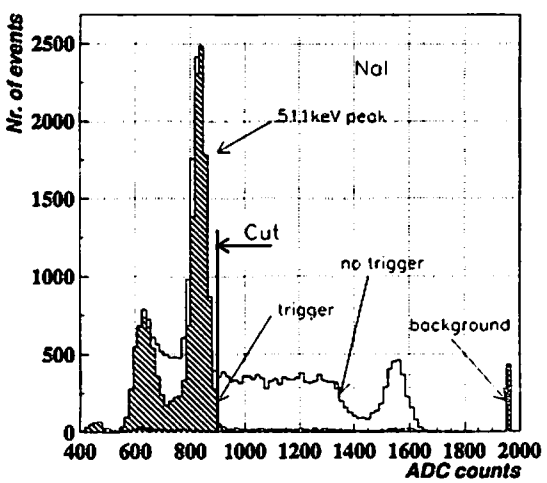

Figure 7: The energy distribution of NaI(Tl) detector. NaI(Tl) detector pick up the 511 kev gamma

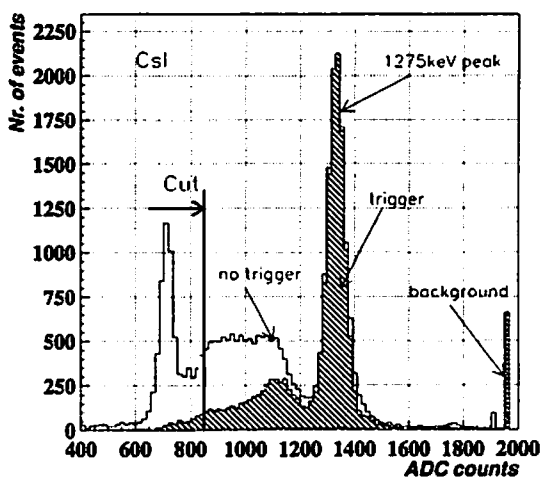

Figure 8: The energy distribution of CsI detector. CsI detector pick up the 1275 kev gamma

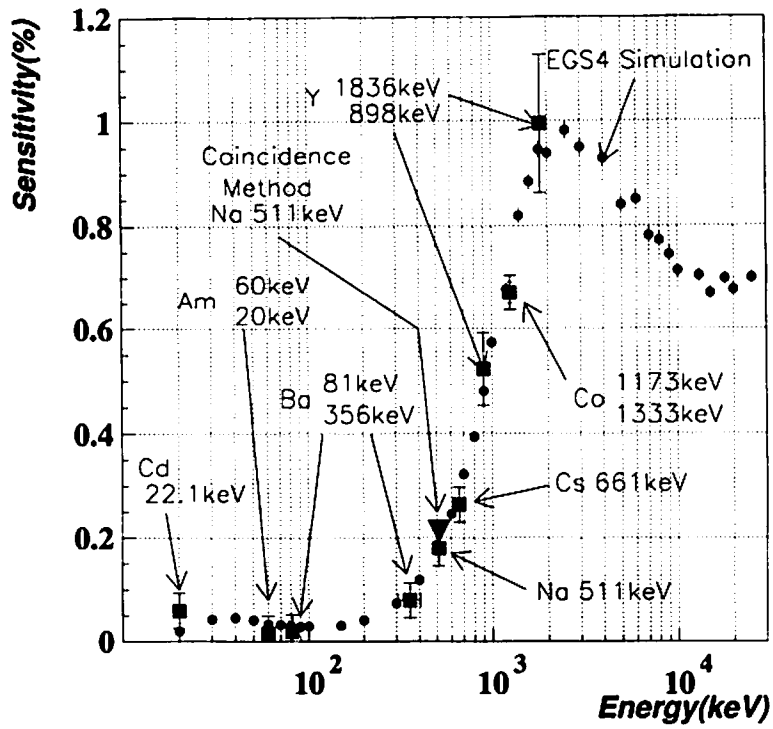

Figure 9: The sensitivity of gammas for the TGC

6 Summary

We measured the gamma sensitivity of the TGC using the radio active source with energy from 20 keV to 1.8 MeV. The result of the meaurement was compared with the EGS4 simulation. While the main detection process was the photoelectron effect in the low energy less than 100 keV according to the simulation, it was the compton scattering in the high energy nearly 1 MeV. We also measured by the γ - γ coincidence method to confirm the result using the ^{22}Na source with the pair annihilation and the 1275 keV gamma. The results of the measurement are in good agreement with the simulation value. Now we conclude that the aging effect on TGC's from the photon background is small enough in 10 years of LHC running. But the study of the other background particle, neutron remain undone. Now we are planning neutron radiation for TGC.

References

1) G.Battistoni et al. Muon Chamber Sensitivity to neutron and photn background in the ATLAS hall ATLAS Internal Nnote MUON-NO-052

2) A.Ferrari et al. Radiation Calculations for the ATLAS Detector and Experimental Hall

3) Aleandro Nisati Fake Level-1 Muon Trigger Rates in the ATLAS experiment ATL-DAQ-98-123

4) EGS4:Electron Gamma Shower http://ehssun.lbl.gov/egs/egs.html

SLOW POSITRON PROJECT AT NIHON UNIVERSITY

K. SATO, I. SATO, K. HAYAKAWA, T. TANAKA, Y. HAYAKAWA, H. NAKAZAWA[1], K. YOKOYAMA[1], K. KANNO[1], T. SAKAI[1], Y. MATSUBARA and I. KAWAKAMI

Atomic Energy Research Institute, Nihon University
7-24-1 Narashinodai, Funabashi-Shi, Chiba-Ken, 274-8501, Japan
[1] *College of Science and Technology, Nihon University*
7-24-1 Narashinodai, Funabashi-Shi, Chiba-Ken, 274-8501, Japan

Abstract

Slow positron facility is planned as one of many applications of the 125 MeV electron linac at Nihon University. The electron beam from the linac is passed through an undulator, producing FEL oscillation and then transported to the target-moderator assembly for slow positron production. In order to design the facility, positron production from the target was calculated using EGS4. Positron yield per unit beam power was found to be maximum at the beam energy of 100 MeV. In our case of 125 MeV beam energy, maximum positron yield was obtained at the Ta target thickness of 0.8 cm and energy deposit in the target is 2.4 kW. Using our 125 Mev,50 μ A(average current) electron linac we expect to obtain slow positron beam of more than $\sim 10^9$ e^+/sec. After accelerating it to 0-60 keV and changing it to short pulse of 150 ps, the slow positron beam is used in the research of material science. Fundamental research of positron microscope is also planned.

1 Introduction

The construction of 125 MeV electron linac was started in 1994 at Nihon University and completed March of 1998. Measurement of spontaneous emission from FEL system was observed by use of CCD camera[1]. The characteristics (energy spread and emittance)of the ele ctron beam were also measured[2]. The main object of our electron linac is to use it for FEL oscillation and even in the exit of FEL system, the electron beam has still more than 99 % of its original energy. So it is reasonable to use it for positron production after passing through FEL system. The electron beam from the electron linac at first passes through the undulator-optical cavity system to produce FEL oscillation and then is transported to the target-moderator system for slow positron production.

2 Slow Positron Production

Positrons can be produced by bombarding the target with the high energy electron beam. In the case of the tantalum target , positron yield was calculated using Monte Carlo Code: EGS4[3]. Fig.1 shows the beam energy dependence of positron yield. Vertical axis shows the positron numbers emitted per unit beam power. In consideration of thermalization efficiency[4] of positrons in the W foil, only positrons having emission angle of 0-10 degree and having energy of 0-10 MeV were plotted in Fig.1. In each beam energy, optimum target thickness was adopted in the calculation. Fig.2 shows the target thickness which gives maximum positron yield in each beam energy. From the

result of Fig.1, it is concluded that although positron yield increases in accordance of the increase of beam energy, positron yield divided by beam power has maximum at the beam energy of 100 MeV. So it is most efficient to use the electron linac of 100 MeV for positron production. In Fig.3 is shown the target thickness dependence of positron yield in the case of 125 MeV electron beam and tantalum target. In this result the maximum positron yield is obtained in the 0.8 cm thickness of Ta target. In fig.4 is shown the energy spectrum of positrons emitted forward(0-10 degree) in the case of the beam energy of 125 Mev and Ta target of 0.8 cm. The comparison was made between the result with PRESTA[5] and the result without PRESTA in Fig.4. The result with PRESTA is a little higher than that without PRESTA in the low energy region of positrons. Rate of Energy deposit was also calculated to be 0.39 when the electron beam passed through the Ta target. So in our case of 125 MeV and 50 μA electron beam, heat production in the target is 2.4 kW. Positrons from the target are moderated in the W foils and slow positrons are extracted by means of an extracting electrode. As the moderation eficiency of positrons in the W foils depends remarkably on the heat processing of W foils[6], we intend to design a moderator system which is able to do heat processing in a vacuum chamber. Assuming the thermalization efficiency of positrons to be 10^{-4}, we expect the slow positron beam of $\sim 10^9$ e^+/sec, using our 125 MeV and 50 μA electron linac .

3 Radiation Shielding of Experimental Area

The electron beam from the FEL system is transported to the target-moderator assembly by means of two 45° bending magnets and two Q magnets and bombards the Ta target which emits intense Bremsstrahlung radiation. The energy spectrum of Bremsstrahlung emitted forward was calculated using EGS4 and is shown in Fig.5. In the case of our 125 MeV and 50 μA, it is concluded from this spectrum that the absorbed dose rate at 1 m from the target in a forward direction is 52 Gy/sec. Dose rate in sideward direction is two orders lower than that of the forward direction. Because the experimental area is ,at present, separated from the target with ordinary concrete wall of 1m thick, radiation shield is insufficient. So the shielding wall will be increased to 1 m ordinary concrete wall plus 1 m heavy concrete wall. In addition the target-moderator assembly will be surrounded by steel slabs of 20 cm thick which will reduce the scattered gamma rays from the ceiling of the accelerator room. In order to reduce the gamma rays through the door between accelerator room and experimental room, the ordinary concrete blocks of 1 m cube will be placed in front of the door to 3 m height. By making these changes, we can expect the dose rate at any positions in the experimental room to be below 1 mSv/week .

4 Slow Positron Facility Plan at Nihon University

In fig.6 is shown the slow positron facility plan at Nihon university. The beam current of our electron linac is 200 mA at maximum and continues in 20 μsec at a repetition rate of 12.5 Hz . The beam produces slow positrons of$\sim 10^8$ during 20 μsec at the repetition rate of 12.5 Hz which induces pulse pile-up in the positron detector. It is necessary to convert the slow positron beam to quasi-continuous positron beam. This conversion will be acomplished by Penning trap method. After penning trap electrode, positron pulsing device will be installed, which is necessary for life time measurement of positrons in the material sample. The pulsing device consists of chopper, subharmonic prebuncher, buncher , drift tube. This kind of pulsing device was already utilized at Electrotechnical Laboratory[7] and slow positron pulse of 150 ps in width was obtained. Moreover the acceleration of slow positrons will be made in the energy range of 0 - 60 keV for the purpose of position dependent probing of the material sample. Slow positron beam line is utilized mainly for the research of material science . Fundamental research on transmission positron microscope is

also planned .

Acknowledgement
The authors would like to thank Prof. Hideo Hirayama KEK for his kind help in using EGS4.

References

1) Y. Hayakawa et al,"MEASUREMENT SYSTEM FOR LEBLA USING A THERMOELECTRIC COOLED CCD", Proc. of the 24th Linear Accelerator Meeting in Japan 368-370(1999) in Japanese.

2) K. Yokoyama et al,"BEAM CHARACTERISTICS OF FEL LINAC AT NIHON UNIVERSITY II", Proc. of the 24th Linear Accelerator Meeting in Japan 359-361(1999) in Japanese.

3) W. R. Nelson, H. Hirayama and D. W. O. Rogers,"THE EGS4 CODE SYSTEM", *SLAC-REPORT 265*(1985).

4) H. Kaneko, S. Okada, "Consideration on Electron Linac and Target System for the Positron Factory(II)", Proc. of the Third EGS4 Users' Meeting in Japan 46-48 (1993) in Japanese.

5) A. F. Bielajew and D. W. O. Rogers,"PRESTA : THE PARAMETER REDUCED ELECTRON-STEP TRANSPORT ALGORITHM FOR ELECTRON MONTE CARLO TRANSPORT", *Nucl. Instr. Methods* **B18**(1987) 165-181.

6) A. Enomoto, T. Kurihara, H. Kobayashi, T. Shidara, A. Shirakawa, K. Nakahara, T. Suzuki, H. Hirayama, Y. Ito and M. Hasegawa, "Construction Report of the PF Slow-Positron Source(1)", *KEK Report 93-13*(1993) in Japanese.

7) R. Suzuki, Y. Kobayashi, T. Mikado, H. Ohgaki, M. Chiwaki, T. Yamazaki and T. tomimasu, "Slow Positron Pulsing System for Variable Energy Positron Lifetime Spectroscopy", *Jpn. J. Appl. Phys.* **30** L532(1991).

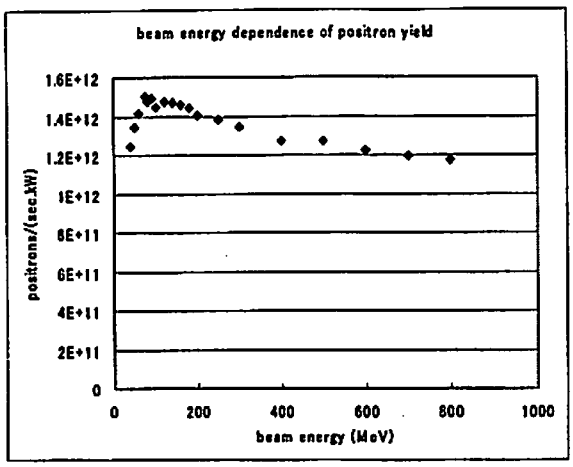

Fig.1 Beam energy dependence of positron yield . Only positrons having emission angle of 0-10 degree and having energy of 0-10 MeV are selected. Vertical axis shows positron intensity per beam power of 1 kW

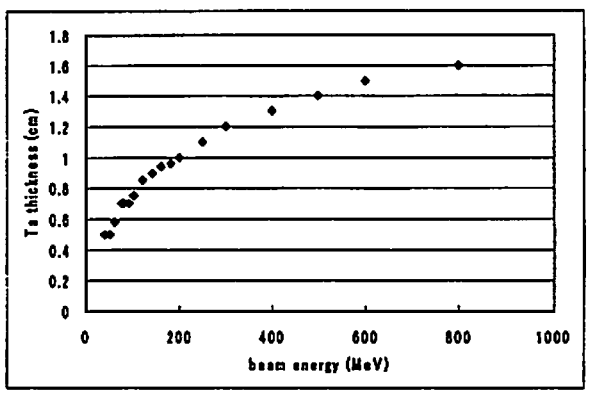

Fig.2 Ta target thickness for maximum positron yield

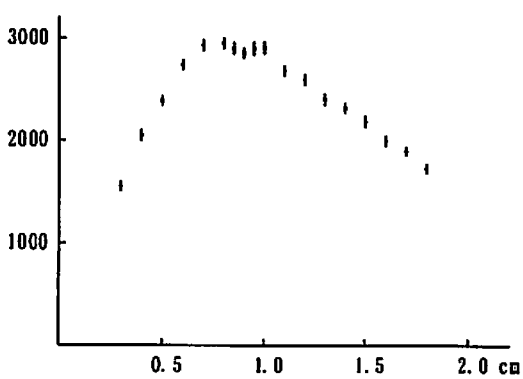

Fig.3 Target thickness dependence of positron yield . The electron beam energy is 125 MeV Target meterial is tantalum .

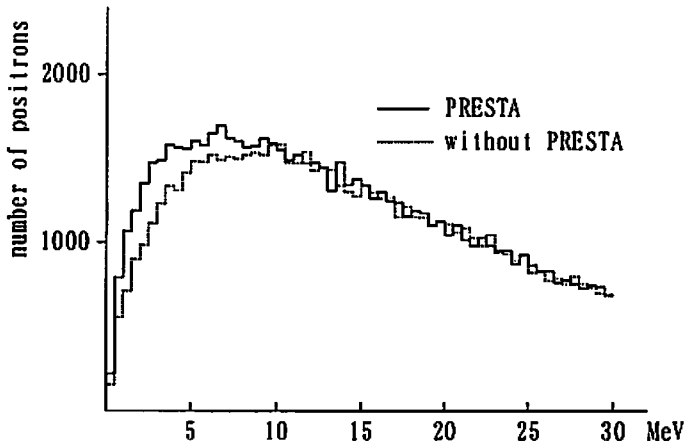

Fig.4 The energy spectrum of positron in the case of beam energy of 125 MeV and Ta target of 0.8 cm thick .

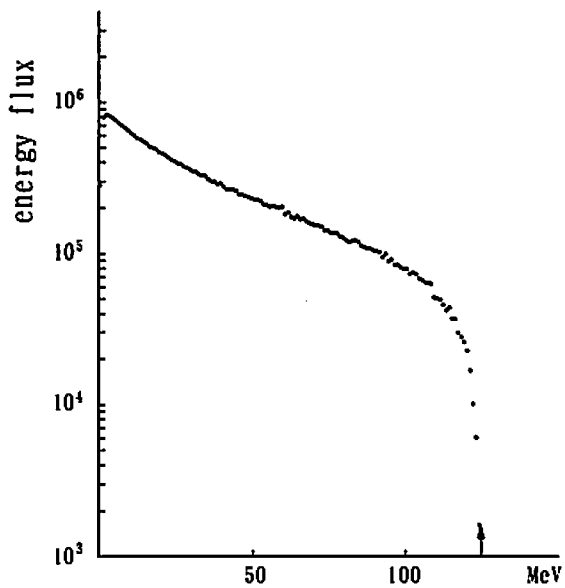

Fig.5 Bremsstrahlung spectrum emitted forward from the Ta target of 1.0 cm thick. Beam energy is 125 MeV.

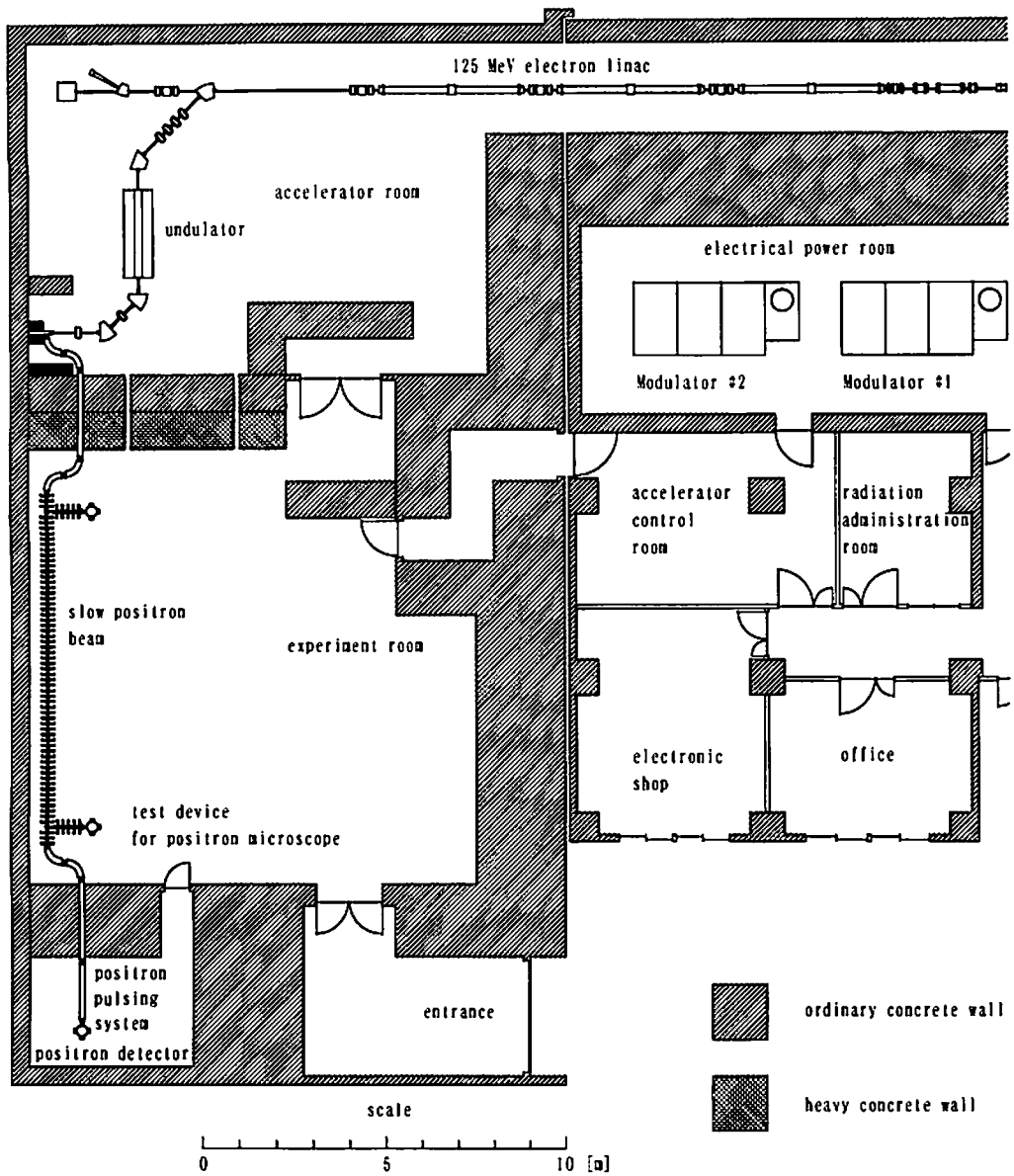

Fig.6 Slow Positron Facility Plan at Nihon University

EXAMINATION OF THE X-RAY PIPING DIAGNOSTIC SYSTEM USING EGS4 (IN CASE CONSIDERING SPECTRUM OF X-RAY)

G. KAJIWARA

Shimizu Corporation Institute of Technology
3-4-17 Etchujima, Koto-ku, Tokyo, 135-8530 Japan

Abstract

EGS4 code was used to simulate the exposure of an X-ray film under conditions similar to the practical radiography in order to determine the possibility of using an X-ray piping diagnostic system on corroded steel pipes. Considering the spectrum that X-ray bulb generates, the absorbed energy of a steel plate placed in front of the X-ray apparatus is simulated using EGS4. The results of the simulation are very similar to the results of radiography measurements of the density of a film on which the same plate is radiographed. These results indicates the possibility of using the X-ray piping diagnostic system to diagnose pipes with rust.

1 Introduction

Since its development ten years ago, the X-ray piping diagnostic system used for renewal construction or planninghas been an effective and practical system for determining the number of residual years of old piping, nearly 500 actual results. The thickness of the wall in an old pipe is estimated using the relationship between steel thickness and film density. However, the system does not work when the density of the steel changes due to the accumulation of rust. Electron Gamma Shower 4 (EGS4) was used to overcome this problem.

2 X-ray Piping Diagnostic System

Figure 1 shows the X-ray piping diagnostic system. Figure 2 shows the method of estimating the thickness of the corroded part using the relationship between the thickness of steel and film density. A standard pipe is radiographed at four selected points with varying thickness. The estimate would be more precise if the relationship were proportional, but the densities of the film for each point do not vary linearly versus the X-ray exposure of the film. Moreover, differences in a film development conditions such as time affect the density of films exposed for the same amount of time. These differences can be overcome by radiographing a ruler with standard thickness along with the piping on the same film. The relationship between the density and the thickness is thus acquired on the same developed film.

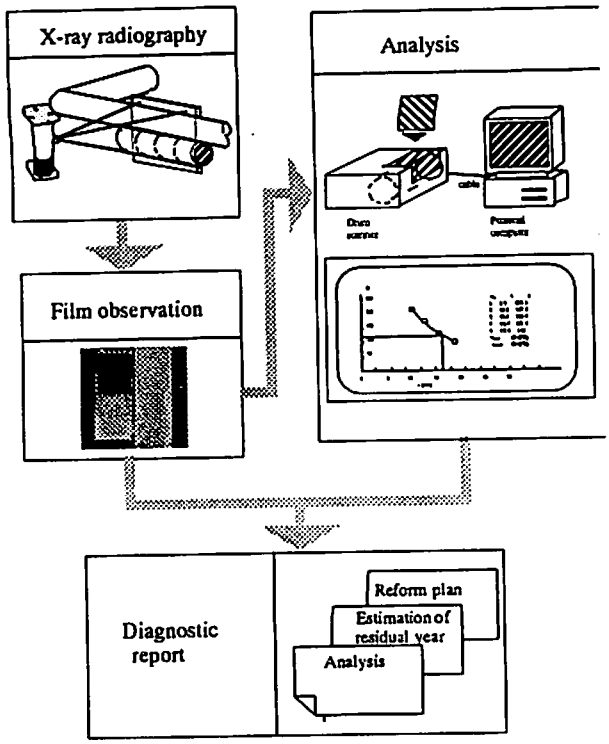

Fig.1. An outline of X-ray piping diagnostic system.

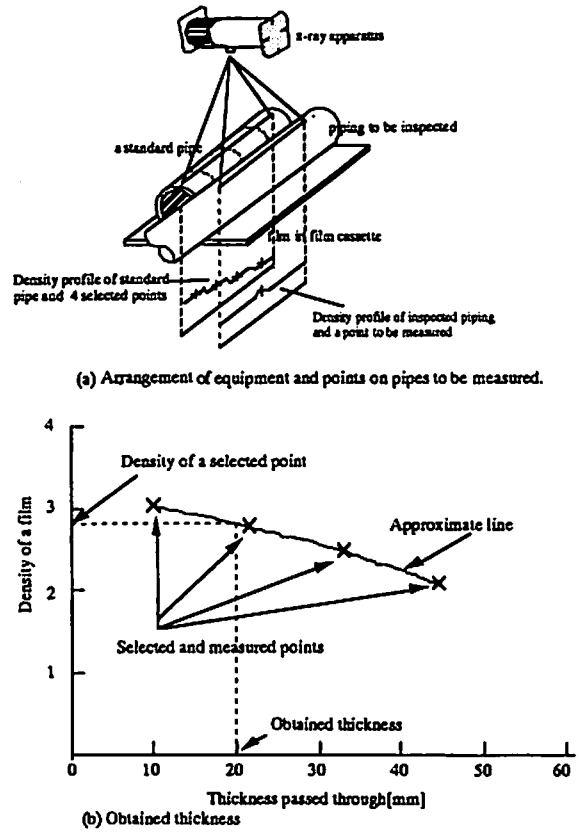

Fig.2. Method of obtaining thickness of corroded piping.

3 Simulation

3.1 X-ray source

A portable X-ray apparatus with a glass X-ray bulb was used (as shown in Fig. 3). The bulb was covered with a cylindrical aluminum plate. The simulation was carried out only with the tungsten target, not with glass and aluminum, as shown in Fig. 4. Output voltage was set at 150 kV. Electrons hit the tungsten target at an incident angle of 22 degrees, and the spectrum of the X-rays, which was emitted in the angle from 107 degrees to 117 degrees, was calculated. The spectrum emitted from the tungsten target is shown in Fig. 5. By using probability distribution function (pdf) this spectrum was made into the input spectrum for the following simulation of the film.

3.2 Film density

The X-ray film has two layers of emulsion, as shown in Fig. 6. The results of reading the density of a film that shows a radiographed iron contrast meter consisting of 15 steps (shown in Fig. 7) are shown in Fig. 8. The thickness of a steel plate in the simulation model was varied as shown in Fig. 9. Ranmar variable was used, and the maximum number of cases counted in the simulation was 5,000,000. The level of energy absorption of the film was obtained for a plate thickness of 15 mm as shown in Fig. 10. A comparison of the two results, indicates that the

density variation curve and the energy absorption curve are very similar, as shown in Fig. 11. The conditions of radiography are as follows:

1. The X-ray generator operates at 150 keV.
2. X-ray bulb: SIO-160-5E (Hitachi Medico Co.)
3. X-ray apparatus: Rix-200NM (Rikodenki Co.)
4. X-ray film (Fujifilm Co. #80)
5. Densitometer (Abesekkei Co. Drum scan densitometer)

4 Summary

A complete simulation was carried out of the X-ray diagnostic system for changes in steel plate thickness. Good conformity of the results of this simulation indicates the possibility of successfully carrying out simulations in which parameters such as density or voltage are changed. The results also suggest the possibility of measuring the pipe thickness of pipes with rust. Future work will include comparisons of simulations and practical radiography under such parameters as well as analyses of rust in steel pipes for simulating pipes with rust conditions.

Acknowledgements

I am very grateful to Hideo Hirayama of KEK (High Energy Research Organization) who assisted me in using EGS4, especially concerning X-ray bulb simulation.

References

1) G. Kajiwara, "X-ray piping diagnostic system", *Journal of Testing and Evaluation*, **Vol. 26**, 1998, pp. 346-351.

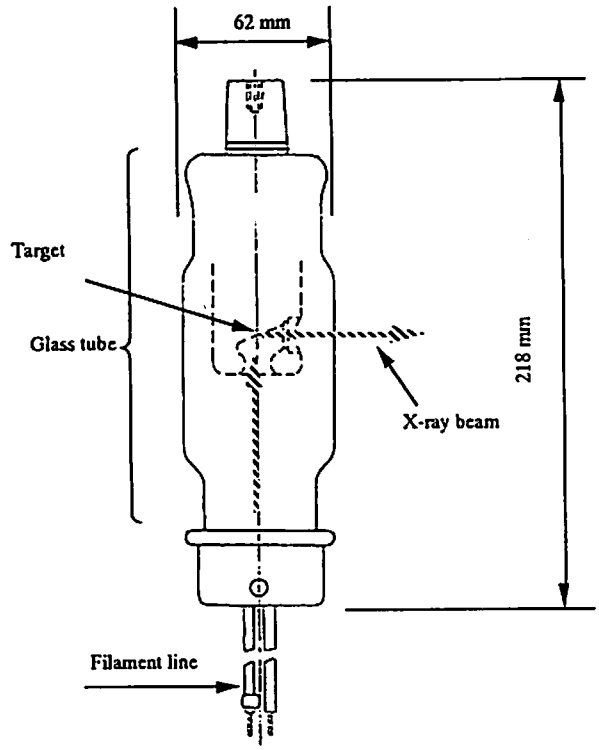

Fig.3. The structure of an X-ray bulb.

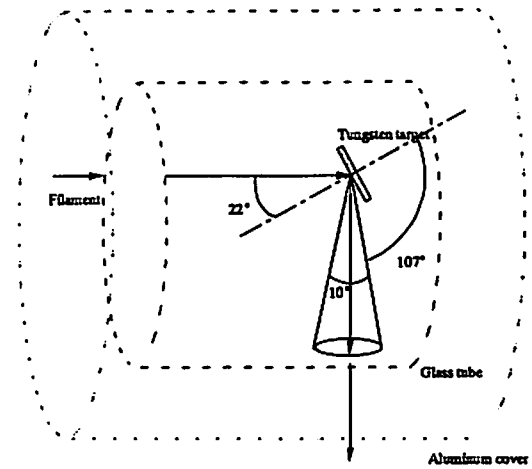

Fig.4. Simulation model of X-ray generation.

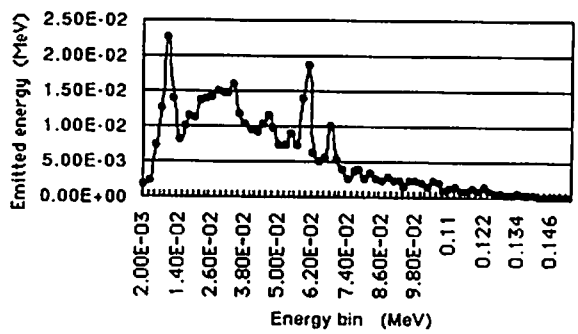

Fig.5. X-ray spectrum at 150 kV.

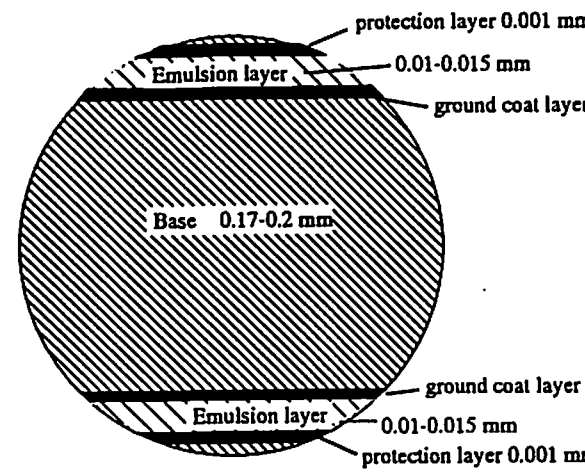

Fig.6. Composition of X-ray film for industrial use.

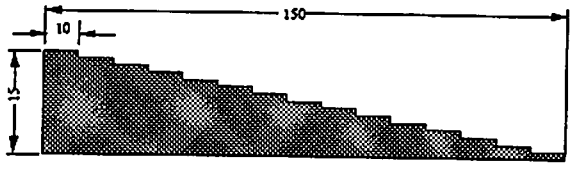

Fig.7. Cross section of a contrast meter(mm).

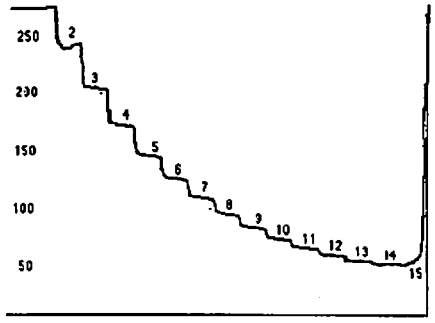

Fig.8. The relationship between steel thickness and density of a film radiographed at 150 kV.

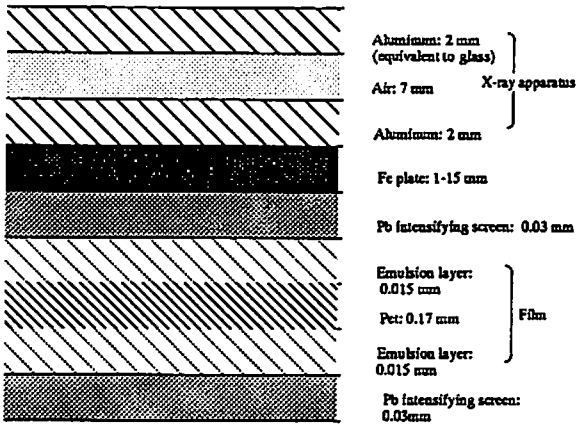

Fig.9. Model structure for simulation.

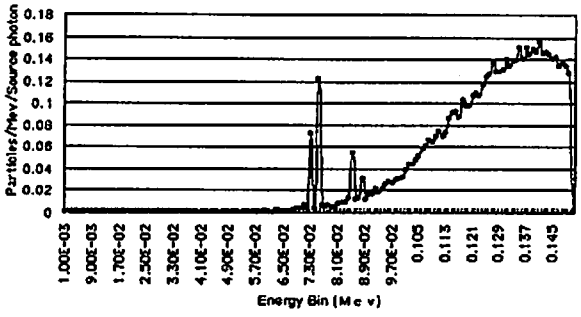

Fig.10. X-ray spectrum absorbed in a film.
X-ray emitted at 150 keV
Fe plate thickness: 15mm

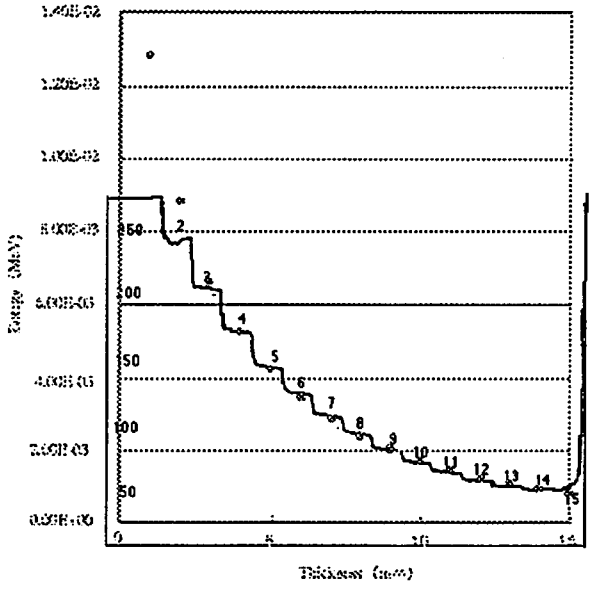

Fig.11. Steel thickness-Energy absorption at 150 kV. The points indicate the energy absorption and the stepped curve indicates the film density. Numbers on the stepped curve indicates the thickness of the contrast meter.

RESPONSE FUNCTION SIMULATION FOR A WHOLE-BODY COUNTER

S. KINASE

Japan Atomic Energy Research Institute
2-4 Shirane, Shirakata, Tokai-mura, Ibaraki 319-1195 Japan

Abstract

Counting efficiencies of a whole-body counter were calculated using Monte Carlo simulation so as to improve accuracy on the assessment of body burdens with a whole-body counter. Consequently, the relationship between counting efficiencies and photon energies, particularly multiple-scattering components of counting efficiency for monoenergetic photons, was identified quantitatively.

1 Introduction

A whole-body counter is used for measurements of body radioactivity made in programmes of internal dosimetry for occupational radiation monitoring. The apparatus is useful for (i) indications of the distribution of radionuclides in the body, (ii) identification and (iii) quantitative assessment of mixtures of nuclides. In order to measure body burdens with a whole-body counter, it is necessary to have equipment applying gamma ray spectrometry and to have obtained reliable counting efficiencies by calibration. However, the number of phantoms is limited, and is inadequate for calibration. Hence, energy dependence of counting efficiencies (counting efficiency curve) should be obtained by applicable calibration without using any phantoms, i.e., calculation.

We have investigated counting efficiencies of a whole-body counter for several radionuclides using Monte Carlo simulation [1,2,3] . This work was performed to determine total absorption peak distribution of the whole-body counter for a phantom which contained radionuclides, to obtain the counting efficiency curve and to investigate multiple-scattering components of the counting efficiency.

2 Materials and Methods

Figure 1 shows the calculational geometry. The whole-body counter and the water-filled block-shape phantom were modeled after those at Japan Atomic Energy Research Institute (JAERI). The whole-body counter has five cylindrical 8-inch-diameter x 4-inch-length thallium-activated sodium iodide [NaI(Tl)] detectors, the sensitivity along the longitudinal axis of the body to a monoenergetic point isotropic source (662 keV) is uniform with an arrangement of the subject-detector configuration. The phantom consists of 5 mm vinyl chloride vessels of rectangular cross-section, and is filled with radionuclides in solution.

Monte Carlo simulation was carried out using the EGS4 code system with a user code for general purpose (UCGEN) [4,5] . A million histories were determined for the number of histories, the photon cross sections for materials were taken from PHOTX [6] .

The response functions calculated by the EGS4 code were folded with a Gaussian distribution since the energy resolution of the detector is not considered by the EGS4 code [7] .

As shown in Fig. 2, counting efficiency of the whole-body counter was obtained as the ratio of total absorption peak counts (double the FWHM of the absorption peak) to the activity of the phantom. For quantitatively investigating multiple-scattering components of counting efficiency, peak efficiency was obtained as the ratio of the total absorption peak counts (10 keV-bin peak of the response function that was not folded) to the activity of the phantom.

To validate the calculations, calculated counting efficiencies for point sources were compared with measured ones.

3 Results and Discussion

Figure 3 shows calculated and measured counting efficiencies for the point sources. The agreement between calculation and measurement is very good in the energy range of 300 to 1,461 keV. This result would testify of the validity of the calculations. Peak efficiencies of the whole-body counter for the point sources are also shown in Fig. 3. The peak efficiencies for the point sources, which contain few multiple-scattering components, are nearly equal to the counting efficiencies for those.

Figure 4 shows total absorption peak distribution of the whole-body counter for both the point sources and the water-filled block-shape phantom. From a comparison with the results, it can be stated that the multiple-scattering components in the total absorption peak distribution for the phantom decrease with an increase in energy.

Figure 5 shows counting efficiencies and peak efficiencies of the whole-body counter. It was found that self-absorption and multiple-scattering components in the phantom play an important role in counting efficiencies of the whole-body counter. The multiple-scattering components of counting efficiency for 662 keV photons is about 10 %.

4 Conclusions

The following conclusions were derived from the results and discussion.

1. The multiple-scattering components of counting efficiency for the phantom decrease with increasing photon energy.

2. Self-absorption and multiple-scattering components in the phantom play an important role in counting efficiencies.

3. The multiple-scattering component of counting efficiency is about 10 % for 662 keV.

References

1) Kinase, S., *JAERI-Review 98-015*, 167(1998), [in Japanese].

2) Kinase, S., *J. Nucl. Sci. Technol.* **35** ,958(1998).

3) Kinase, S., *J. Nucl. Sci. Technol.* **36** ,952(1999).

4) Nelson, W. R. et al., *SLAC-265*(1985).

5) Nojiri, I. et al., *Dounengihou* **102**, 59(1997), [in Japanese].

6) PHOTX:RSIC Data Package, *DLC-136*(1989).

7) Saito, K. and Moriuchi, S., *JAERI-1306*(1987), [in Japanese].

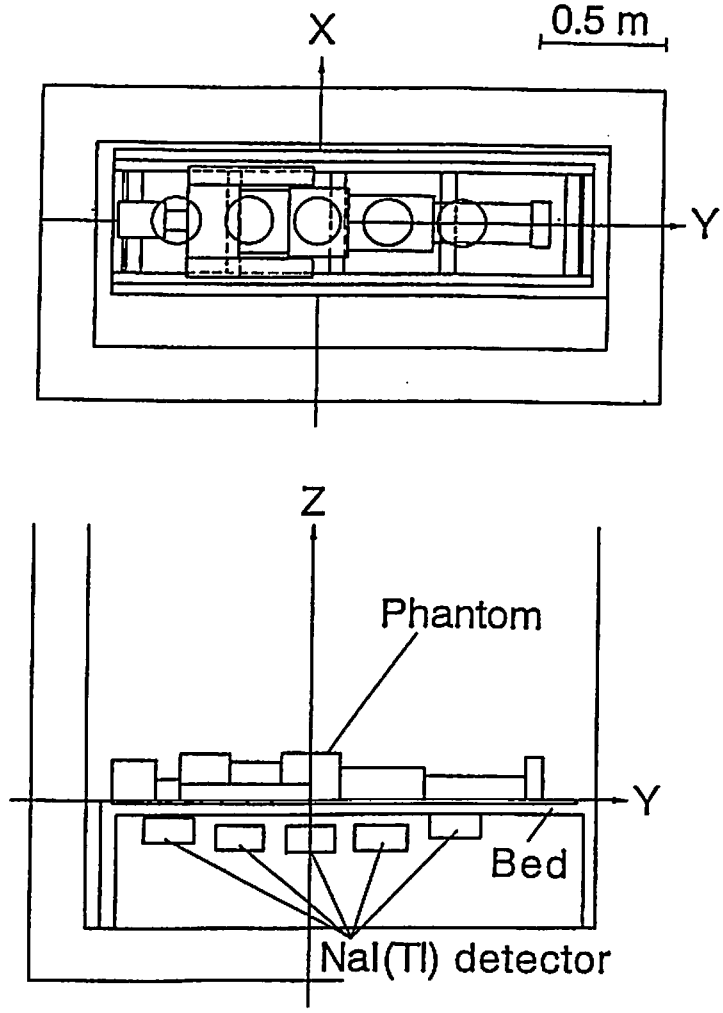

Fig. 1 Geometry of a whole-body counter and phantom.

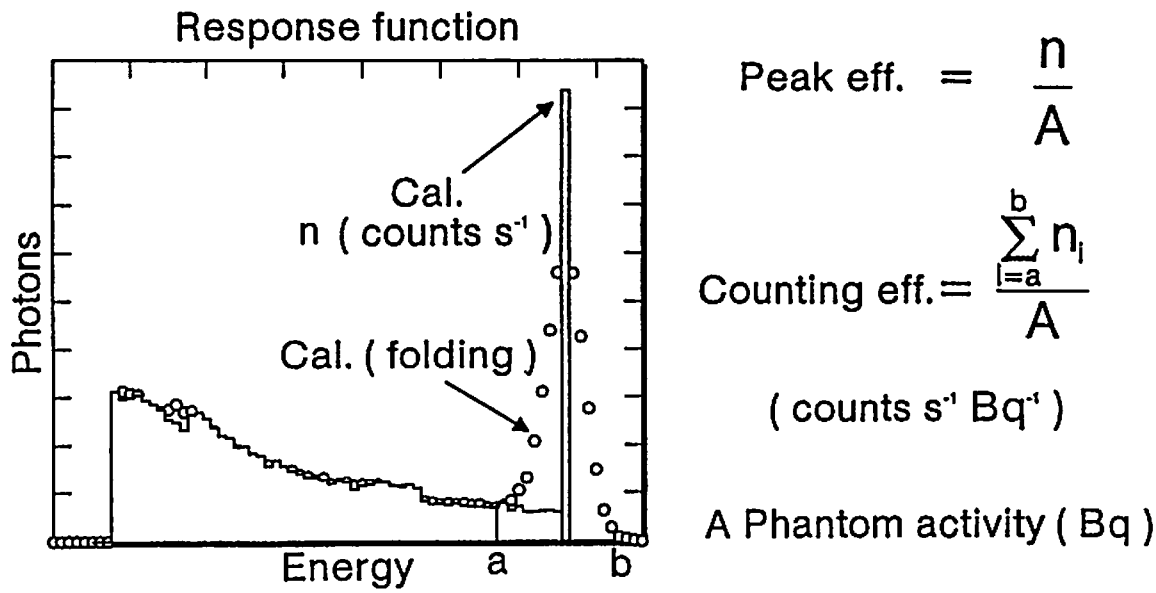

Fig. 2 Peak efficiency and counting efficiency.

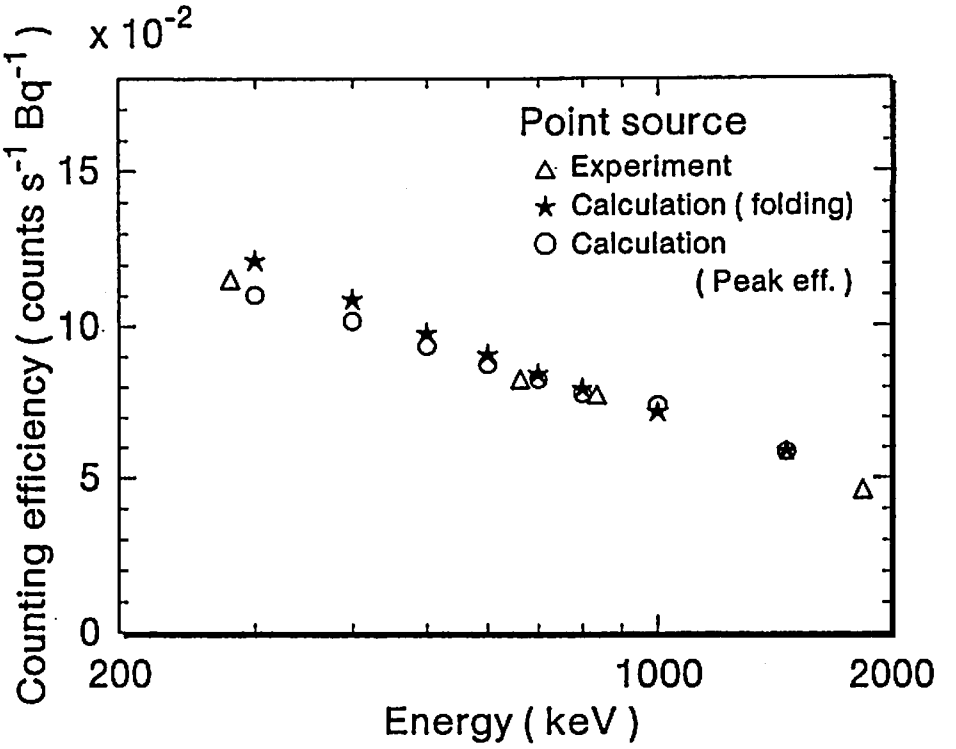

Fig. 3 Comparison of calculated and measured counting efficiencies for point sources.

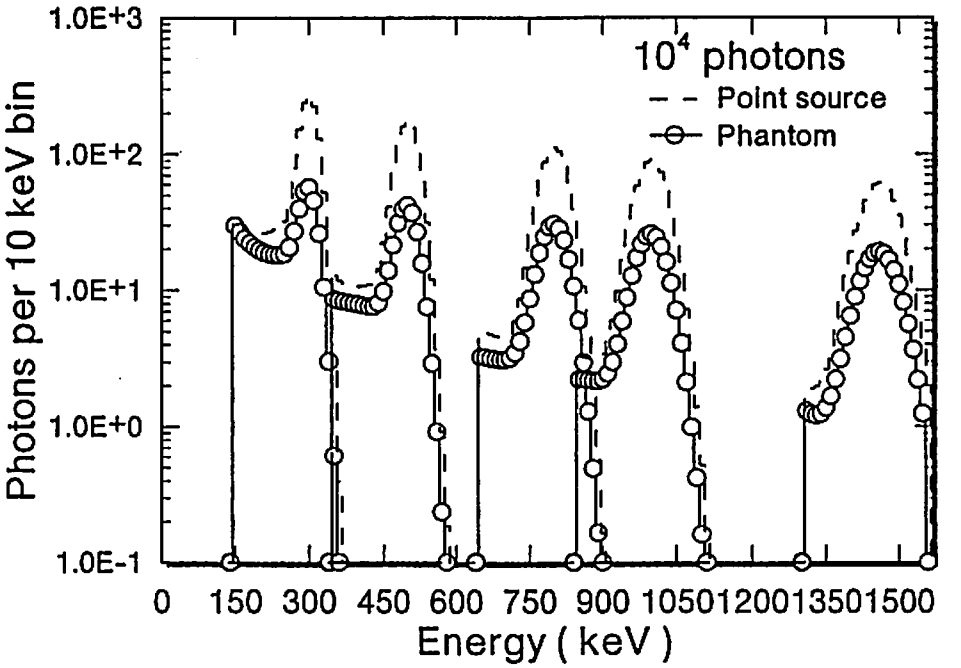

Fig. 4 Total absorption peak distribution of a whole-body counter for point sources and a phantom.

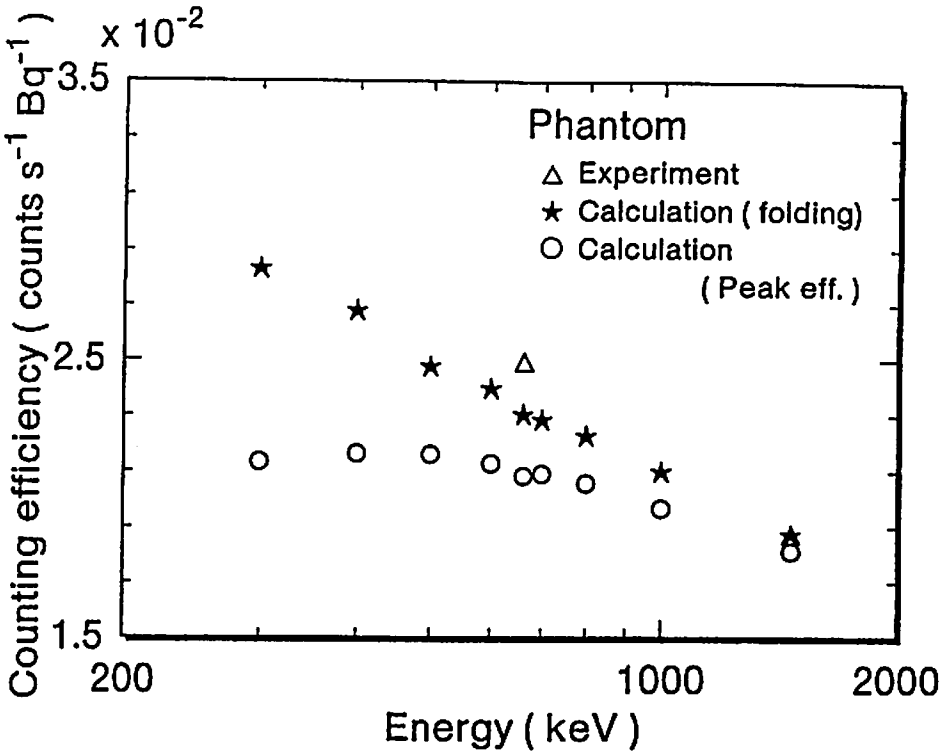

Fig. 5 Counting efficiencies of a whole-body counter for a phantom.

A STUDY ON DOSIMETRY OF STEREOTACTIC IRRADIATION

H. SAITOH, T. FUJISAKI[1], S. ABE[1], M. FUKUSHI and K. FUKUDA

Tokyo Metropolitan University of Health Sciences
7-2-10, Higashi-Ogu, Arakawa-Ku, Tokyo 116-8551 Japan
[1]*Ibaraki Prefectural University of Health Sciences*
4669-2, Ami-Machi, Inashiki-County, Ibaraki 300-0394 Japan

Abstract

Stereotactic irradiation using a linear accelerator has been widely adopted in many hospitals recently. For this radiotherapy technique, accurate dosimetry is important for defining the position and dimensions of the irradiation field, and determining the absorbed dose to target volume. Nevertheless, there are some uncertainties caused by a smaller field than conventional techniques. A cause for the uncertainties is a variation in the energy spectrum and other cause is a spatial resolution of detector.

In this study, the energy spectrum and dose distribution in water was calculated using the EGS4 Monte Carlo method. The field size and depth dependence of energy spectrum and stopping power ratio was investigated. In addition, the optimal detector size was also investigated.

It is evident that electron and photon energy spectrum changes as a function of field size and depth in water. Nevertheless, it is evident that variation in stopping power ratio caused by a variation in the energy spectrum is less than 1% for an energy range below 10 MV. Furthermore, it is evident that the absorbed dose reading changes as a function of detector diameter. The allowable maximum diameter, which has a difference within 2% from an ideal detector, is less than 1/3 and 1/4 of field diameter for 4 and 10 MV, respectively.

1 Introduction

Stereotactic irradiation using a linear accelerator has been widely adopted in many hospitals recently. For this radiotherapy technique, accurate dosimetry is important for defining the position and dimensions of the irradiation field, and determining the absorbed dose to target volume.

Nevertheless, there are some uncertainties caused by a smaller field than conventional techniques [1]. A cause for the uncertainties is a variation in the energy spectrum [2, 3]. In the case of x rays emitted from a linear accelerator, the mean energy of photons will increase with depth due to the beam hardening effect. Furthermore, in the case that the field radius is less than the maximum range of a recoil electron, the result will be a lack of lower energy electrons, which travel from a distant point inside the field. Consequently, the mean energy of electrons may increase. These phenomena may affect the energy spectrum of photons and electrons as a function of field size and depth.

A data acquisition for stereotactic irradiation beam is mainly based on silicon diode detector, photographic film, radiochromic film and diamond detector. In the case of small field, an ionization

chamber is inadequate for the measurement of spatial dose distribution because of its relatively large sensitive volume. The significant discrepancies between the reading of some solid detectors and that of an ionization chamber have been reported [4]. Therefore, a different cause for the uncertainties is a spatial resolution of detector.

In this study, the energy spectrum and dose distribution in water was calculated using the EGS4 Monte Carlo method. As a result, the mean energy of photons and electrons (and positrons) were given as a function of field size and depth. In addition, the absorbed dose reading was given as a function of detector diameter. Furthermore, the field size and depth dependence of stopping power ratio and the optimal detector size was also investigated.

2 Methods

The beam intensity from a clinical machine is so high that spectrometry can only be performed indirectly. Therefore, the Monte Carlo simulation is employed as a highly reliable spectrometry method [5]. Furthermore, the Monte Carlo simulation is employed as an ideal dosimetry method since it has no energy dependency, no geometrical error, no perturbation and arbitrary sensitive volume can be set. We used the general purpose Monte Carlo code system EGS4 with PRESTA [6, 7], and coded an EGS4 user program for this study.

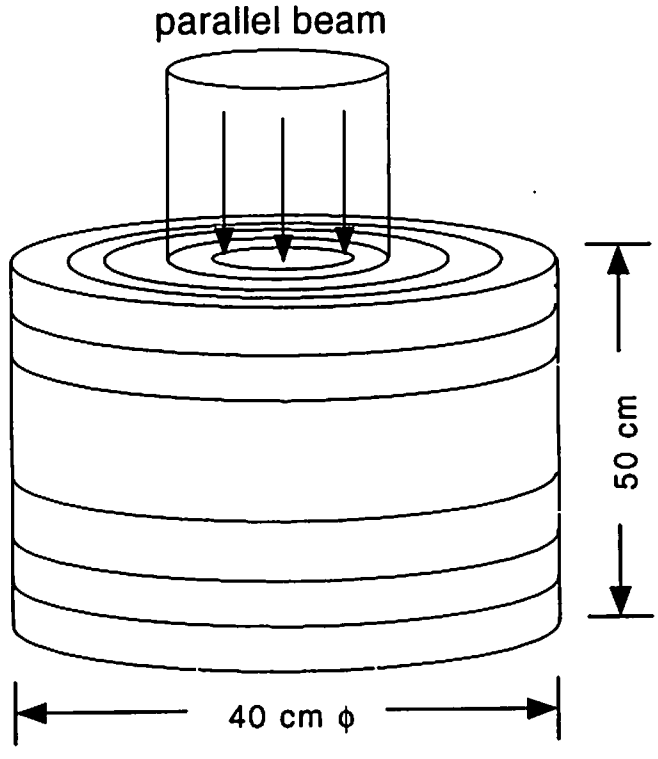

Figure 1 Geometrical arrangement of Monte Carlo simulation for energy sampling and dose distribution calculation.

Figure 1 shows the geometrical arrangement of simulation. Incident photons were normally impinged to the surface of a 40 cm in diameter by 50 cm thick water cylinder. In this cylinder, imaginary planes were arranged perpendicular to beam axis. The field was divided into imaginary concentric cylinders. For the energy spectrum sampling, the energy and radial position were recorded when the particle passed through the plane. For dose distribution calculation, the imparted energy to the volume, which was segmented by planes and cylinders, was accumulated.

Limited amounts of energy spectrum data have been published on clinical beams. The energy spectra for a ^{60}Co unit [8], 4, 6 and 10 MV linear accelerator [9] were used in the simulation. It was assumed that the field size and field position dependence of the energy spectrum for incident photons is negligible in this study. A set of 1×10^6 to 1×10^7 photons was generated per batch and ten batches were performed for field diameter of 0.5 to 20.0 cm. Simulations were done in a condition of transport cutoff parameter ECUT=0.521 MeV and PCUT=0.01 MeV, electron step-size limit parameter ESTEPE=0.05. The cross section data set of water was calculated in a condition of energy cutoff parameter AE=0.521 MeV and AP=0.01 MeV with PEGS4 as a preprocessor of EGS4.

3 Results

3.1 Variation in energy spectrum

Figure 2 shows the photon energy spectra at a 5 cm depth for 10 cmϕ and 0.5 cmϕ fields of 10 MV x rays. The field size dependence of the photon energy spectrum was not evident above 3 MeV. Nevertheless, it was discernible below 2 MeV that photon fluence for the 0.5 cmϕ field was less than the 10 cmϕ field.

In a Compton interaction between a high energy photon and an electron, the electron is recoiled forward and the photon travels at an obtuse scatter angle with lower energy. In a small field, the mean photon energy increases at deeper points because of a decreasing number of lower energy photons.

Figure 3 shows the variation in mean photon energy as a function of field diameter and depth for 10 MV x rays. The mean energy increased as field size decreased and depth increased.

Figure 4 shows the electron energy spectra for 10 cmϕ and 0.5 cmϕ fields at 5 cm and 25 cm depths of 10 MV x rays. At a 5 cm depth, the field size dependence of the electron energy spectrum was not evident within the entire energy range. However, electron fluence below 1.5 MeV for a 0.5 cmϕ field was slightly less than for a 10 cmϕ field. At a 25 cm depth, it was notable below 1.5 MeV that electron fluence for a 0.5 cmϕ field was less than for a 10 cmϕ field.

In a small field, the lower energy electrons will decrease because electrons travel outside the field due to multiple scattering. Furthermore, at deeper points, fluence of lower energy electrons will decrease because the fluence of lower energy photons decreases as a result of the beam hardening effect. Consequently, the mean energy of electrons increases as the field size decreases and depth increases.

Figure 5 shows the variation in mean electron energy as a function of field diameter and depth for 10 MV x rays. The mean energy increased as field size decreased and depth increased. The variation in mean electron energy increased as incident photon energy increased.

Figure 6 shows the absorbed dose reading as a function of detector diameter at peak depth for a 1.0 cmϕ field of 10 MV x rays. Where, the absorbed dose reading is the reading of mean imparted energy to the coin shape volume as a detector. This volume was made of water, arranged on beam axis and constant 0.5 cm thick by arbitrary diameter in dimensions.

The absorbed dose reading decreased as detector diameter increased. A major cause for this phenomenon is an absence of lateral electronic equilibrium in a sensitive volume.

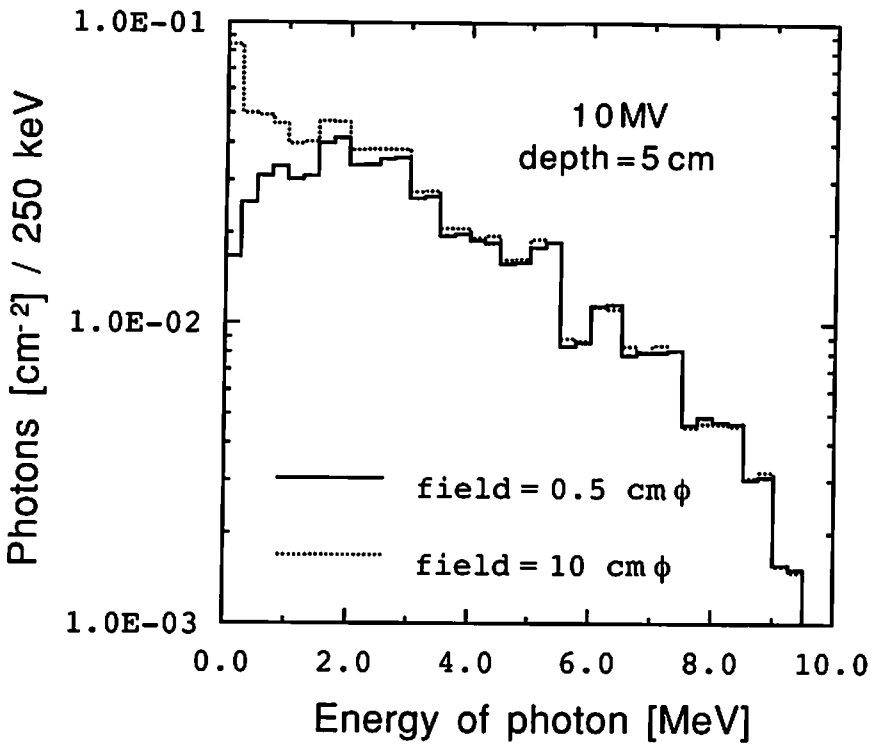

Figure 2 Comparison of photon energy spectra at a 5 cm depth in water for 10 cmϕ and 0.5 cmϕ fields of 10 MV.

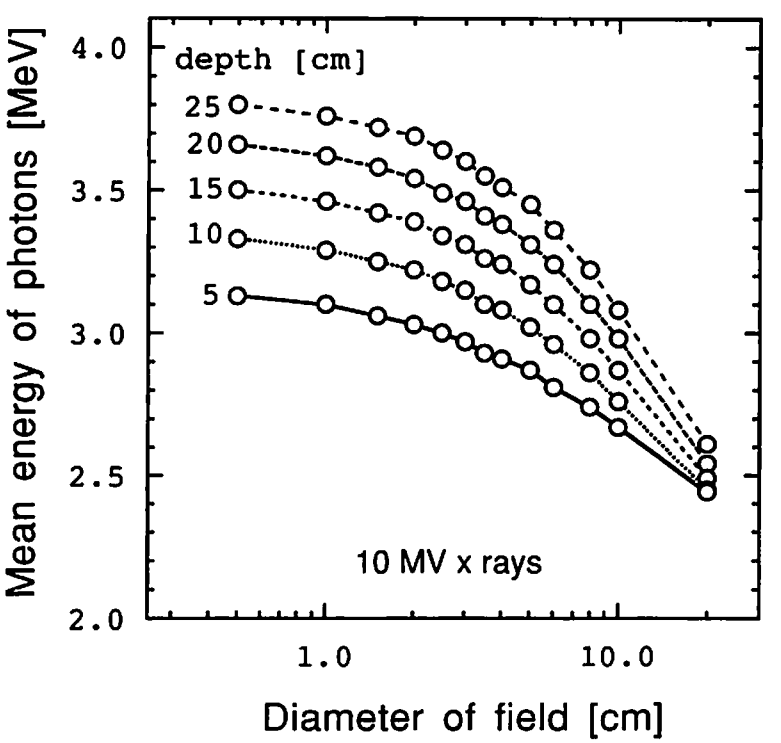

Figure 3 Variation in mean photon energy as a function of field diameter at 5, 10, 15, 20 and 25 cm depths in water for 10 MV x rays.

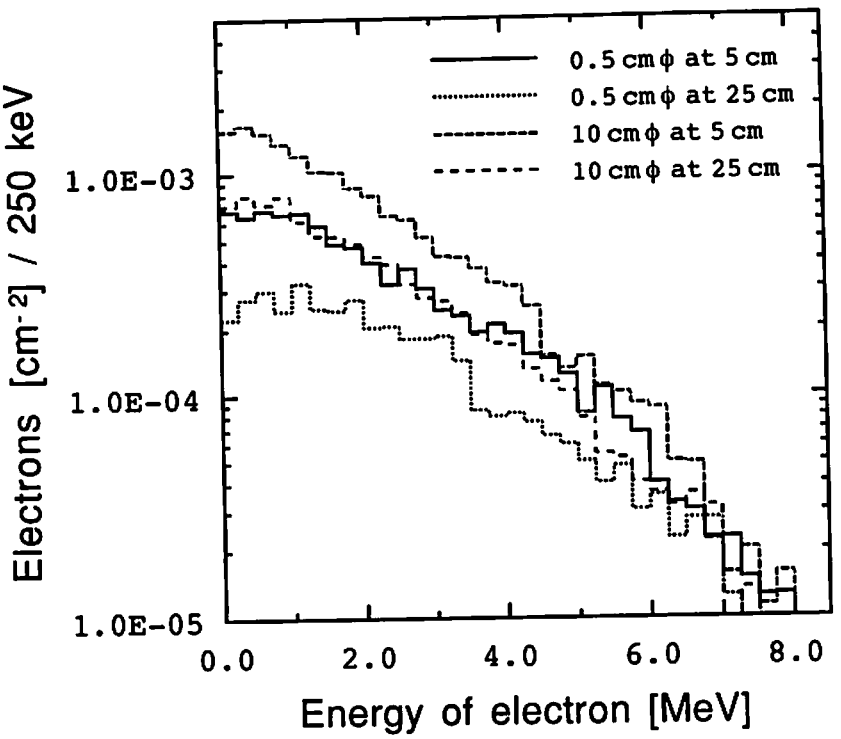

Figure 4 Comparison of electron energy spectra at 5 cm and 25 cm depths in water for 10 cmϕ and 0.5 cmϕ fields of 10 MV.

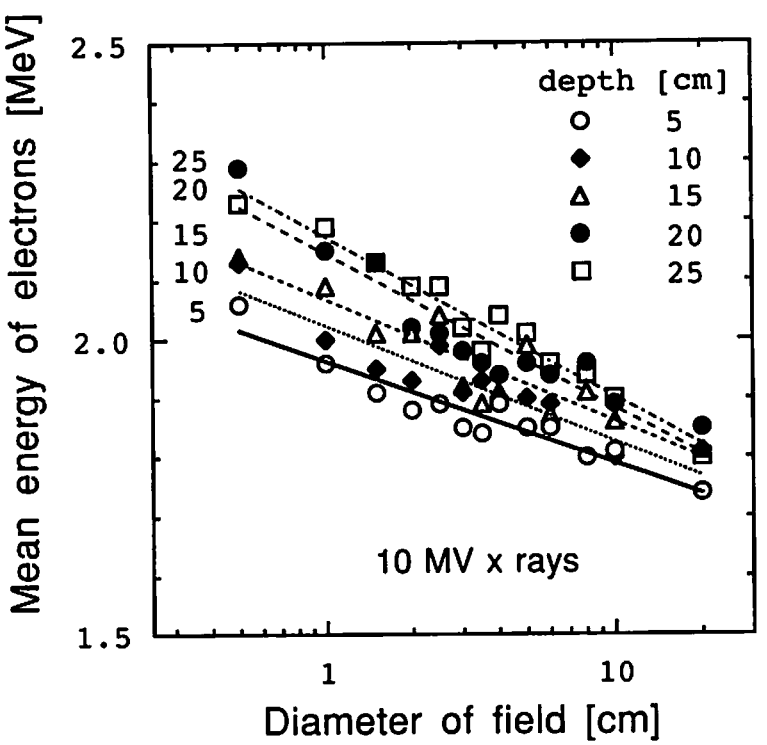

Figure 5 Variation in mean electron energy as a function of field diameter at 5, 10, 15, 20 and 25 cm depths in water for 10 MV x rays.

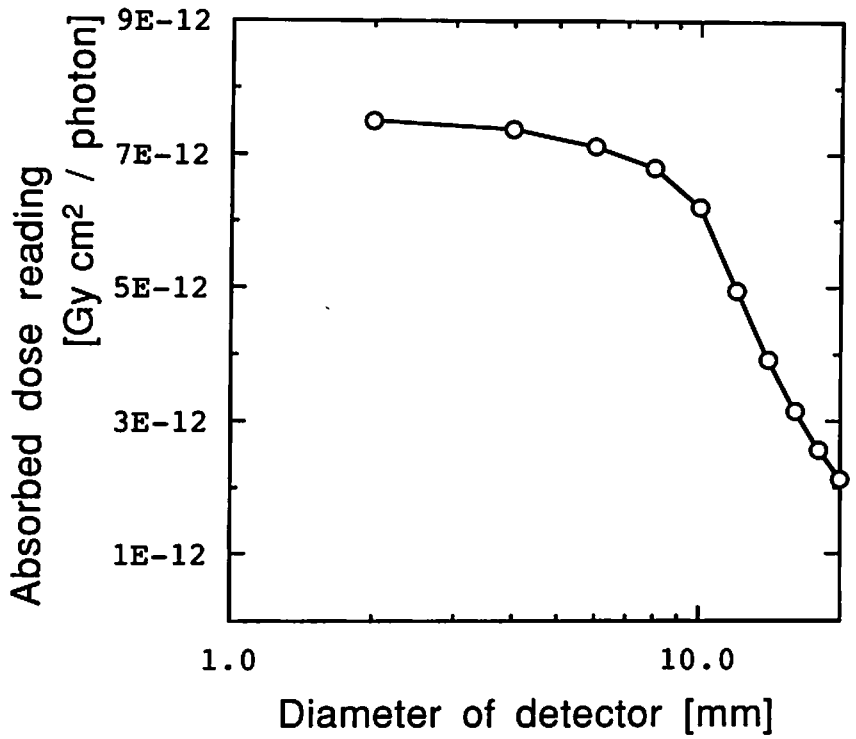

Figure 6 Variation in absorbed dose reading as a function of detector diameter at peak depth for 1.0 cmϕ field of 10 MV x rays.

4 Discussion

4.1 Variation in stopping power ratio

Absorbed dose for radiotherapy is determined in accordance with the AAPM Protocol [10] in the North America and elsewhere, the JARP Protocol [11] in Japan. In these protocols, the absorbed dose measurement using a cavity chamber is recommended. The absorbed dose in water Dw is calculated by

$$D_w = M \cdot N_{gas} \cdot (\bar{L}/\rho)_{w,a} \cdot P \tag{1}$$

where M is the electrometer reading, N_{gas} is the absorbed dose of the cavity gas per unit reading of the electrometer,P is the correction factor for replacement, ion-recombination, etc. $(\bar{L}/\rho)_{w,a}$ is the ratio of the mean restricted mass collision stopping power of water to air. This variable can be determined from the following equation:

$$(\bar{L}/\rho)_{w,a} = \frac{\int_0^{E_{max}} \frac{d\Phi(E)}{dE} \cdot (L(E)/\rho)_w dE}{\int_0^{E_{max}} \frac{d\Phi(E)}{dE} \cdot (L(E)/\rho)_a dE} \tag{2}$$

where $d\Phi(E)/dE$ is the energy spectrum of electrons. Therefore, the energy spectrum is indispensable data for determining stopping power ratio of the absorbed dose calculation. In case of conventional radiotherapy using a broad photon beam, variation in the energy spectrum is so slight that the stopping power ratio is assumed constant. Though the energy spectrum may be varied in a small field, as described above, the constant stopping power ratio is applied for dose determination, without sufficient discussion, in the AAPM Report 54 [12].

To check the validity of such an assumption, the ratio of the mass collision stopping power of water to air and other detector materials were determined using data given in ICRU Report 37

[13]. For an ionization chamber, the c utoff energy of 10 keV was chosen because it is recommended by the dosimetry protocols.

Figure 7 shows the mass collision stopping power ratio as a function of electron energy, and range of the mean electron energy depend on field size and depth. For a diamond detector, the variation in the ratio of the mass collision stopping power of water to carbon is negligible. For an ionization chamber, diode detector and photographic film, the variation in stopping power ratio caused by a variation in the mean energy is less than 1% for 6 MV and 10 MV. It may be stated that the field size and depth dependence of the stopping power is negligible.

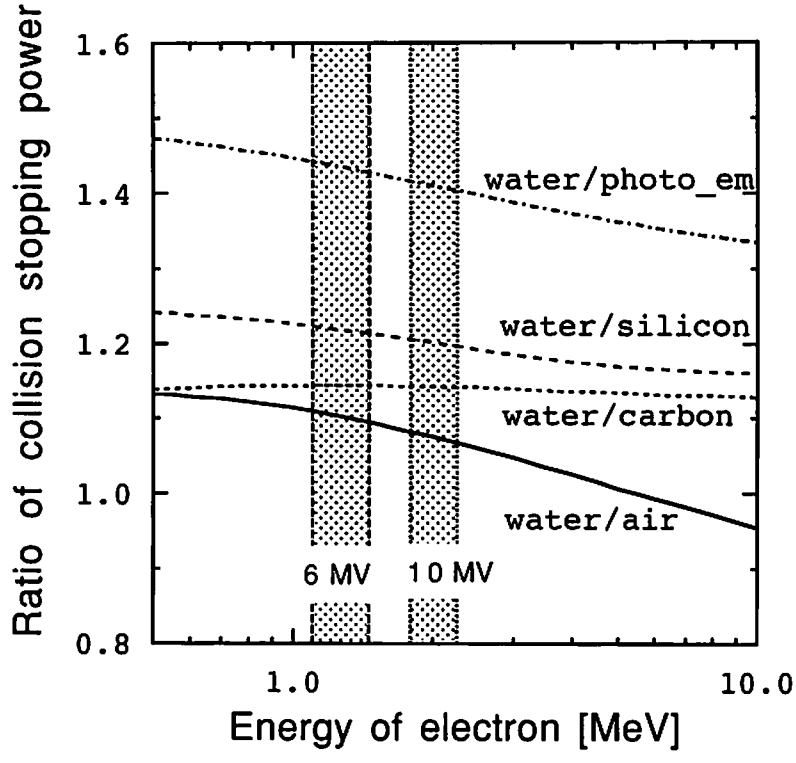

Figure 7 Variation in the mass collision stopping power ratio as a function of electron energy. Shaded zones indicate ranges of the mean electron energy depend on field size and depth for 6 and 10 MV x rays.

4.2 Optimal detector size

In a small field, the absorbed dose reading changed as a function of detector diameter caused by an absence of lateral electronic equilibrium in a sensitive volume. A diamond and/or diode detector, which has a small sensitive volume, is suitable for absorbed dose measurement. Nevertheless, a cavity ionization chamber, which has a relatively large sensitive volume, is recommended for the absolute absorbed dose measurement in the protocols. Therefore, we have to know the maximum size of ionization chamber which has allowable size dependency.

The absorbed dose reading of an ideal 0 diameter detector was calculated by extrapolation. The allowable maximum diameter of a coin shape detector, which has a difference within 2% from an ideal detector, was determined.

Figure 8 shows the variation in the allowable maximum diameter as a function of field diameter for ^{60}Co, 4, 6 and 10 MV. The allowable maximum diameter decreases as field diameter decreases and photon energy increases. In a small field, the allowable maximum diameter is less than 1/3 and 1/4 of field diameter for 4 and 10 MV, respectively.

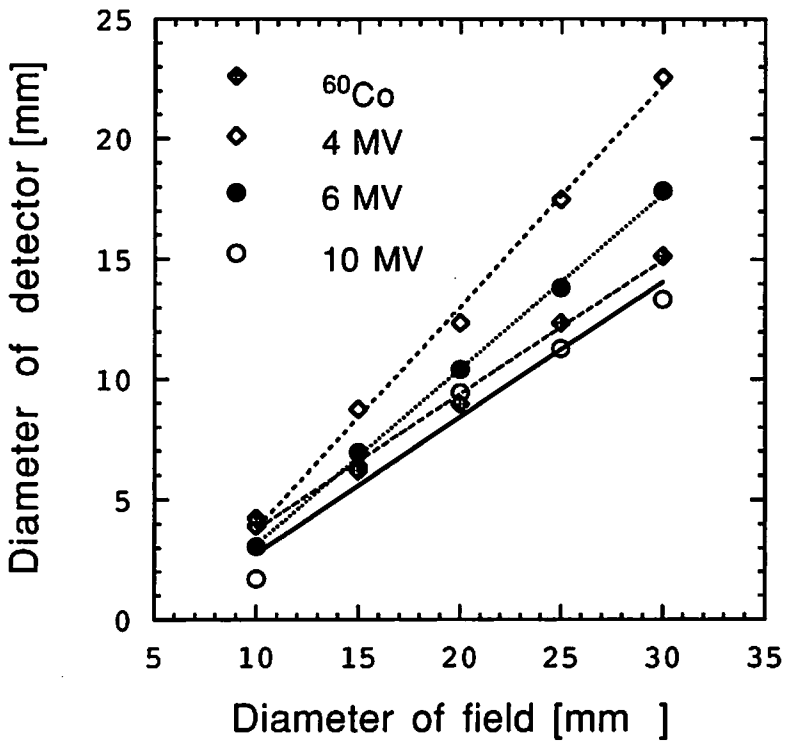

Figure 8 Variation in the allowable maximum diameter as a function of field diameter for ^{60}Co, 4, 6 and 10 MV.

5 Conclusions

The energy spectrum and dose distribution in water were calculated using an EGS4 Monte Carlo simulation.

It is evident that electron and photon energy spectrum changes as a function of field size and depth in water. Nevertheless, it is evident that variation in stopping power ratio caused by a variation in the energy spectrum is less than 1% for an energy range below 10 MV. Consequently, it is confirmed that the $(L/\rho)_w$, a of the AAPM Protocol can be applied to absorbed dose determination for a small field.

In a small field, the absorbed dose reading changes as a function of detector diameter. It is evident that the allowable maximum diameter is less than 1/3 and 1/4 of field diameter for 4 and 10 MV, respectively.

Acknowledgment

This work was partially supported by the Ministry of Education, Science, Sports and Culture, Grant-in-Aid for Scientific Research (C), 11670905, 1999.

References

1) Committee of radiation measurement on Japanese Association of Radiological Physicists: A manual for dosimetry stereotactic radiation surgery beams, *Jpn. J. Med. Phys.*, **Supple. 42**, 1-18, 1994. (in Japanese).

2) A. Wu, R. D. Zwicker, A. M. Lalend et al., "Comments on dose measurements for a narrow beam in radiosurgery", *Med. Phys.* **20**, 777-779, 1993.

3) M. Heydarian, P. W. Hoban and A. H. Beddoe, "A comparison of dosimetry techniques in stereotactic radiosurgery", *Phys. Med. Biol.* **41**, 93-110, 1996.

4) International Atomic Energy Agency, "The use of plane parallel ionization chambers in high energy electron and photon beams: An international code of practice for dosimetry, *Technical Reports Series No.381*, 1997.

5) D. Rogers, B. Faddengon, G. Ding, "BEAM: A Monte Carlo code to simulate radiotherapy treatment units", *Med Phys.* **22**,503-524,1995.

6) W. R. Nelson, H. Hirayama and D. W. O. Rogers, "The EGS4 code system", *SLAC Report-265*, 1985.

7) A. F. Bielajew and D. W. O. Rogers, "PRESTA-The "Parameter Reduced Electron-Step Transport Algorithm" for electron Monte Carlo transport", National Research Council of Canada report *PIRS-0042*, 1987.

8) H. Saitoh, T. Fujisaki, M. Fukushi et al., "Realistic energy spectra of a Cobalt-60 therapeutic beam", *Jpn. J. Med. Phys.* **18**, 341-350, 1999.

9) R. Mohan, C. Chui and L. Lidofsky, "Energy and angular distributions of photons from medical linear accelerators", *Med. Phys.* **12**, 592-597, 1985.

10) AAPM Radiation Therapy Committee Task Group 21, "A protocol for the determination of absorbed dose from high-energy and electron beams", *Med. Phys.* **10**, 741-771, 1983.

11) Japanese Association of Radiological Physicists, "Standard dosimetry for absorbed dose on high-energy photon and electron in radiotherapy", Tsusho Sangyo Kenkyusha, Tokyo, 1986. (in Japanese)

12) AAPM Radiation Therapy Committee Task Group 42, "Stereotactic radiosurgery", *American Institute of Physics*, New York, 1995.

13) International Commission on Radiation Units and Measurements, "Stopping powers for electrons and positrons", *ICRU report 37*, 1984.

CALCULATION OF EFFECTIVE DOSE CONVERSION COEFFICIENTS FOR ELECTRONS FROM 1MeV TO 100GeV

S. TSUDA, A. ENDO, Y. YAMAGUCHI and O. SATO*

Department of Health Physics, Japan Atomic Energy Research Institute (JAERI)
Tokai-mura, Ibaraki-ken, 319-1195, Japan
** Mitsubishi Research Institute, INC.*
2-3-6 Otemachi, Chiyoda-ku, Tokyo, 100-8141, Japan

Abstract

Effective dose and organ dose conversion coefficients for electrons from 1MeV to 100GeV have been calculated using an anthropomorphic phantom and EGS4 for anterior-posterior (AP) and posterior-anterior (PA) geometries. The results were compared with data calculated by FLUKA and MCNP.

1 Introduction

Radiation protection for high-energy radiation, in the energy range up to GeV order, has come to be important with increase of development of high-energy accelerators and space mission. Effective dose, recommended by the International Commission on Radiological Protection (ICRP) in its publication 60 (ICRP60) [1], is used as radiological protection quantities to evaluate radiation risks. Effective doses and organ doses per unit fluence, refered to as the conversion coefficients, have been calculated against external radiation as the quantity to transform a measured fluence to effective dose and organ dose. The conversion coefficients have been calculated up to 10GeV for photons [2], [3] and up to 10TeV for neutrons [4]. The conversion coefficients for electron, however, are not enough to cover the high-energy range. ICRP74 presented them from 1MeV to 10MeV [5] but the irradiation geometry and the kind of organ doses presented are limited. Sawamura [6] calculated the conversion coefficients up to 400MeV using EGS4 [7]. The data available over 400MeV are those presented by Ferrari et al. They calculated the conversion coefficients from 5MeV up to 10GeV [8] using FLUKA. However, the data should be checked independently, since FLUKA is not opened to the public.

In the present study, we calculated the fluence to effective dose and organ dose conversion coefficients for electrons from 1MeV to 100GeV, using the photon electron Monte Carlo simulation code EGS4 and an anthropomorphic phantom.

2 Method of calculation

2.1 Effective dose

Effective dose, recommended by ICRP60, is defined as

$$E = \sum_T w_T H_T, \tag{1}$$

where w_T is the tissue weighting factor for tissue or organ, T, and H_T is the equivalent dose in tissue or organ, T. The tissue weighting factors are given for 12 tissues or organs and remainder which includes 10 tissues or organs.

H_T is given by

$$H_T = \sum_R w_R D_{T,R}, \tag{2}$$

where w_R is the radiation weighting factor for radiation R and $D_{T,R}$ is absorbed dose for tissue or organ, T, due to radiation R. For photons and electrons, w_R is defined to be 1. $D_{T,R}$ is the absorbed dose averaged over the tissue or organ, T, due to radiation R.

2.2 Mathematical phantom and Monte Carlo code

An anthropomorphic phantom and EGS4 were used to calculate $D_{T,R}$ for each tissue or organ. Figure 1 shows the anthropomorphic phantom, an improved version of MIRD phantom [9]. The phantom, designed as a western male, is 174cm in height and 71.1kg in weight. To incorporate the phantom into the EGS4 code ststem, the generalized user code for EGS4, UCGEN [10], was used. The user code employs modified MARS geometry package [11] developed at ORNL, and the MIRD-type anthropomorphic phantom was presented with this geometry package.

Cut off energies for photons and electrons were set to be 10keV and 100keV respectively, whose range are short as compared with the tissue or organ size in the phantom. A large number of histories were selected to keep the statistical uncertainties for most of organ or tissue equivalent doses below 10%. Ovaries had the largest statistical uncertainties especially for incident energy lower than 10MeV though they were within 15%.

The phantom was irradiated in a vacuum space by mono-energetic parallel electron beams. The directions of incidence of the beams were anterior-posterior (AP) and posterior-anterior (PA).

3 Results and Discussion

Table 1 summarizes phantom types and radiation transport codes used in other studies. The phantom used in this study is hermaphroditic. Ferrari et al. [12] used an hermaphroditic phantom derived from ADAM, developed by GSF and translated into the FLUKA code geometry.

Figure 2 shows the effective dose conversion coefficients in AP geometry. The coefficients increase with incident electron energy up to 50MeV and become almost constant for electron energies over 50MeV. This is because the range of 50MeV electron is over the anterior-posterior thickness of the phantom.

Figure3 shows the conversion coefficients for the gonads equivalent dose in AP geometry vs. incident electron energy. Equivalent doses to both gonads and ovaries are plotted for comparison with other results. The gonads equivalent dose in this calculation has been evaluated as the mass-weighted mean of both male and female gonads equivalent dose. In the energy range below 10MeV, the contribution of ovaries to gonads equivalent dose were found to be a few percent, whereas the fraction can reach 9.4% at 10MeV. For the energies greater than 50MeV, the gonads equivalent doses show a small increase with incident electron energy.

In the energy range from 1MeV to 10MeV, effective doses calculated by Sawamura [6] are smaller than the other results in Fig.2. A possible reason is that Sawamura calculates the gonads equivalent dose as female organ equivalent dose as shown in Fig.3. The method of evaluation of tissue or organ equivalent dose can vary among such tissue or organ as red bone marrow, bone surface, muscle and gonads. In the case of gonads equivalent dose, Ferrari et al. [8] adopted the arithmetic mean of the doses, though no significant difference between our values can be seen in Fig.3. On the other hand, the value of ICRP74 is in good agreement with our values only at 1MeV in the energy range.

Figure 4 shows the fractions of $w_T H_T$, equivalent dose (H_T) multiplied by the tissue weighting factor (w_T), contributing to effective dose in AP geometry. In the energy range below 3MeV,the components of effective dose are almost dominated by $w_T H_T$ for gonads, breast and skin. This is because these tissue are not only located near the surface of the phantom but also have comparatively large tissue weighting factors. At energies greater than 50MeV, each fraction of $w_T H_T$ for tissue or organ contributing to effective dose are independent on electron energy and become asymptotic to each weighting factors as shown at the bar graph. The reason comes from the relation between the electron range at energies above 50MeV and the thickness of the phantom, as discussed about Fig.2 and Fig.3 in this section.

The comparison of effective dose for AP and PA geometries is shown in Fig.5. The effective dose for AP geometry is higher than that for PA in the energy range over 100MeV, mainly due to the larger doses received by gonads and breast. In the energies greater than 100MeV, the effective doses are roughly constant though the effective dose for PA geometry is slightly larger than the AP ones. The difference at 100GeV can reach 28.5% (the effective dose for PA geometry relative to that for AP geometry).

As a summary of this section, effective doses in the energy range greater than 100MeV were found to be about 20% less than the values calculated FLUKA as seen in Fig.2. One possible reason is attributed to a result of the accumulation of each small difference in organ doses. Another explanation is that the difference in the energy range over 10MeV may result from the photonuclear reaction which has been considered by FLUKA.

It is reported that charged particles produced by the photonuclear reaction contribute to equivalent dose because of their large averaged quality factors [13]. Considering the definition of the radiation weighting factor, the quality factor must be used to evaluate the doses for charged particles.

4 Conclusion

Effective doses and organ doses per unit fluence for electrons have been calculated from 1MeV to 100GeV using the photon-electron Monte Carlo simulation code, EGS4, combined with an anthropomorphic phantom. The results could verify the conversion coefficients for electrons up to 10GeV calculated by FLUKA and suggest that the methods for calculation such as a phantom used and simulation code cause no significant difference in the effective doses and organ doses.

We will make a set of database for conversion coefficients for electrons up to 100GeV. The first is to calculate the conversion coefficients for other geometries such as right lateral (RLAT), left lateral (LLAT), isotropic (ISO) and rotational (ROT). The second is to evaluate the photonuclear reaction at energies greater than about 10MeV, whereas it was not treated in the calculations.

Table.1 Character of Phantoms and radiation transport codes employed.

	Phantom's type	Phantom's sex	Code	Energy range
Present	MIRD phantom†	Hermaphrodite	EGS4	1MeV~100GeV
ICRP Publ. 74 [5]	ADAM	Male	MCNP ver.4	0.1~10MeV
Sawamura et al. [6]	MIRD phantom‡	Hermaphrodite	EGS4	0.1~400MeV
Ferrari et al. [8]	ADAM	Hermaphrodite	FLUKA	5MeV~10GeV

† Improved version of MIRD phantom. The height of the breast model was changed to about half of the Christy phantom model for making it a hermaphroditic phantom.

‡ Improved version of MIRD phantom.

References

1) International Commission on Radiological Protection. ICRP Publication 60 (Oxford: Pergamon Press) (1991).

2) O. Sato, et al. Radiat. Prot. Dosim. **62**, 119-130 (1995).

3) A. Ferrari, M. Pellicioni, et al. Radiat. Prot. Dosim. **67**, 245-251 (1996).

4) A. Ferrari, et al. Radiat. Prot. Dosim. **71**, 165-173 (1997).

5) International Commission on Radiological Protection. ICRP Publication 74 (Oxford: Pergamon Press) (1998).

6) S. Sawamura. JAERI Conf-95-007, 94-102 (1995).

7) W.R. Nelson, H. Hirayama and D.W.O. Rogers. SLAC-265 (1985).

8) A. Ferrari, M. Pellicioni, et al. Radiat. Prot. Dosim. **69**, 97-104 (1997).

9) Y. Yamaguchi. J. Nucl. Sci. Tech. **31**, 716-725 (1994).

10) T. Momose, et al. Proceedings of 1st EGS4 User's Meeting in Japan, 48-73 (1990).

11) J.T.West and M.B.Emmett. NUREG/CR-0200, vol.3, sect.M9 (1993)

12) M. Pellicioni, M. Pillon Radiat. Prot. Dosim. **67**, 253-256 (1996).

13) O. Sato. doctoral dissertation, Tohoku University (1999)

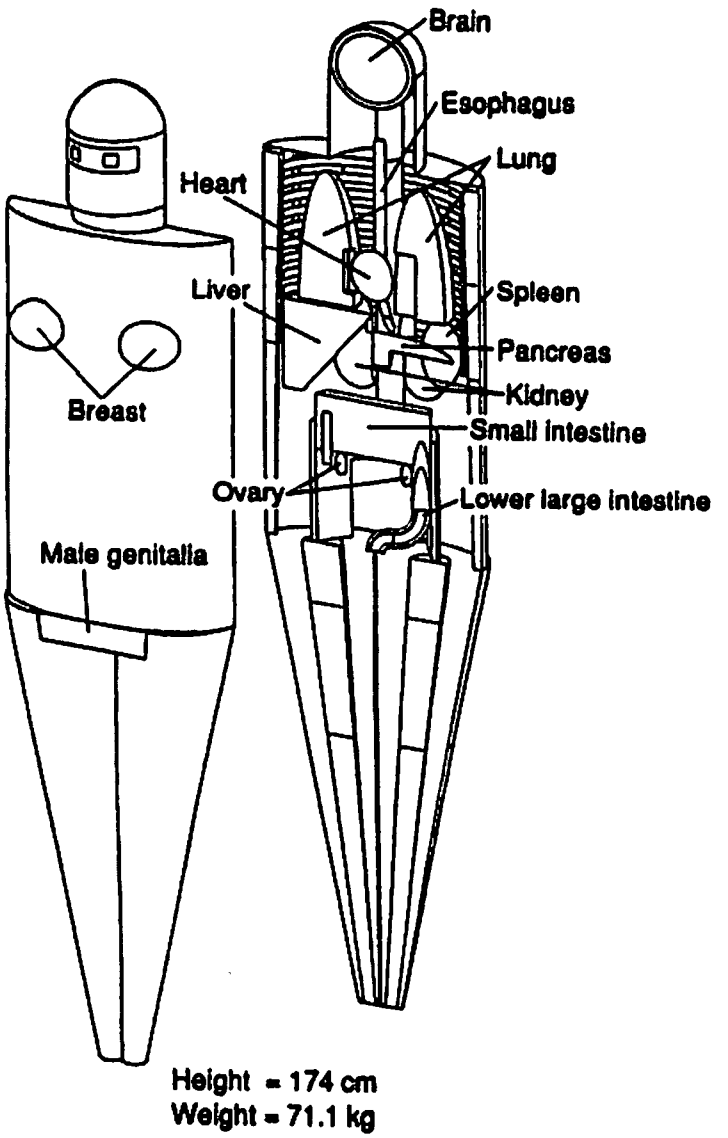

Fig.1 Schematic representation of phantom used in calculation.

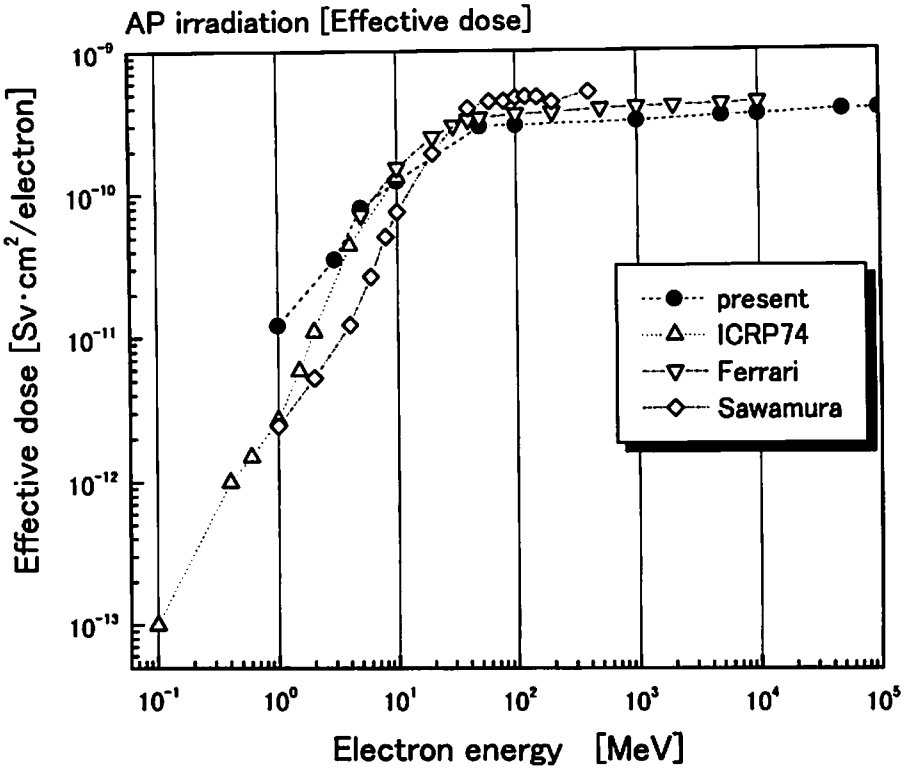

Fig.2 Effective dose per unit fluence as a function of incident electron energy.

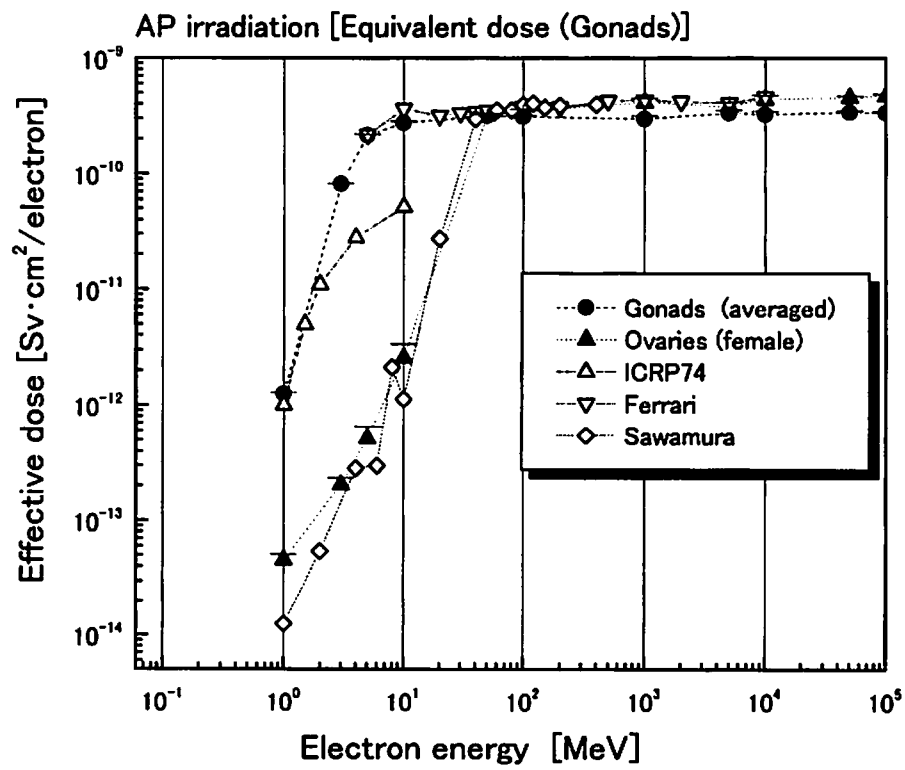

Fig.3 Gonads equivalent dose per unit fluence as a function of incident electron energy.

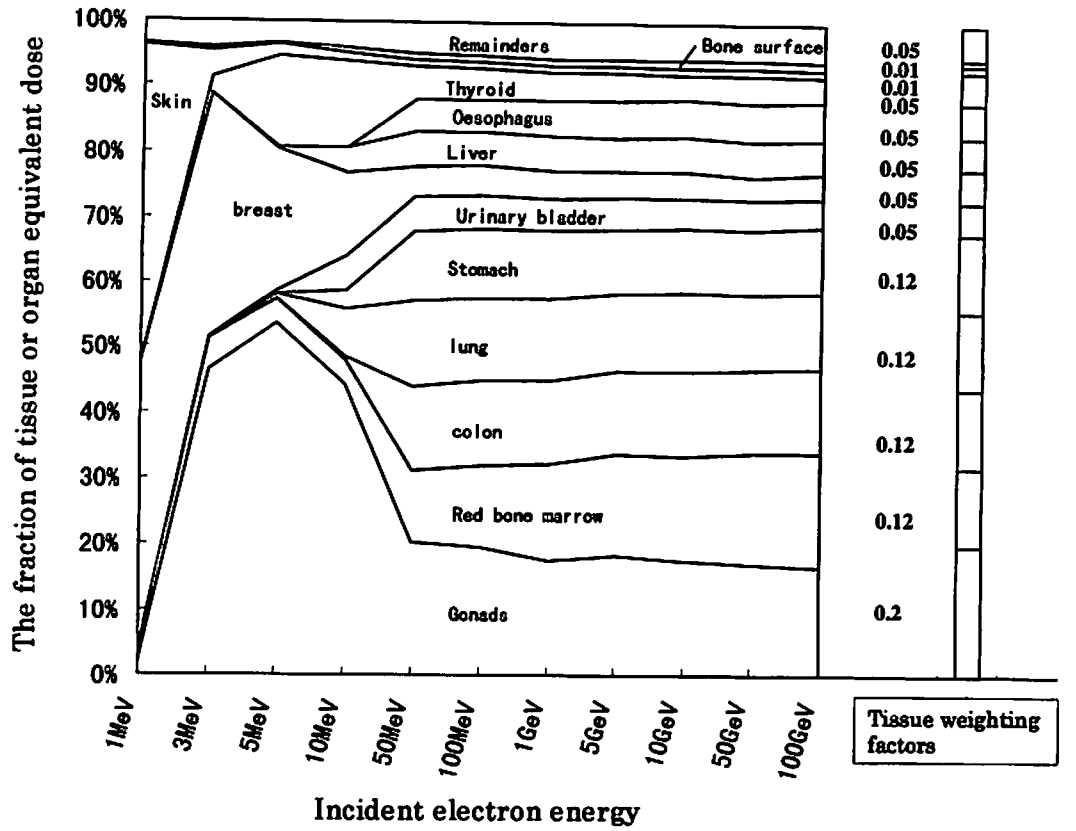

Fig.4 The fractions of equivalent dose (H_T) multiplied by the tissue weighting factor (w_T), $w_T H_T$, contributing to effective dose in AP geometry.

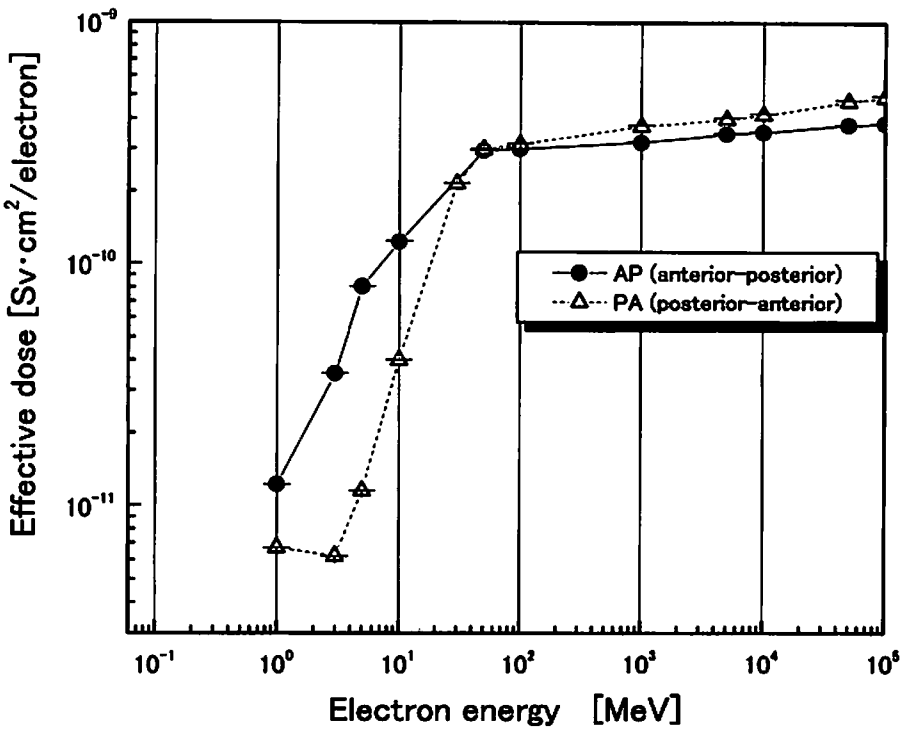

Fig.5 The comparison of effective dose between anterior-posterior (AP) and posterior-anterior (PA) geometry.

INFLUENCE OF SECONDARY ELECTRONS PRODUCED IN IRON OR LEAD SHIELD IRRADIATED WITH GAMMA AND X RAYS TO SKIN DOSE

N. NARIYAMA

Nuclear Technology Division, Ship Research Institute
6-38-1, Shinkawa, Mitaka, Tokyo 181-0004, Japan

Abstract

Secondary electrons from high-Z material shield irradiated with photons possibly influence skin dose. To confirm the quantitative relation with 1-cm dose equivalent and necessary distance from the shield for neglecting the effect, energy deposition at the depth of 70 μm in a phantom was calculated behind iron or lead shield with 1-3 mfp thickness irradiated with 0.1-1.0 MeV photons. For iron, while the factor of the dose enhancement at the surface of the shield was 50observed just 5 cm from the shield. For lead, the factors rose to 2.5, 4.7 and 2.5 for 0.5, 0.2 and 0.1 MeV photons, respectively, and the influence was observed until 80, 60 and 5 cm for each energy. It was confirmed that even the enhanced 70-μm dose equivalent was smaller than the values 10 times as large as 1-cm dose equivalent for all the photon energies. The enhancement, however, will increase effective dose by about 4case of lead shield for 0.2 MeV photons.

1 Introduction

From iron and lead shields irradiated with gamma or X rays, a large number of secondary electrons generated are ejected. The electrons cannot reach at the 1-cm depth, but easily at 70-μm depth above an energy: the electrons influence skin dose in the vicinity of the shield. The standard of radiation shielding safety, however, is determined from 1-cm dose equivalent and 70-μm dose equivalent is estimated only if the value can overpass a value ten times as large as 1-cm dose equivalent. In fact, without shielding and in the electric equilibrium condition even behind the shield, the condition is not satisfied above 10 keV [1-3]. Nevertheless, in the vicinity of the shield the relation is not clear while the influence of the electrons has been assumed small enough.

In the ICRP 60 Recommendations [4], skin dose is incorporated into the effective dose. Moreover, first of all, unnecessary exposure should be avoided. Accordingly, even if 70-μm dose equivalent is negligible for shield design and individual dose monitoring, skin dose near the shield surface and distance necessary for neglecting the effect is to be estimated.

In this study, energy deposition at 70-μm depth in ICRU 4-element slab phantom behind iron or lead shield irradiated with 0.1 to 1.0 MeV photons was calculated using EGS4 [5] with variable shield thickness and distance between the shield and the phantom. The values were compared with 1-cm dose equivalent and effective dose.

2 Calculation Method

For the calculations, ICRU 4-element slab phantom of 15-cm thickness was placed behind iron or lead shield, and irradiated with plane parallel-beam photons. The atomic constituents of the phantom are 10.1% H, 11.1% C, 2.6% N and 76.2% O by weight, and the density is 1.0 g/cm^3. For 70-μm dose equivalent, energy deposited in the interval of 50-100-μm depth in the phantom was calculated. The photon energy used was 0.1, 0.2, 0.5 and 1 MeV, and the thickness of the shield 1, 2 and 3 mfp. The distance between the shield and the phantom slab was changed from 0 to 200 cm. In the EGS4 calculations, the cut-off energy used was 1 keV for photons and 10 keV for electrons, and fluorescent photons and photoelectrons from K- and L-shells were considered [6].

3 Result

Figure 1 shows the energy deposited at 70-μm depth behind iron shield of 1-mfp thickness. The statistic errors are below 6%. For 0.5 and 1 MeV photons, the values are constant even if the phantom is attached with the shield. On the other hand, for 0.2 and 0.1 MeV photons, the dose is enhanced by 40 and 50% at the surface of the shield, and the distance for electric equilibrium condition is 10 and 5 cm, respectively. Figures 2 and 3 show the results for 2- and 3-mfp thickness. The tendency is almost the same as that in Fig. 1, while the distance for electric equilibrium condition differs somewhat.

The result for lead of 1-mfp thickness is indicated in Fig. 4. The degree of the dose enhancement at the shield surface is larger than for iron: 1.06 at 1.0 MeV, 2.5 at 0.5 MeV, 4.7 at 0.2 MeV and 2.5 at 0.1 MeV. Moreover, the distance needed for electric equilibrium condition is 80 cm at 0.5 and 0.2 MeV, and 5 cm at 0.1 MeV. Figures 5 and 6 show the results for 2- and 3-mfp thickness. The degree of the dose enhancement for 2 mfp is 2.0, 4.6 and 2.5 at 0.5, 0.2 and 0.1 MeV; for 3 mfp 2.25, 4.8 and 2.2. In both figures, the distance attaining electric equilibrium condition was almost the same as for 1 mfp.

4 Discussion

From Figs. 1 to 6, it was found that the increase of the dose by the shield and the distance to attain the electric equilibrium condition did not depend largely on the shield thickness. Moreover, the influence of iron shield is negligible as long as the skin is not attached to the shield. On the other hand, for lead shield the influence continues to be remarkable until several tens cm for 0.5 to 0.2 MeV photons.

For 1.0 MeV photons, outstanding increase at the surface of the shield has not been observed even for lead. To clarify the cause, transmitted electron spectra from lead shield and the ICRU phantom were calculated for 1 and 0.5 MeV photons. The results are indicated in Figs. 7 and 8 for 1-mfp thickness. In Fig. 7, the spectra for lead are shifted to higher energy but the integral area does not differ from that for the ICRU phantom. On the other hand, in Fig. 8 the area for lead becomes larger than that for the phantom. That is, the integral number of the electrons made difference between 1.0 and 0.5 MeV photons.

To confirm that 70-μm dose equivalent does not exceed the dose 10 times as large as 1-cm dose equivalent even if the skin becomes in touch with the lead shield, 1- cm dose equivalent were calculated using an empirical expression. In the method, linear attenuation coefficients, exposure buildup factors for plane normal incidence [7], and effective conversion factors [2,3] were used. The result is shown in Table 1. For 0.3 to 0.1 MeV photons, the values were calculated with EGS4 since exposure buildup factors for plane geometry are not tabulated in the reference [7]. The doses ten times as large as the 1-cm doses equivalent are larger compared to 70-μm dose equivalent in any

case. That is, 70-μm dose equivalent is negligible for shield design calculation and individual dose monitoring.

Skin dose is incorporated into effective dose with the tissue weighting factor of 0.01. In the energy region over 0.1 MeV, the contribution of skin dose to effective dose is 1% in AP, PA and ROT irradiation geometry [8]. Consequently, 4.7 times increase of skin dose behind lead for 0.2 MeV photons makes the effective dose larger by 3.7% assuming that all the front-side skin is attached to the shield. For the other energy, the increment is smaller.

5 Conclusion

The values of 70-μm dose equivalent have been found to be negligible for individual dose monitoring and shielding design even behind a lead shield. The secondary electrons, however, enhance the skin dose by a factor of 4.7 for 0.2 MeV photons and the effective dose by 4% at most. For the influence, slab geometry used is a safer-side condition compared to sphere geometry.

When the phantom is in front of the shield, the electron influence will be given to the backside of the phantom. However, the 70-μm dose equivalent on the back is considered smaller than the value ten times as large as 1-cm dose equivalent because the photons attenuate in the phantom and electrons ejected backward are smaller than those ejected forward in the energy region.

While in practice personnel wear clothes and will not keep in touch with the shield for a long time, the influence is worth keeping in mind.

References

1) International Commission on Radiological Protection, ICRP51 Pergamon Press (1987).

2) S. Tanaka and T. Suzuki, *ORNL/TR-90/29* (1991).

3) "Practical manual for γ(x)-ray shield calculations for radiation facility," ed. T. Hamada, Nuclear Safety Technique Center (1989) (in Japanese).

4) International Commission on Radiological Protection, ICRP60, Pergamon Press (1991).

5) W. R. Nelson, H. Hirayama and D. W. O. Rogers, *SLAC-265* (1985).

6) H. Hirayama et al., *KEK Internal 96-10* (1996).

7) S. Tanaka and K. Takeuchi, *JAERI-M 84-018* (1984).

8) International Commission on Radiation Units and Measurements, ICRU Report 57 (1998).

Table 1 Comparison of 70-μm and 1-cm dose equivalent just behind 1-mfp thick lead shield

Energy (MeV)	70-μm dose equivalent (MeV cm^2/g)	1-cm dose equivalent (MeV cm^2/g)
1.0	1.93e-2	1.61e-2
0.5	2.01e-2	8.10e-3
0.3	2.14e-2	5.31e-3
0.2	1.56e-2	3.58e-3
0.15	9.54e-3	2.91e-3
0.1	5.78e-3	2.43e-3

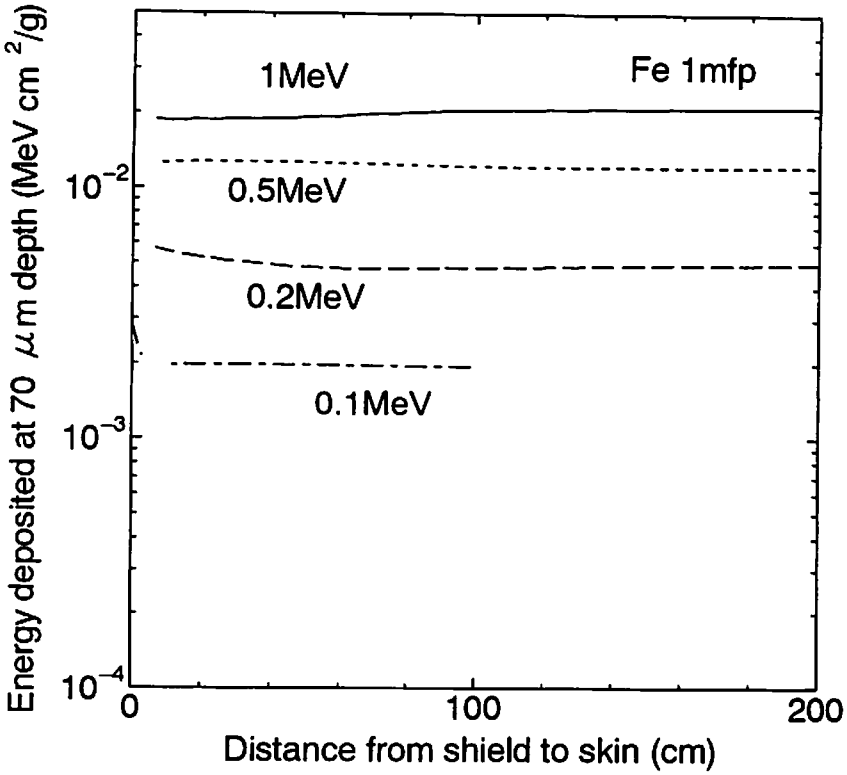

Fig.1 Energy deposition at 70μm depth in ICRU 4-element slab phantom for 1-mfp thick iron shield

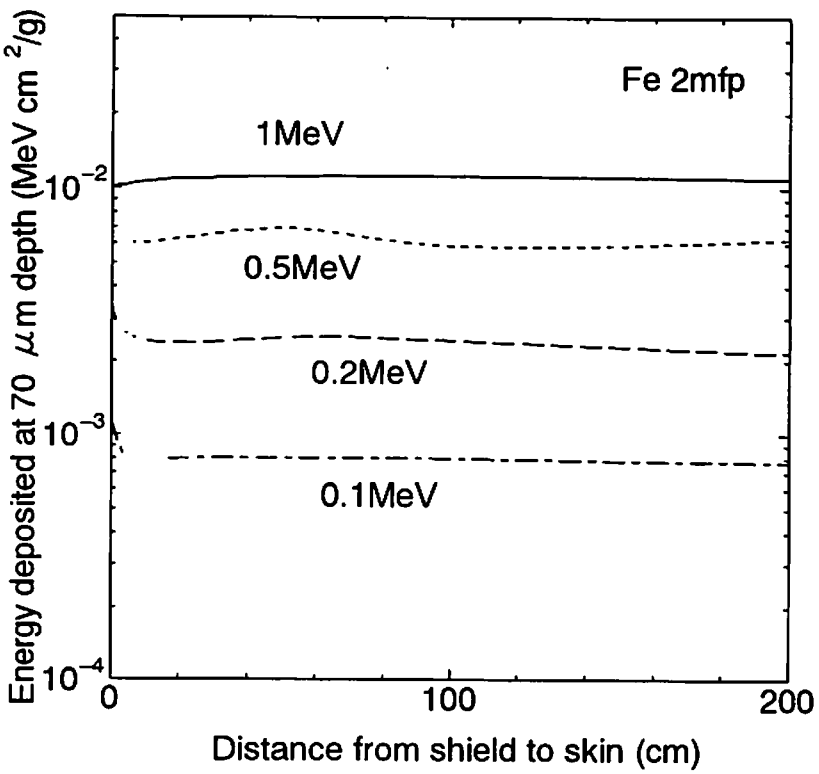

Fig.2 Energy deposition at 70μm depth for 2-mfp thick iron shield

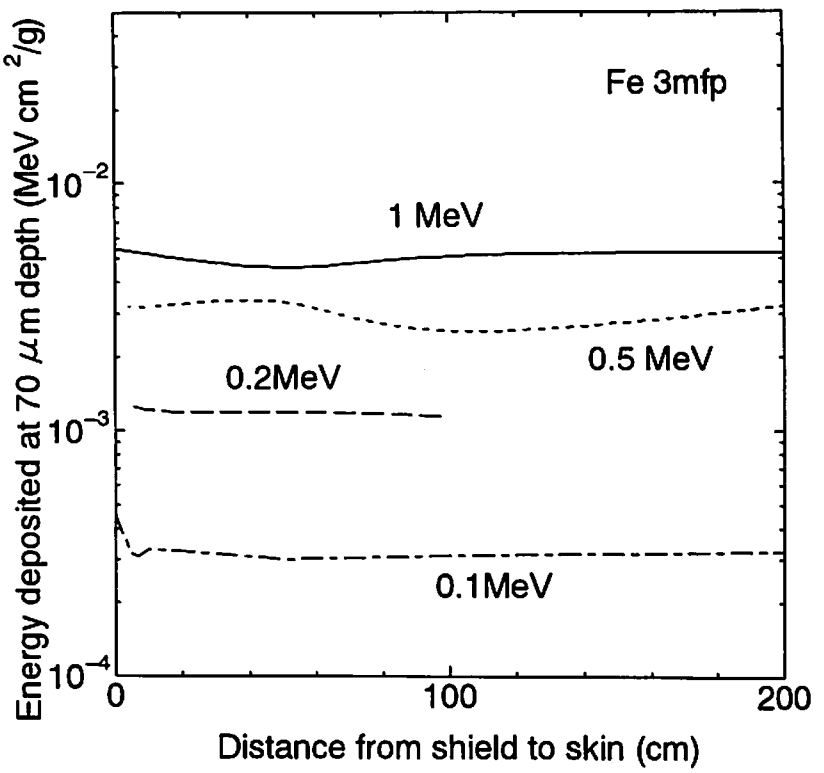

Fig.3 Energy deposition at 70μm depth for 3-mfp thick iron shield

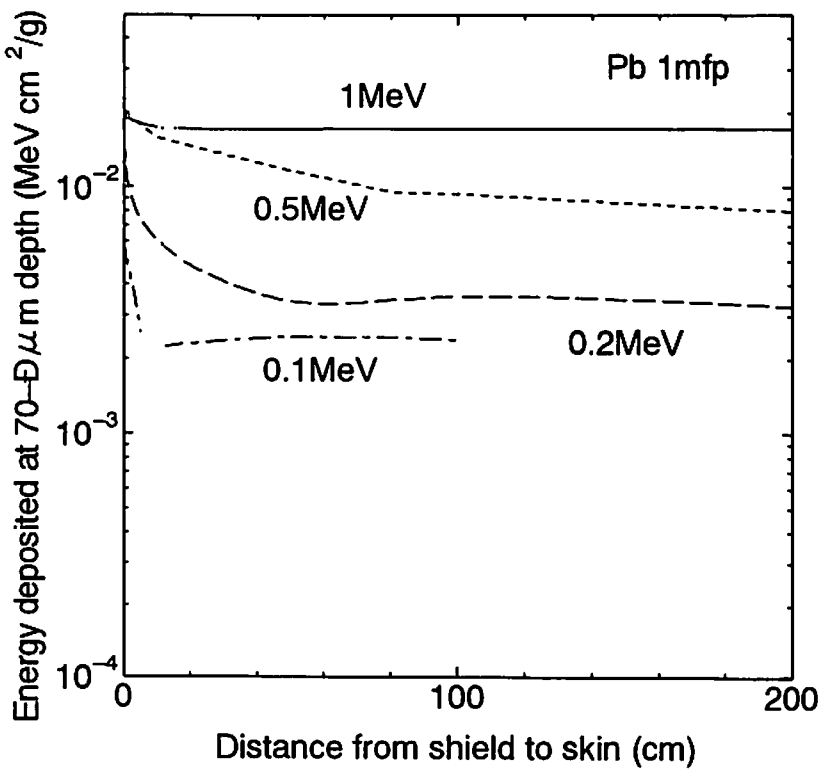

Fig.4 Energy deposition at 70μm depth for 1-mfp thick lead shield

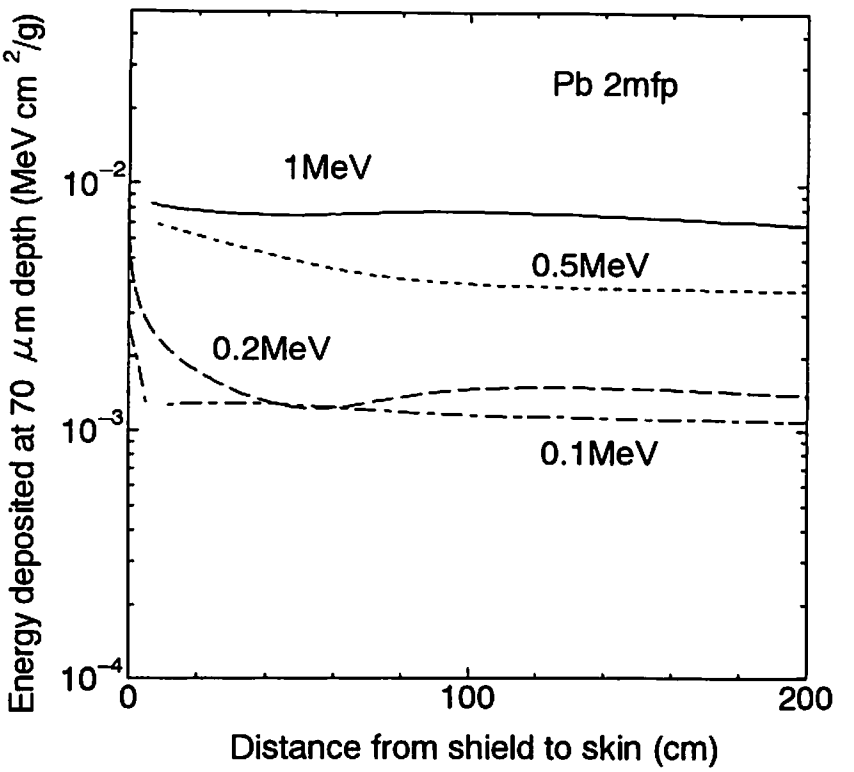

Fig.5 Energy deposition at 70μm depth for 2-mfp thick lead shield

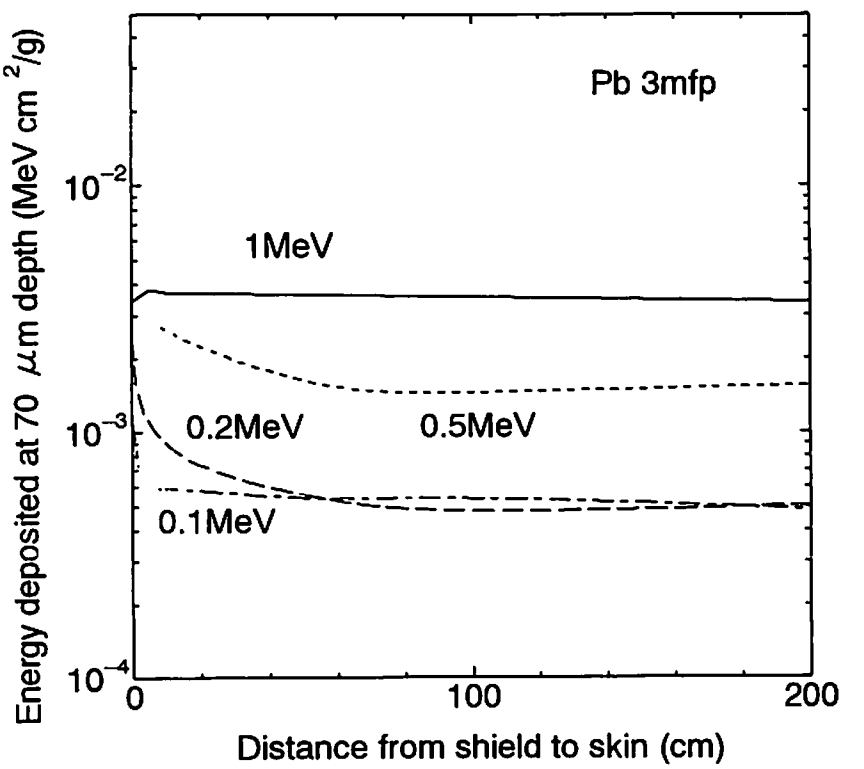

Fig.6 Energy deposition at 70μm depth for 3-mfp thick lead shield

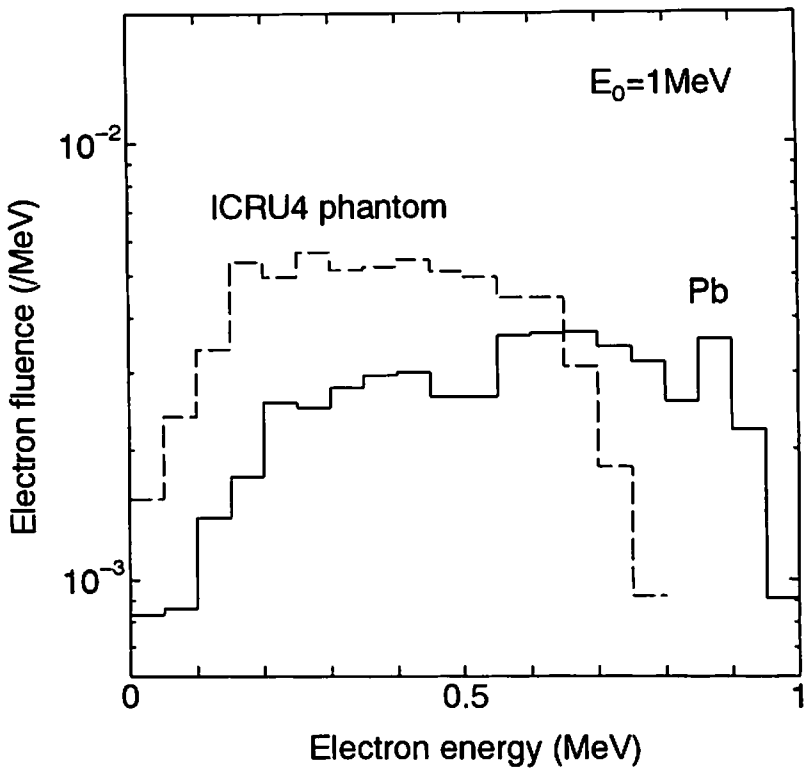

Fig.7 Electron spectra for 1-mfp thick lead shield irradiated with 1.0 MeV photons

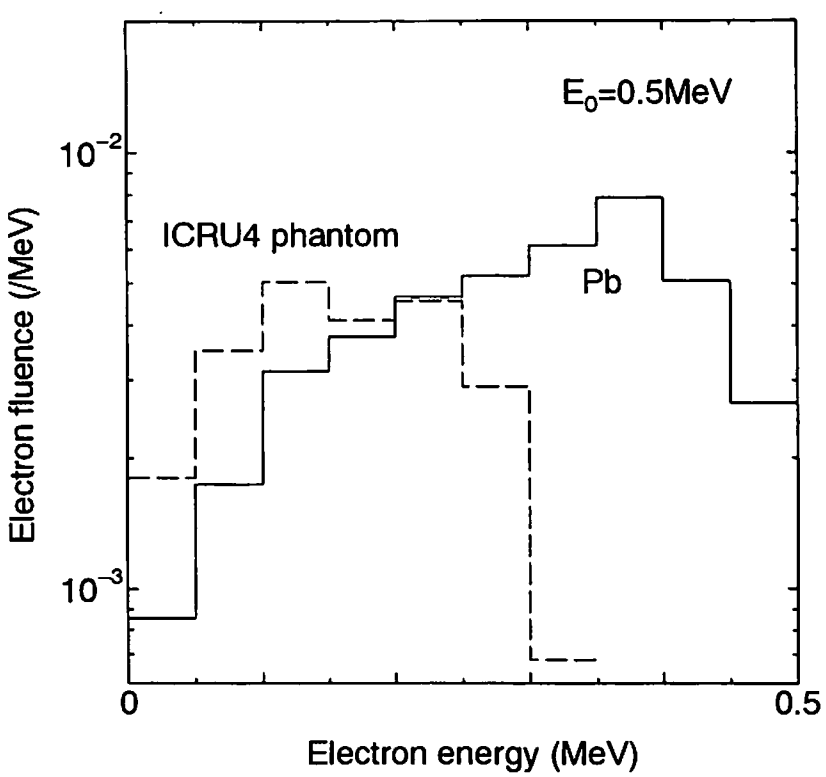

Fig.8 Electron spectra for 1-mfp thick lead shield irradiated with 0.5 MeV photons

ENERGY SPECTRA OF PHOTONS GENERATED FROM THE TA TARGET IRRADIATED BY ELECTRONS

H. SAGAWA and I. URABE

Faculty of Engineering, Fukuyama University
Gakuen-cho 1, Fukuyama-shi, Hiroshima, 729-0292, Japan

Abstract

The energy spectrum of photons generated from a tantalum irradiated by electrons varies depending on the thickness of the target, the electron energy and the direction of the photons generated. In order to estimate the performance of the KUR LINAC as a neutrons generator and the safety level of the working space, the energy spectra of photons were calculated using the EGS4 Monte Carlo Code. The angular distribution of the emitted photons was also obtained. As the energy of the incident electrons became higher, the intensive photons were observed in the direction of the 0 radian (the direction of the beam line). When the tantalum target was 1mm in thickness, the photons observed in the direction of the $\pi/4$ radian became intensive, as the electron energy was lower.

1 Introduction

The many kind of radiations was generated at the high energy Linac facility. The intensity and the energy of radiation were different at the each position in the experimental room. The information of the kind, the energy and the directional distribution at the working place must be known in order to protect workers from the radiation exposure. The spectra of photons and the directional distribution at the working place were calculated to obtain the information for the health physics.

2 Calculation Model

The energy spectra of photons generated from the tantalum target by irradiating mono-energy electrons were calculated. The arrangement of the tantalum target and the detector used for the calculation of the photons spectra was shown in Fig.1. The electron energy was varied from 10MeV to 100MeV. The tantalum target was a cylinder of 5.0cm in diameter. The thickness of tantalum target was varied from 1mm to 10mm. The direction of 0 radian was defined in the direction of the electron irradiation. The position of the detector was varied to make the angle of 0 radian, $\pi/4$ radian and $\pi/2$ radian.

The geometrical model used for the calculation of the photons detected in the direction of the 0 radian was shown in Fig.2. The boundary was fixed by two cylinder surfaces and four plane surfaces. The regions divided by the boundary were numbered from 1 to 9. The region 2 was a tantalum target. The region 6 and the region 7 were the air detector. The others were the gap. The thickness (T1) of tantalum was chosen as 1mm, 3mm, 5mm and 10mm. The distance (T2)

of the tantalum target and the detector was 1m. The thickness (T3) of detector was 10cm. The radius (R1) of tantalum target was 2.5cm. R2 was 2.5cm so that the radius of the detector was 5cm. The electrons were irradiated from the top of the region 2. The electron energy was varied 10MeV, 30MeV, 60MeV and 100MeV. The spectra of photons generated from tantalum target were calculated at each state.

The geometrical model used for the calculation of the photons detected in the direction of the $\pi/4$ radian was shown in Fig.3. The boundary was fixed by three cylinder surfaces and four plane surfaces. The regions divided by the boundary were numbered from 1 to 12. The region 2 was a tantalum target. The region 10 was the detector. The others were the gap. The radius (R1) of the tantalum target was 2.5cm. T2 and R2 were 67cm so that the distance of the tantalum target and the detector became 1m. T3 and R3 were 7cm so that the width of the detector became 10cm. The thickness (T1) of the tantalum target, the electron energy and the irradiation position were the same as the former calculation.

The geometrical model used for the calculation of the photons detected in the direction of the $\pi/2$ radian was shown in Fig.4. The boundary was fixed by three cylinder surfaces and four plane surfaces. The region 5 was a tantalum target. The region 4, 7 and 10 were the detector. The others were the gap. The thickness (T2) of the tantalum target was the same as T1 of the former calculation. The radius of the tantalum target (R1) was 2.5cm. The distance (R2) of the tantalum target and the detector was 1m. T1 and T3 were varied (100-T2)/2mm so that the width of the detector became 10cm. The thickness (R3) of the detector was 10cm. The electron energy and the irradiation position were the same as the former calculation.

3 Results and Discussion

The energy spectra of photons observed by the 1mm thick tantalum in the direction of the 0 radian were shown in Fig.5. The horizontal axis shows the energy of photons, the vertical axis shows the flux density of photons (electron-1 cm-2 MeV-1). The lines indicate the spectra of photons generated at the electron energy of 10MeV, 30MeV, 60MeV and 100MeV. The amount of observed photons increases with increasing the electron energy. The higher intensity of photons was observed in the lower energy region.

The energy spectra observed by the 10mm thick tantalum in the direction of the 0 radian were shown in Fig.6. The more intensive photons were observed by the higher energy electrons. Although the energy spectra of photons were similar to that observed by the thin tantalum, the photons spectra at the 1MeV were different from the photons spectra observed by the thin tantalum. The ratios of the photons spectra observed by the 10mm thick tantalum to that observed by the 1mm thick tantalum were calculated to compare the difference of each spectra.

The ratios of the photons spectra observed by the 10mm thick tantalum to that observed by the 1mm thick tantalum were shown in Fig.7. The horizontal axis shows the energy of photons, the vertical axis shows the ratio of the photons spectra observed by the 10mm thick tantalum to that observed by the 1mm thick tantalum. Since the more intensive photons were absorbed in the case of the thick tantalum, the ratios of the photons spectra in figure were less than one in the range of all energy. Since the many photons at the energy above 10MeV decrease due to scatter, the ratios of photons spectra in the energy range between 2MeV and 10MeV were higher than that at the energy above 10MeV. Although the many photons in the range between 2MeV and 10MeV decrease due to scattering and the absorption, the photons increase due to production by the scattering of photons above 10MeV. Since the photons below 1MeV were absorbed by the thick tantalum very much, the ratios at the 1MeV were very small.

The ratios of the photons spectra observed by the 3mm thick tantalum to that observed by the 1mm thick tantalum were shown in Fig.8. The ratios at the electron energy of 60MeV and 100MeV were more than one in the photon energy range of interest, because the scattered photons were

more intensive than the absorbed ones. The thickness of tantalum target could be decided so as to get the most intensive photons.

The energy spectra observed by the 10mm thick tantalum in the direction of the $\pi/4$ radian were shown in Fig.9. The horizontal axis shows the energy of photons, the vertical axis shows the flux density of photons. The amount of observed photons increases with increasing the electron energy. The higher intensity photons were observed in the lower energy region. The photons in the direction of the $\pi/4$ radian were less than that in the direction of the 0 radian.

The spectra of photons observed by the 1mm thick tantalum in the direction of the $\pi/4$ radian were shown in Fig.10. The higher intensity photons were observed in the lower energy region. The 1mm thick tantalum was not enough to generate the photons in the direction of the $\pi/4$ radian.

In order to estimate the performance as the neutron generator, the totals of photons above 10MeV were calculated. The total photons above 10MeV in the direction of the $\pi/4$ radian were shown in Fig.11. The horizontal axis shows the tantalum thickness, the vertical axis shows the total photons. When the electron energies were 60MeV and 100MeV, the total photons show the maximum intensity at the 10mm thick tantalum. When the electron energy was 30MeV, the total photons show the maximum intensity at the 4mm thick thickness. So it will be concluded that, in the case of 30MeV electron, the 4mm thick tantalum target is the best one for generation of neutron in the direction of the $\pi/4$ radian.

The total photons obtained by the 10mm thick tantalum were shown in Fig.12. The horizontal axis shows the energy of electrons, the vertical axis shows the total photons. The photons in the direction of the 0 radian became intensive, the photons in the direction of the $\pi/2$ radian were weak. The total photons at all direction increase with increasing the electron energy.

The total photons obtained by the 1mm thick tantalum were shown in Fig.13. The total photons in the direction of the 0 radian were intensive, that in the direction of the $\pi/2$ radian were weak. The total photons in the direction of the 0 radian increase with increasing the electron energy. But the total photons in the direction of the $\pi/4$ radian and the $\pi/2$ radian decrease with increasing the electron energy.

4 Conclusions

From the investigation stated above, conclusions are as follows,

1. The photons emitted from the 1mm thick tantalum by the electrons of 100MeV were less than that from the 10mm thick tantalum in the direction of the $\pi/4$ radian and the $\pi/2$ radian. The photons from the 1mm thick tantalum were more intensive than that from the 10mm thick tantalum in the direction of 0 radian. Therefore, when the neutrons were generated at the straightforward by the electrons of 100MeV, the 1mm thick tantalum was superior to the thicker tantalum from the view point of the radiation safety and the performance as the neutron generator.

2. When the neutrons were generated in the direction of the $\pi/4$ radian or the $\pi/2$ radian by the electrons of 100MeV, the 10mm thick tantalum is needed at least to generate the neutrons sufficiently.

3. When the neutrons were generated in the direction of the $\pi/4$ radian by the electrons of 30MeV, the 4mm thick tantalum seemed to be the best size for getting the maximum intensity of neutrons.

References

1) W. R. Nelson, H. Hirayama and D. W. O. Rogers, "THE EGS4 CODE SYSTEM", *SLAC-265*, December 1985.

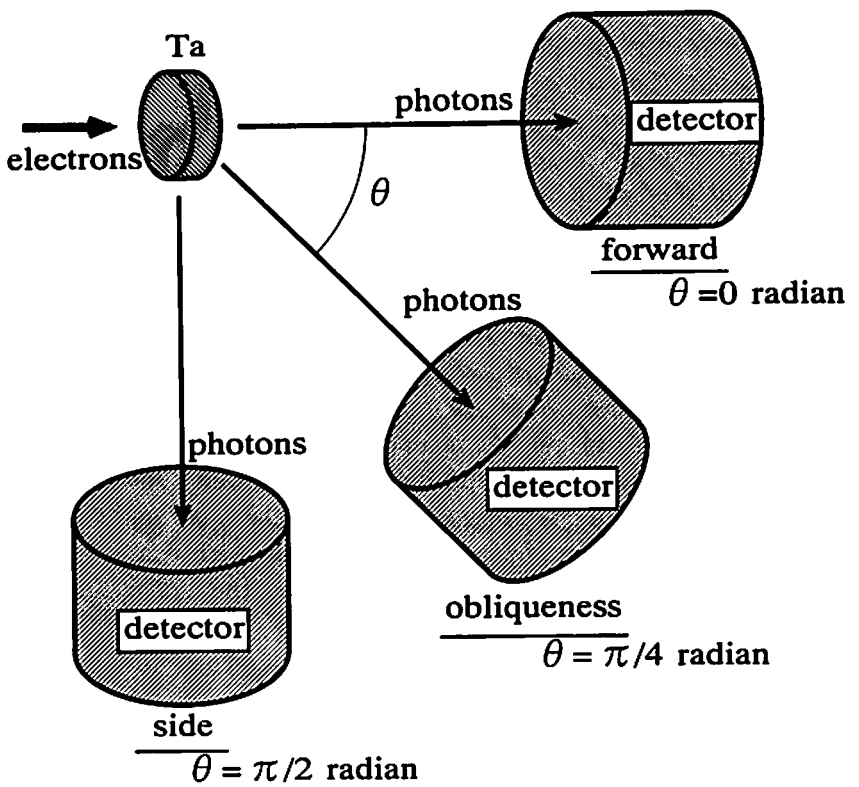

Fig.1 The arrangement of the tantalum target and the detector used for the calculation of the photons spectra.

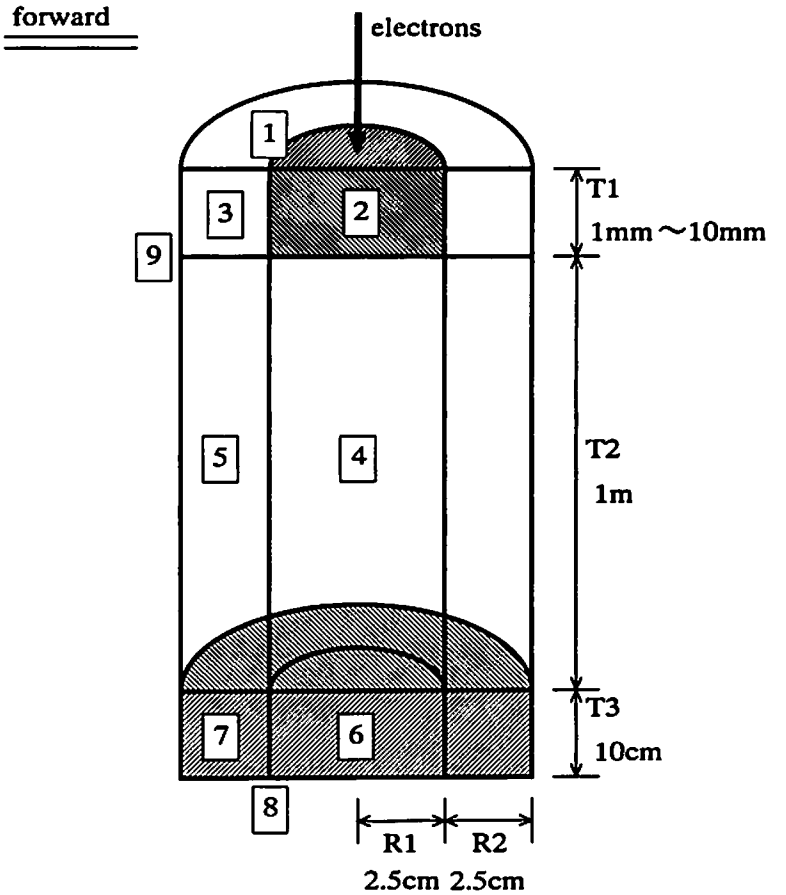

2 : Tantalum

6, 7 : Detector (Air)

1, 3, 4, 5, 8, 9 : Gap

Fig.2 The geometrical model used for the calculation of the photons detected in the direction of the 0 radian.

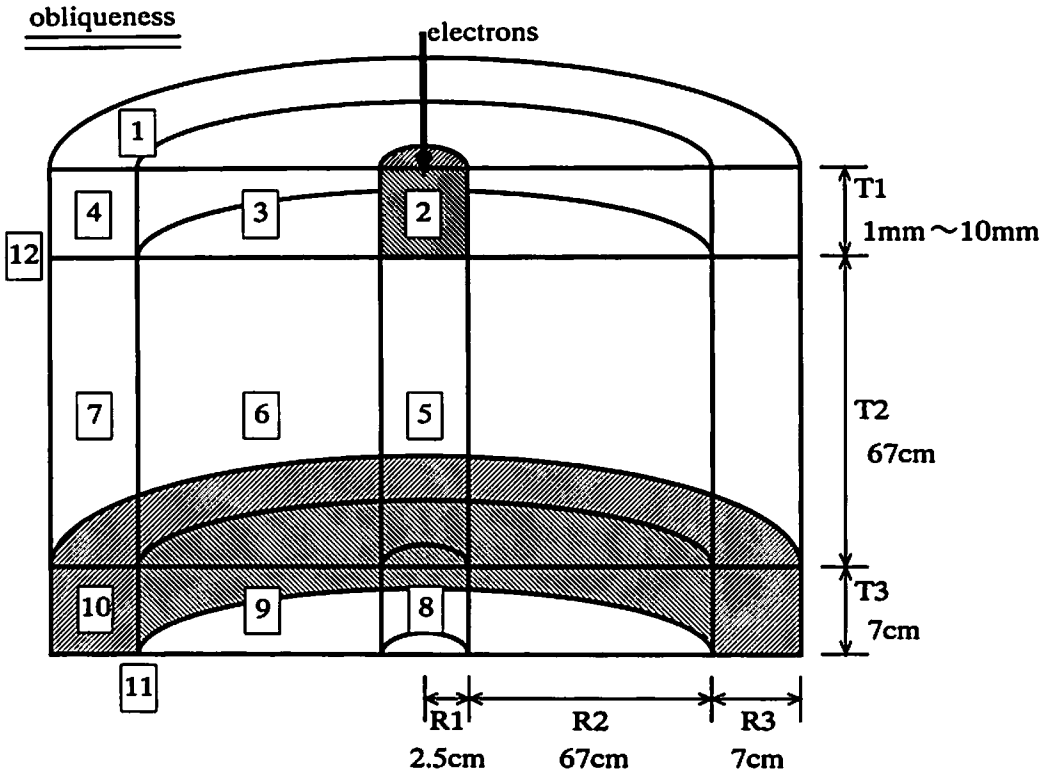

Fig.3 The geometrical model used for the calculation of the photons detected in the direction of the $\pi/4$ radian.

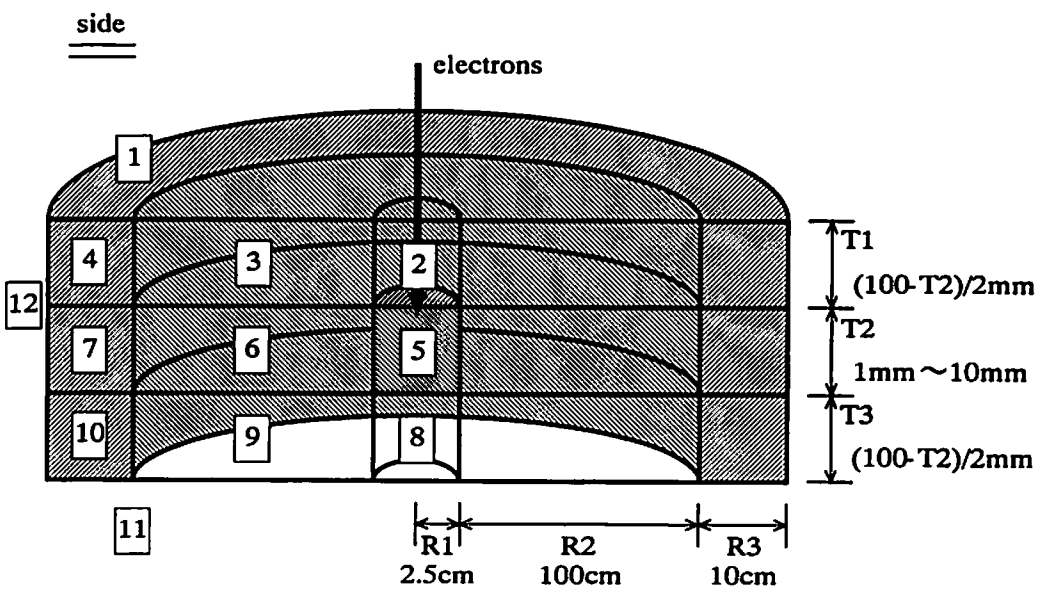

Fig.4 The geometrical model used for the calculation of the photons detected in the direction of the $\pi/2$ radian.

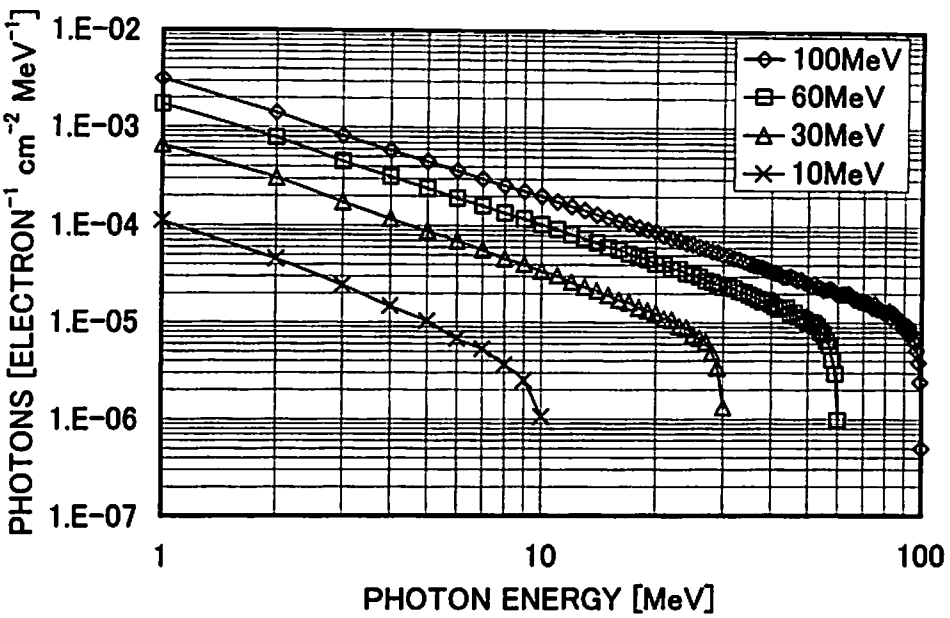

Fig.5 The energy spectra of photons observed by the 1mm thick tantalum in the direction of the 0 radian.

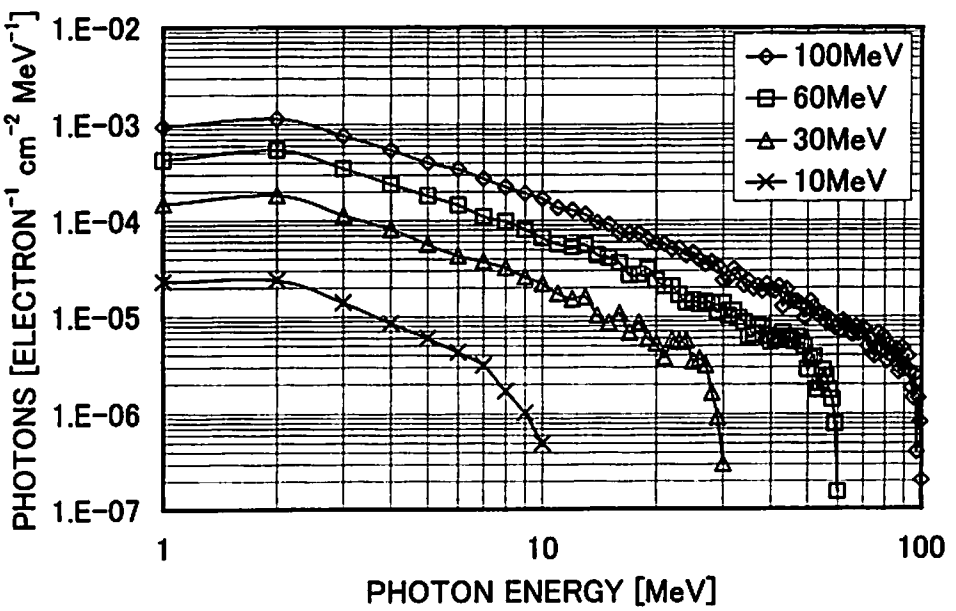

Fig.6 The energy spectra of photons observed by the 10mm thick tantalum in the direction of the 0 radian.

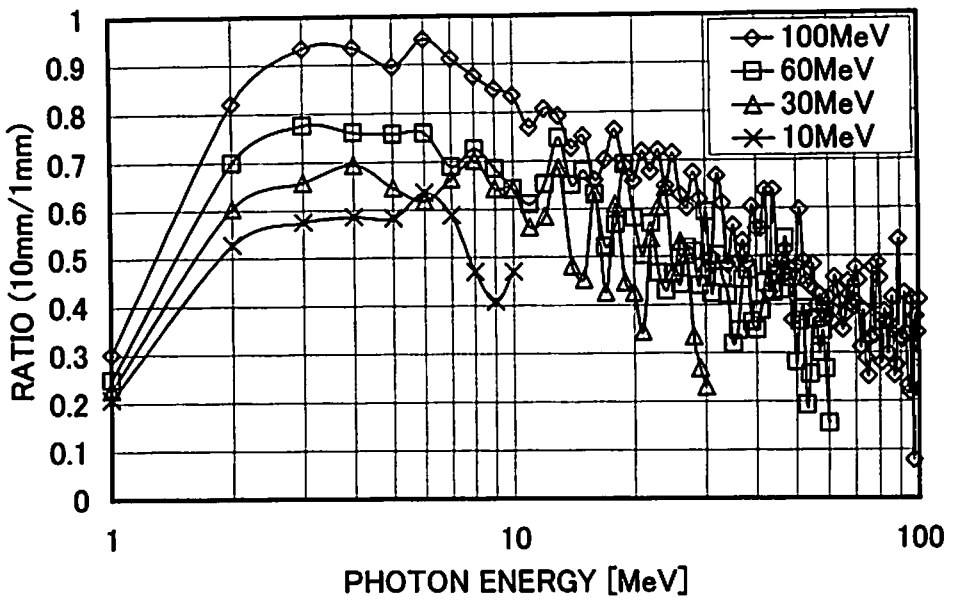

Fig.7 The ratios of the photons spectra observed by the 10mm thick tantalum to that observed by the 1mm thick tantalum.

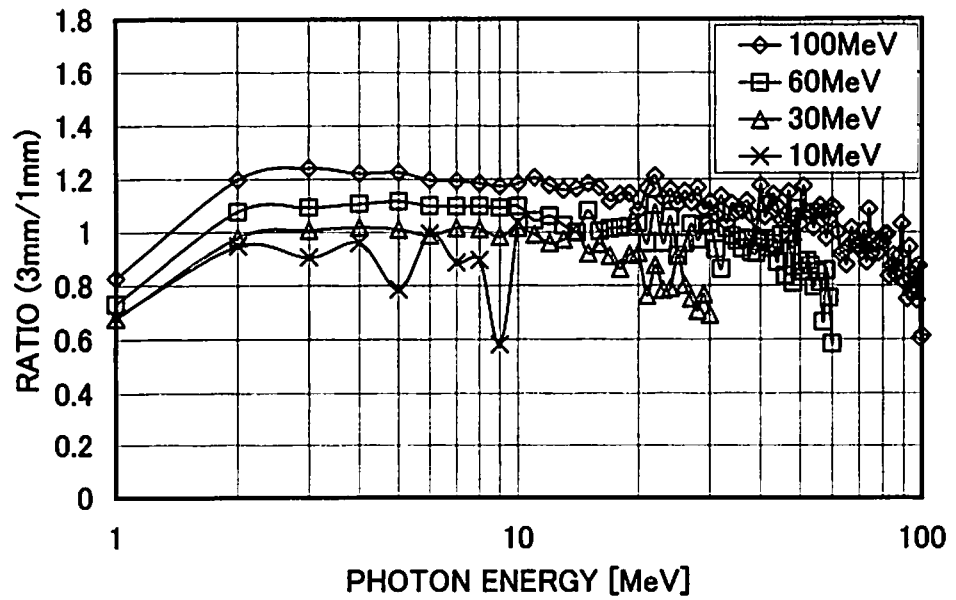

Fig.8 The ratios of the photons spectra observed by the 3mm thick tantalum to that observed by the 1mm thick tantalum.

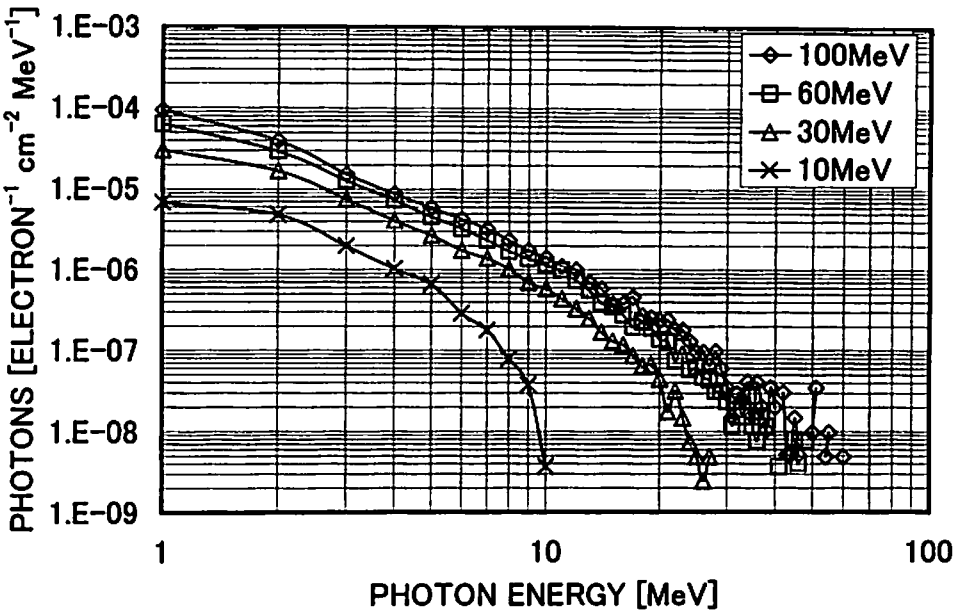

Fig.9 The energy spectra observed by the 10mm thick tantalum in the direction of the $\pi/4$ radian.

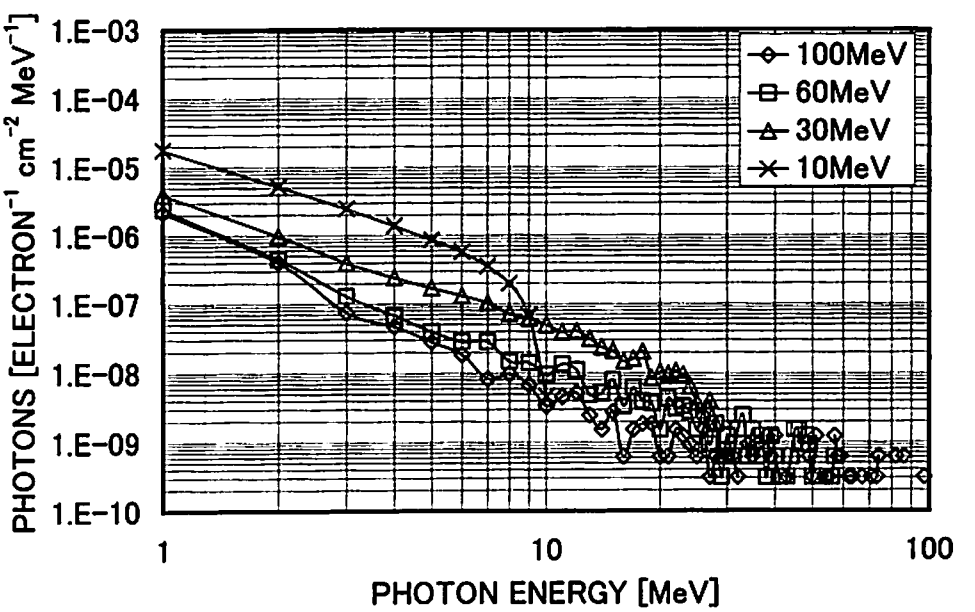

Fig.10 The spectra of photons observed by the 1mm thick tantalum in the direction of the $\pi/4$ radian.

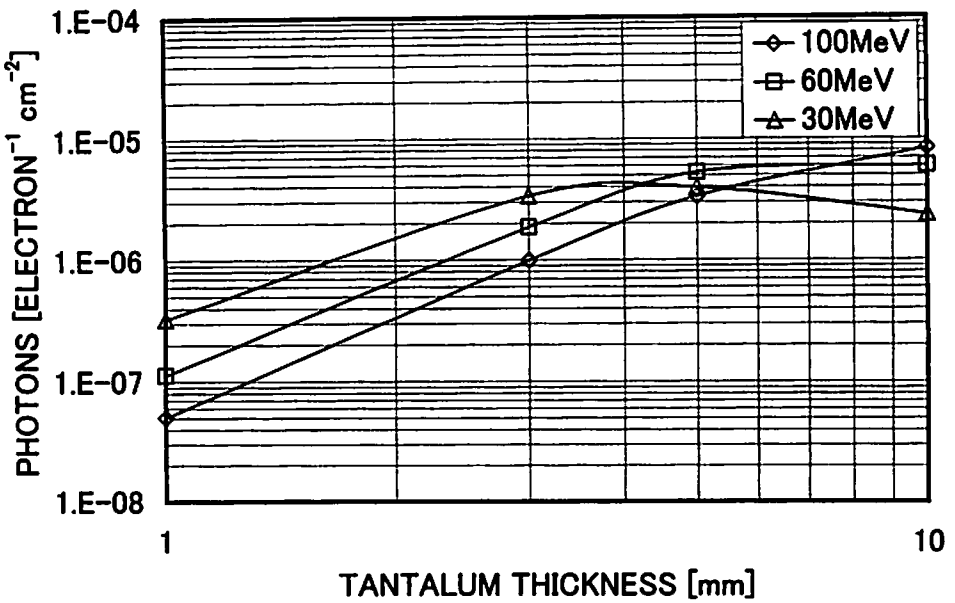

Fig.11 The total photons above 10MeV in the direction of the $\pi/4$ radian.

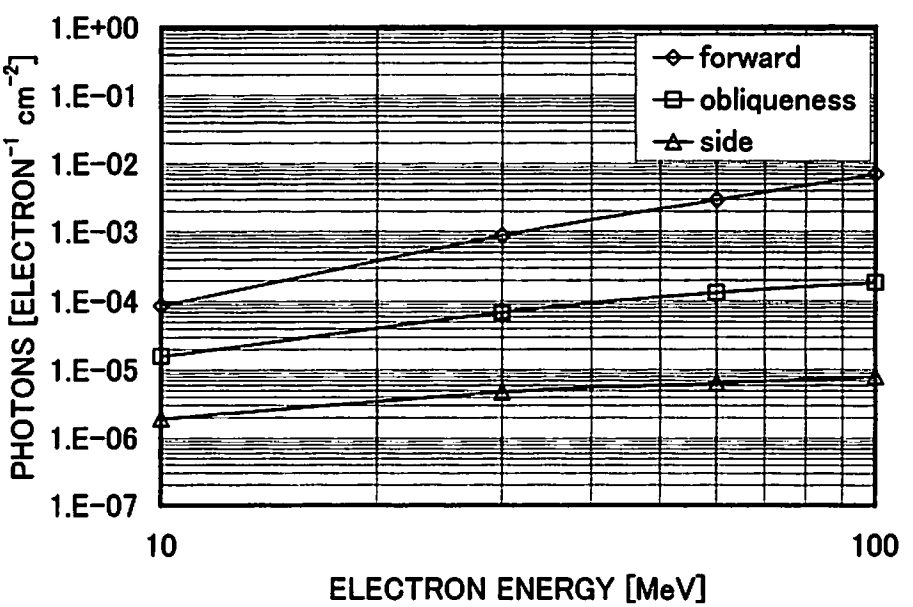

Fig.12 The total photons obtained by the 10mm thick tantalum.

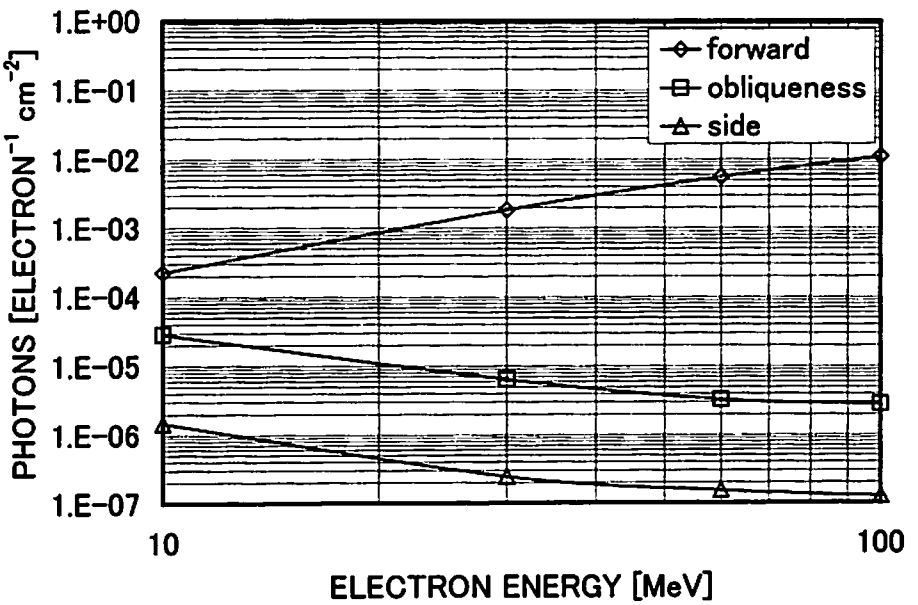

Fig.13 The total photons obtained by the 1mm thick tantalum.